This is to certify that the
dissertation entitled

MODELS OF AXONAL ELONGATION AND TRANSPORT

presented by

Matthew R. O'Toole

has been accepted towards fulfillment
of the requirements for the

Doctoral degree in Mathematics

Major Professor's Signature

9/29/10

Date

MODELS OF AXONAL ELONGATION AND TRANSPORT

By

Matthew R. O'Toole

A DISSERTATION

Submitted to
Michigan State University
in partial fulfillment of the requirements
for the degree of

DOCTOR OF PHILOSOPHY

Mathematics

2010

ABSTRACT

MODELS OF AXONAL ELONGATION AND TRANSPORT

By

Matthew R. O'Toole

The topic of axonal elongation has been studied for just over one-hundred years. It is only recently, however, that the problem has received the attention of mathematical modelers. Most of these models assume that elongation of an axon occurs when cytoskeletal materials are delivered to the distal tip (or growth cone) of the axon, where they are incorporated into the end of the existing framework. Several pieces of evidence, however, have been suggestive of another mode of elongation.

Axons are viscoelastic structures; inside the outer membrane is a network of microtubules, neurofilaments, motor proteins, organelles, and various other cytoplasmic materials. Axial forces are exerted on the axon from the distal end of the the neuron. In pre-synaptic neurons these forces are generated by the interactions of the protein actin with the substrate (or path) on which the axon is elongating. In post-synaptic neurons, the forces of bodily growth exert tension on nerves, and nerves elongate as the body grows larger. These axial forces cause deformation of the viscoelastic axons, which leads to neuronal lengthening and displacement of the existing cytoskeleton. This thesis is the first effort to describe the axons response to applied tension and the effect that these forces have on slow axonal transport.

In the first chapter, a biophysical model of axonal elongation is derived. The axon is treated as a viscoelastic fluid under tension, and a system of equations are developed to describe how the forces cause distension of the cytoskeleton. The effects of force dissipation due to interactions with the substrate are incorporated into the velocity equation.

Axonal demands for new material are the topic of the second chapter. As an axon elongates, it must supply the new section of axon with materials, replace material

which becomes dysfunctional, and uniformly add new material to cause any increases in axonal caliber. This chapter lays the groundwork for the study of stretching's role in slow axonal transport.

Chapter three examines under what circumstances stretching makes a significant contribution to slow axonal transport. Until now, the phenomenon has been overlooked, but the modeling in this chapter shows that, under certain conditions, stretching can supply nearly half the flux necessary to sustain a healthy axon.

In the fourth chapter we view the problem of slow axonal transport as a boundary value partial differential equation. The problem, in its entirety, includes carrier-mediated transport, stretch-induced transport, diffusion, and protein degradation. As a first step to analyzing this PDE and what it can tell us about each transport process, a perturbation problem is studied when diffusion is the sole method of transport, and an analytical solution is found.

The final chapter summarizes the dissertation and discusses the role of this work in the field of nerve repair.

DEDICATION

This thesis is dedicated to my parents and family that have given so much to make this possible, and to my wife Lia who has been at my side throughout this entire endeavor. I am eternally grateful for their love and support, without which I surely would not have been able to complete this work.

ACKNOWLEDGMENT

I would like to thank the various people who have helped me complete this labor. I could not have gotten to this point without the generous gifts of time and knowledge provided to me by so many gracious people.

First I would like to thank the members of my committee. I am most grateful to Dr. Kyle E. Miller, who took me as a student in his laboratory when I had minimal knowledge of neurological systems. His patience and tutelage allowed me to take on the projects covered in this manuscript, and he has guided me in learning how to succeed in the scientific community. He is a fantastic advisor and a good friend. My co-advisor, C.Y. Wang, was first an amazing instructor for several of my graduate courses. His knowledge of and passion for applied mathematics were a true inspiration as I strived to become a better mathematician. I hope that I am able to emulate his traits in my career as a professor. Dr. Guowei Wei provided me with my first exposure to computational biology and introduced me to Dr. Miller. Dr. Chichia Chiu taught me numerical analysis and was a valuable committee member. Finally, Dr. Peter Bates has provided many helpful comments that have improved this thesis.

Philip Lamoureux supplied much of the data used in the first two chapters. Rehan Baqri and Robert Latham contributed the lab-work from the second chapter. Other members of Dr. Miller's lab have provided helpful discussions on biological topics and general support, including Bradley Hammond, Brittany Turner, and Julie Taylor. Dr. Steven Heidemann was particularly generous with his time and knowledge.

Many colleagues contributed to my success as a graduate student. Those whose support was vital to my success are: Ahmet Ay, Benjamin Beckmann, Justin Carroll, Michael Dabkowski, Jacqueline Dresch, Joseph Timmer, and Eric Waggoner.

Lastly, thanks are in order for Dr. Clifford Weil for his invaluable help as I learned to use LaTeX.

TABLE OF CONTENTS

LIST OF TABLES

LIST OF FIGURES

Chapter 1

A Biophysical Model of Axonal Elongation

1.1 Introduction

Axonal elongation has been thought to occur through tip growth where new material is added at the growth cone and the axonal framework is stationary [26, 13, 41]. While past studies suggest axonal branch points and marks made along the axon remain stationary as the axon elongates [9, 10, 56, 68, 24], recent work suggests that in some cases there is a gradient of bulk transport of docked materials, with little or no transport seen in the proximal axon and increasing anterograde transport in the distal axon [64]. This low velocity transport (LVT) has been observed in the absence of growth-cone advance, which suggests that there is more to this than simple stretching of the axon. In addition, whether axons lengthen through tip growth or stretching in Xenopus neurons depends on whether they are grown on highly adhesive (Con A) or permissive substrates (laminin) [23]. These past studies raise the questions of what role growth cone generated tension plays in elongation, and whether the mode of axonal elongation depends on the physical properties (adhesion to the substrate,

viscosity) of the axon.

Mechanical tension has long been known as an effective stimulus to axonal elongation / growth. Tension has been experimentally applied to lengthen existing neurites [11, 51], and axons that are detached from their substrate not only stop elongating, but experience retraction [99]. Mass addition to the neurite is another important aspect of axonal elongation which appears to be linked to tension. In one instance, elongation rates of 8 mm/day were achieved via mechanically applied tension [74]. These neurons tended to increase in diameter [74] and were functionally normal [73]. In another experiment, leg-lengthening procedures in adult rats caused doubling of the internodal distances with no axonal thinning [1]. These results indicate that the rate of mass addition to the axon increases in response to tension-induced lengthening. Further, the inability of microtubule polymerizing drugs, such as taxol, to induce elongation [54] brings into question whether mass addition independently drives elongation. Mass addition is certainly an essential component of healthy axonal elongation, but the evidence suggests that tension at the growth cone is the direct factor that controls the rate of lengthening. Thus, we place tension as the independent variable which determines the rate of axonal lengthening.

En bloc movement of the axonal cytoskeleton long went unnoticed as experimental observations focused on proximal regions of axons. Only when measurements were made in the distal axon was this phenomenon discovered. Photobleaching [23, 70], photoactivation [69, 77], and the tracking of docked mitochondria [64] have revealed that the cytoskeleton does move in an anterograde manner, but this behavior diminishes with distance from the growth cone. That growth cones generate pulling forces and neurons grown in culture adhere to their substrates gives a possible insight to this observation. Any deformation of the axon as a result of growth cone generated tension will be most prominent in the distal region, but as that force is dissipated through adhesions the effects will diminish. As the above experiments have shown,

tension at the growth cone not only leads to lengthening, but may deform the distal region of the axon resulting in en bloc movement of the cytoskeleton.

Deformations of materials can be elastic, where materials stretch like springs, or viscous, where materials flow as fluids [38]. Here, axonal stretching refers to both elastic and viscous deformation. Whether axons behave mechanically as solids or fluids depends importantly on the time scale of the observations. Rapid deformations over the course of seconds to minutes lead to spring-like behaviors. When axons are pulled slowly enough over the course of hours to days they can elongate viscously many millimeters without breaking or thinning [74, 73, 25]. The observation that lengthening occurs without a great degree of thinning suggests that mass addition to the axon is occurring. It is possible that when axons are stretched slowly mass addition can accommodate lengthening and lead to a physiological behavior that is primarily viscous.

Axonal elongation in response to force application at the growth cone (towing) has been described to occur in three stages [25]. After an initial elastic stretch, there is a period of delayed stretching, followed by elongation at a constant rate. This behavior has been modeled by Dennerll et al., [25] using a three-element model where the axon behaved as a spring, a Voigt element, and a dashpot in series (Fig. 1.1 A). The combination is also known as a Burgers element [81]. This model well describes the effects of tensile stress on the elongation of axons, but does not address deformation of the distal axon or the effects of adhesions along the axon.

Aeschlimann was the first to extend a general type of model to segments along the axon [2, 3]. In the Aeschlimann model, the axon is treated as a series of springs that elastically stretch with a growth dashpot at the end of the axon where new mass is added. This accounted for the spring-like behaviors axons exhibit over short time spans and the fluid-like behaviors associated with axonal lengthening. A further insight was the incorporation of viscous drag that was interpreted as being due to

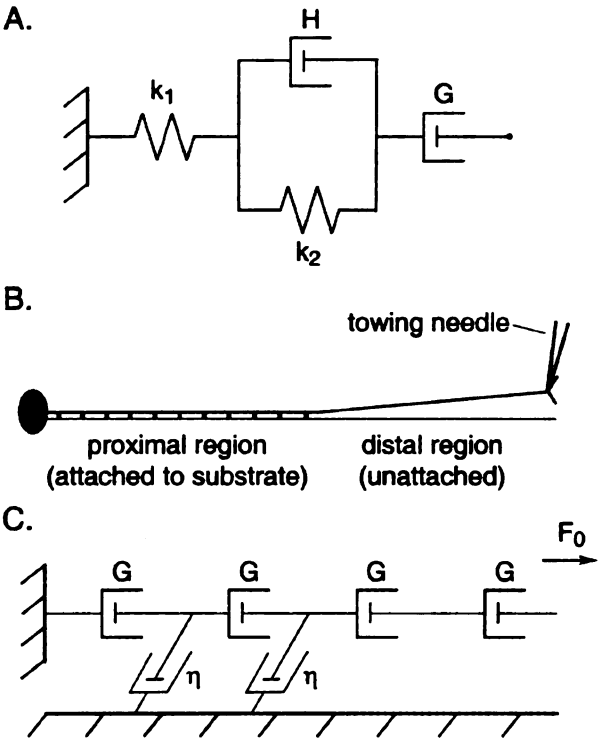

Figure 1.1: Modeling a Towed Neurite as a Series of Dashpots — (A) We consider the axon as a series of Burgers elements. Each element consists of a two elastic elements and a free dashpot (with constant G) which simulates towed growth. (B) Diagram of a neurite during towing. The distal region of the neurite is free of the substrate while numerous adhesions in the proximal region cause the neurite to remain firmly fixed. (C) Under constant tension (F_L) the behavior of a Burgers element is dominated by its free dashpot. We treat a neurite under constant tension as a series of dashpots. Attachments to the substrate are represented as friction dashpots (constant η). Tension is constant in the distal region but is dissipated by adhesions in the proximal region.

interactions between the axonal shaft and substrate. While the Aeschlimann model is sophisticated in its integration of both the tip growth model and the biophysical properties of the axon, the following experimental data suggest to us that the axon is more accurately modeled as a series of dashpots that acts like a viscoelastic fluid. (A) Though rapid deformations over the course of seconds to minutes lead to spring-like behaviors, when axons are pulled slowly enough over the course of hours to days they can elongate viscously many millimeters without breaking or thinning [74, 73, 25]. (B) Growth cones sometimes pause while the axon remains under tension. If axons behaved as viscoelastic solids, material along the axon would stop moving during a pause. In contrast, a viscoelastic fluid model predicts continued movement of the axonal framework towards the site of tension generation. Experimentally, it is seen that bulk movement of material occurs during growth cone pauses [64]. Thus, we suggest that the simplest model for the mechanical behavior of the axon is that of a viscoelastic fluid.

Here we extend the Dennerll model to the entire axon; that is we view each segment of axon as consisting of a Burgers element. This allows us to study how tensile forces cause axonal stretching at each point along the length of the neurite in addition to elongation. With the inclusion of the effects of extracellular adhesions along the length, we derive a model that captures both the effects of tension generation at the growth cone and dissipation along the length due to adhesions to the extracellular matrix substrates [23]. We report that whether axons grow by stretching or tip growth can be explained by varying the parameters in a single model that includes forces, axonal mechanical behavior, and frictional interactions with the substrate.

1.2 Materials and Methods

1.2.1 Cell Culture

Chick sensory neurons were isolated as described by Sinclair et al. [85] from lumbosacral dorsal root ganglia of 11-to 12-day-old chicken embryos. Cells were grown at 37 °C in L-15 medium (Sigma Chemical, St. Louis, MO) supplemented with 0.6% glucose, 300 mg/liter glutamine, 100 U/ml penicillin, 136 μM/ml streptomycin sulfate, 10% fetal calf serum, 50 ng/ml 7S nerve growth factor (Harlan Bioproducts, Indianapolis, IN) and N9 growth supplement. The culture surface was first treated with 0.01% polyornithine and rinsed. The surfaces were then treated with 20 ng/ml laminin.

1.2.2 Towing Experiments

Mitochondria were labeled with 0.1 μM Mitotracker Red CMX-Ros (Molecular Probes, Eugene, OR) in L-15 medium for 2 min. and then allowed to recover for several hours in fresh media [64]. Cultured cells were maintained at 38 °C on the stage in a ringcubator [37]. A reference needle and a calibrated needle (calibration constant k as in [99, 25, 98, 97]) were held in a double-needle holder in a Narishige hydraulic micromanipulator. The needles were brought into the culture dish's microscopic viewing field of a Leica DM IRB inverted microscope and observed with a N Plan L 40×/0.55 corr Ph2 with an adjustable collar infinity / 0—2 / c objective. Cells were illuminated with a 100-W Xenon lamp attenuated 98% with neutral density filters through a Texas Red cube D560/40×, 590DCLP, D630/60m (Chroma, Rockingham, VT) for visualization of MitoTracker Red CMX-Ros.

The calibrated towing needle was previously coated in polylysine (1 mg/ml) and concanavalin A (1 mg/ml). Both needles were brought to the neurite's growth cone and the growth cone was manipulated onto the calibrated towing needle. The ma-

nipulator was used to move the needle and exert axial tension on the growth cone [25]. Each tow consisted of two phases and within each phase the force was held constant. The resting distance r between the two needles was noted prior to cell attachment. Force measurements were acquired during phase imaging throughout the experiment by measuring the distance, d, between the reference needle and the calibrated needle under experimental tension. The screen-image calibration factor, α, was determined by use of images of a stage micrometer. The applied force at the growth cone (in μdynes) was calculated as $F_L = \alpha k\,(d - r)$ [25]. Fluorescent images were taken at 2 min. intervals by an automated script of the Openlab program (Improvision, Waltham, MA) using a Hamamatsu Orca-ER digital camera CCD, model CA742-95. These images were then converted into TIFFs and analyzed using ImageJ (NIH). Images were rotated using an ImageJ plug-in and the StackReg macro was used to align each sequence of images. The images were then cropped, resliced, and z-projected to produce a kymograph. Kymographs were enlarged 2$\times$ and brightness and contrast were manipulated to enhance visualization of mitochondria.

1.2.3 Derivation of Model

As axons are thought to be viscoelastic structures, we hypothesize that forces generated at the growth cone can stretch the axon and give rise to LVT. Whether this LVT occurs will depend on the relationship between the magnitude of the force generated at the growth cone and the viscoelastic properties of the axon. Even though axons can behave like fluids, if they are exceptionally stiff or if the forces generated at the growth cone are too weak, axonal stretching may not occur and elongation will occur through tip growth.

We consider an axon that experiences a constant force averaged over hours at the growth cone (this tension may be internally or externally generated). For the purpose of a continuous model, we treat the axon as a series of infinitesimally small Burgers

elements. If tension is applied for a significant amount of time (> 10 minutes) the axon exhibits constant growth rate [25]. Under these conditions the elastic elements of the cell are at steady state and elongation behaves as force acting on a free dashpot (a dashpot obeys the relationship *force* = *constant* × *velocity*). To analyze bulk transport along the length we simplify the model and treat the axon, in this state, as a series of dashpots (Fig. 1.1 C). A series of dashpots under constant tension, without dissipation at each element, has a linear velocity profile which, when additional dashpots are added in series (through elongation), leads to exponential elongation.

As axons stretch, so must the axonal framework. Using the reported value of the Young's modulus of a microtubule of 100MPa [47], a force of 100 μdynes applied to an individual microtubule will cause $\approx$ 2% strain. Since a growth cone generated force of this magnitude is spread over the cross-sectional area of the axon, the strain on axonal microtubules will be much less. As the stretching of individual polymers is extremely small, significant stretching of the axon most likely occurs by the sliding of cross-linked polymers. The two factors playing the largest role in the velocity profile of an axon under tension are the axon's axial viscosity, g, and the constant of friction, η, that quantifies the interactions between the axon and the substrate. Both of these parameters characterize resistance to flow and have dimensions of viscosity. The axial viscosity is the amount of force needed to distend a unit amount of axon at unit velocity and is determined by the cell's physiological properties. Though the axoplasm is highly heterogeneous, it is the composition of the cytoskeleton that will dictate the axon's response to axial forces. If there are a large number of microtubules, or a high level of cross-linkage between them, then the axon will be resistant to stretching and g will be large [38]. Axonal diameter will also affect an axon's ability to be stretched. Intercalated mass addition (axonal thickening) has the effect of adding dashpots, in parallel, to the system (or, equivalently, increasing the dashpot constant). Applied forces are spread over a wider area and effective tension along the length decreases.

We define the growth dashpot parameter G to quantify an axon's response to distally applied forces. This parameter is the product of g and the cross sectional area of the axon A. If an axon alters its diameter (either thinning due to stretching or thickening by mass addition along the length) but maintains its physiological properties, then G is affected while g is unchanged. Physiological changes alter g and thus G. The coefficient of friction, η, is characterized by the strength and the number of adhesions between axon and substrate. These adhesions have been shown to have major effects on both LVT and growth cone advance [23]. η is assumed to be zero where the axon is unattached to the substrate, and increases as adhesions form and strengthen.

Towed axons were observed to be unattached distally and firmly attached to the substrate in the proximal regions (Fig. 1.1 B). The behavior of the axon in the unattached region can be well described by the three-element model. Our model aims to incorporate the dissipation of forces and describe the velocity profile of docked materials when adhesions are present. We assume that: 1) there is uniform dissipation along the length characterized by the constant η; and 2) during elongation due to towing, the growth dashpot constant G remains fixed on average over a period of days so that constant applied force implies constant tension. Note that our condition on G is not inconsistent with an axon that changes its diameter; physiological changes can be assumed to balance changes in cell morphology. The phenomenon of strain hardening due to deformation has indeed been observed in various cell types [38]. If axons do not exhibit thinning, then we assume that mass addition along the length of the axon, or intercalated mass addition, is responsible for restoring the diameter of axons which grow by stretching. These assumptions allow for a simple and useful analytic description of the effects of cellular composition and external adhesions on axonal elongation and transport.

1.2.4 Governing Equations

The force and velocity profiles of the axons, f and v, are functions of the distance from the cell body x and the length of the axon $L(t)$. A force F_L applied at the growth cone causes distension at each point along the length. The change in velocity from one point of reference to the next (from x_{i-1} to x_i) is given by the rate at which the dashpot between them is elongating:

$$\Delta_x v = v\left[x_i, L(t)\right] - v\left[x_{i-1}, L(t)\right] = \frac{f\left[x_i. L(t)\right]}{G/\Delta x} \tag{1.1}$$

so that the actual velocity of the point of reference x_i is found by summing these elongation rates between x_0 and x_i:

$$v\left[x_i, L(t)\right] = \sum_{j=1}^{i} \frac{f\left[x_i, L(t)\right]}{(G/\Delta x)} = \frac{1}{G}\sum_{j=1}^{i} f\left[x_j, L(t)\right]\Delta x. \tag{1.2}$$

Force is dissipated at a rate proportional to the velocity of elongation:

$$\Delta_x f = f\left[x_i, L(t)\right] - f\left[x_{i-1}, L(t)\right] = (\eta\Delta x)\, v\left[x_i, L(t)\right]. \tag{1.3}$$

Given a constant force generated at the growth cone F_L the force at any reference point x_i is given by

$$\begin{aligned} f\left[x_i, L(t)\right] &= F_L - \eta \sum_{j=i+1}^{N} v\left[x_j, L(t)\right]\Delta x \\ &= F_L - \frac{\eta}{G}\sum_{j=i+1}^{N}\left(\sum_{k=1}^{j} f\left[x_k, L(t)\right]\Delta x\right)\Delta x \end{aligned} \tag{1.4}$$

To extend to the continuous case we let $\Delta x \rightarrow 0$ so that

$$f\left[x, L\left(t\right)\right] = \lim_{\Delta x \rightarrow 0} f\left[x_i, L\left(t\right)\right] = F_L - \frac{\eta}{G}\int_x^L \int_0^y f\left[z, L\left(t\right)\right] dzdy. \tag{1.5}$$

The integral equation (1.5) is equivalent to the differential equation and boundary conditions

$$\begin{aligned} &f_{xx}\left[x, L(t)\right] - \tfrac{\eta}{G} f\left[x, L(t)\right] = 0 \\ &f\left[L(t), L(t)\right] = F_L \qquad\qquad f_x\left[0, L(t)\right] = 0 \end{aligned} \tag{1.6}$$

Note that Eq. (1.6) is in terms of the unknown $L(t)$. The rate of elongation dL/dt is assumed to be the velocity of material at the growth cone $v\left[L(t), L(t)\right]$. Differentiating Eq. (1.5) with respect to x we find

$$f_x\left[x, L(t)\right] = \frac{\eta}{G}\int_0^x f\left[z, L(t)\right] dz = \eta v\left[x, L(t)\right].$$

Now we can express the change in length of the axon in terms of the force by

$$\begin{aligned} &\frac{dL}{dt} = v\left[L(t), L(t)\right] = \tfrac{1}{\eta} f_x\left[L(t), L(t)\right] \\ &L(0) = L_0 \end{aligned} \tag{1.7}$$

1.2.5 Force, Velocity, and Length

Equation (1.6) is solved first and the solution for f is then inserted into Eq. (1.7).

$$f\left[x, L(t)\right] = \frac{F_L \cosh\left[x\sqrt{\frac{\eta}{G}}\right]}{\cosh\left[L(t)\sqrt{\frac{\eta}{G}}\right]} \tag{1.8}$$

$$L(t) = \sqrt{\frac{G}{\eta}}\,\mathrm{asinh}\left[\beta \exp\left(\frac{F_L t}{G}\right)\right] \tag{1.9}$$

where $\beta = \sinh\left[L_0\sqrt{\frac{\eta}{G}}\right]$. Velocity is determined from the force as before ($v = f_x/\eta$):

$$v\left[x, L(t)\right] = \frac{F_L \sinh\left[x\sqrt{\frac{\eta}{G}}\right]}{\sqrt{\eta G}\cosh\left[L(t)\sqrt{\frac{\eta}{G}}\right]}. \tag{1.10}$$

1.2.6 Data Analysis

We tested the predictions of this model by examining the movement of axoplasm in response to tension as described in Materials and Methods. To fully analyze bulk transport of docked materials, the fluorescent images of each trial were converted into kymographs [64]. These useful images were created for each experiment, giving the total profile of movements within each axon over the course of the tow (Fig. 1.2). Tracing individual mitochondria, average velocities of docked material were calculated over 30-minute intervals (Fig. 1.3). For each tow there was an observed region where the axon was free of the substrate (distal) and a region where the axon was firmly attached (proximal). The distal region, being free of dissipative forces of substrate interaction, was analyzed to extract values of G for the axon. Lines were fitted to this data to calculate the rate of change of the velocity of the mitochondria (Fig. 1.4 A). Using force measurements from the calibrated needles, a value of G was found by dividing the average force over this interval by the slope of the fitted line.

Once values of G were determined (one value of G per 30 min.) the Origin software package (OriginLab Corporation, Northampton, MA) was used with Eq. (1.10) to fit the best value of η to the data (Fig. 1.4 B). For this calculation the velocities of mitochondria proximal to the point of adhesion were used. Empirical values of F_L, L, and G were fixed and a Levenberg-Marquardt algorithm was implemented in the Origin package to find the optimal value of η.

The relationship $G = gA$ was used to calculate the intrinsic axial viscosity for each axon. Phase images of each trial were analyzed using ImageJ to determine the

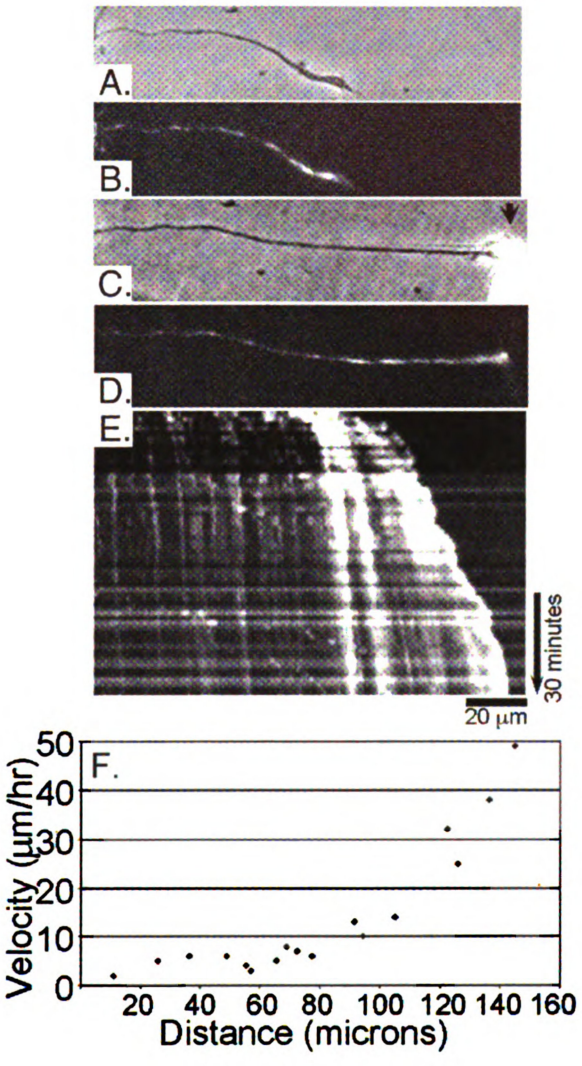

Figure 1.2: Application of Force at the Growth Cone Leads to Anterograde Translocation of Docked Mitochondria — (A) Axonal morphology at the light level before a tow. The growth cone is towards the right hand side. (B) Mitochondrial distribution before the tow. (C) Axonal morphology at the light level after the tow. The arrow points to the end of the needle at the growth cone. (D) Mitochondrial distribution after the tow. (E) Kymograph illustrating mitochondrial movement during a tow. (F) The graph shows that the velocity of docked mitochondria increases non-linearly along the axon.

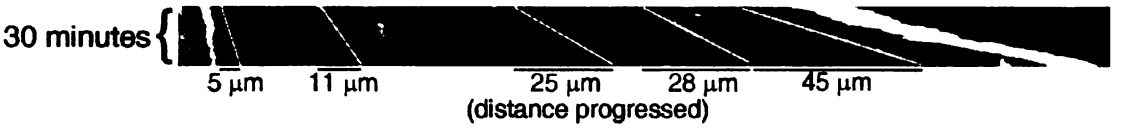

Figure 1.3: Illustration of how Velocity Data were Acquired — Docked mitochondria are observed to translocate anterogradely during a tow. Velocities (in microns per hour) of the mitochondria were calculated as the slope of each traced line. Mitochondria near the growth cone move forward at high velocities while mitochondria near the cell body move slowly.

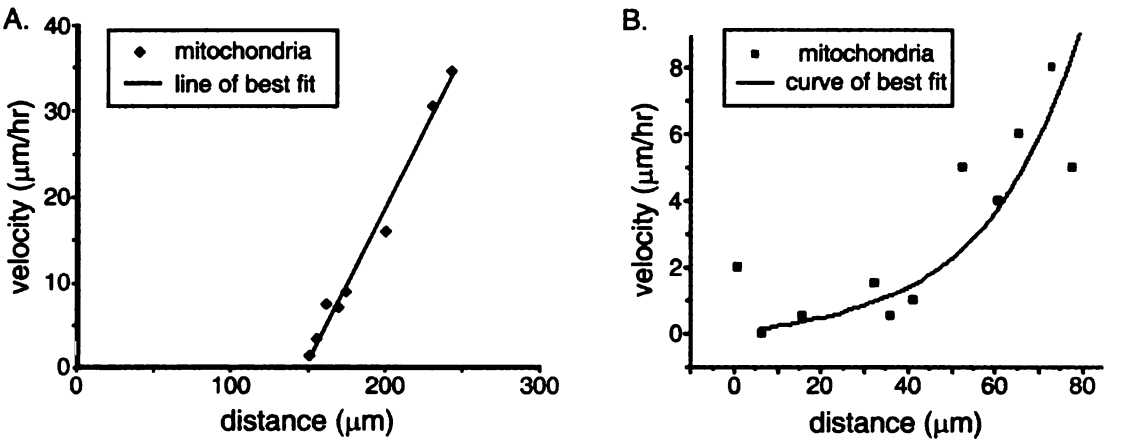

Figure 1.4: Determination of Axonal Viscosity (G) and Adhesiveness (η) — During towing, the distal axon was lifted free from attachments to the substrate. (A) Velocities were measured (one measurement per mito. per 30 min.) for mitochondria distal to the terminal point of adhesion between axon and substrate (for this axon, at 150 μm). The slope m of the line of best fit and the force F_L are related to G by $G = F_L/m$. (B) Velocity profile of mitochondria proximal to the terminal point of adhesion (at 80 μm for this trial). Force dissipation leads to a non-linear velocity profile. The data was fitted to Eq. (1.10) with an optimal value of η found using the Origin software package.

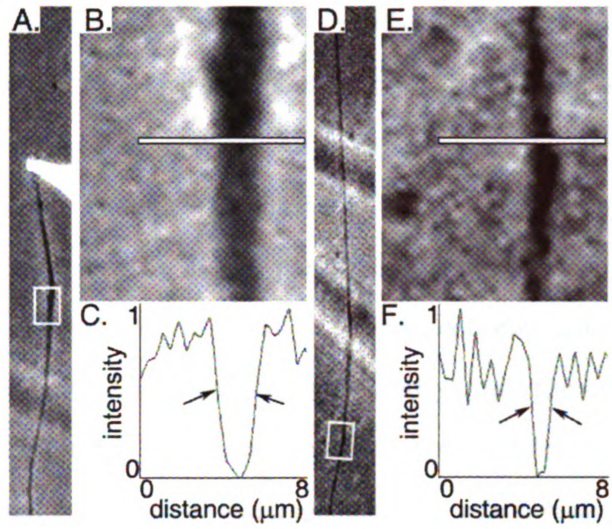

Figure 1.5: Illustration of the Measurement of Axonal Diameter — For each phase image (A, D), the diameters of the axons were measured using ImageJ (one measurement per 25 μm). A line orthogonal to the axon was drawn (B, E) and a plot profile gives the pixel intensity at each point along the line (C, F). Arrowheads in (C, F) denote the two steepest points on the relevant portion of the curve. Visible differences in axonal diameter (A, D) are reflected in (C, F).

axonal diameter at various times (Fig. 1.5). For each phase image, the diameter was measured at 25 μm intervals until the growth cone was reached. A line tool was traced orthogonally across the neurite and a plot profile graphed the pixel intensity of the image at each point on the line. It was determined that the best measure of the diameter was the distance between the two steepest points on the intensity curve.

1.2.7 Numerical Simulation

To address the issue of thinning along the length of the axon, we ran a MATLAB (The MathWorks, Inc., Natick, Massachusetts) simulation of an axon growing by stretching where zero mass addition was assumed and axonal diameter was allowed to vary. The details of the simulation are as follows. The axon is divided into a fixed number of compartments whose length and cross-sectional area are allowed to vary.

At each time step the force is calculated at the distal end of each compartment. This force causes deformation of each compartment and thus lengthening. New values for compartment length, area, and growth dashpot parameter G are then calculated for the next time step. Though η is constant, we account for the adhesive effect of increased compartment length. Using parameter values for g and η determined as above, axons were allowed to grow until the cross-sectional area at any point along the length decreased below 0.05 μm^2 (or, equivalently, until the diameter at any point decreased below 0.25 μm). This basic simulation does not take into account protein degradation or axonal transport of existing materials which may occur to maintain a uniform diameter.

1.3 Results

1.3.1 Consistency

We verify that the model equations are consistent with the physical nature of the problem. Letting the parameters vary we examine the effects on Eq. (1.10). It is important to remember, here, that η characterizes adhesions along the length of the axon and not at the growth cone. As adhesions at the growth cone are necessary for tension generation, our model would predict that those adhesions increase rates of elongation.

The removal of adhesive connections along the length corresponds to η going to zero. In this case forces generated at the growth cone are not dissipated through the substrate and we should expect a linear velocity profile, as that is the behavior of a

series of dashpots under tension. We show that this is indeed the case:

$$\begin{aligned}
\lim_{\eta\to 0} v\left[x, L(t); \eta\right] &= \frac{F_L}{\sqrt{G}} \lim_{\eta\to 0} \frac{\sinh\left[x\sqrt{\frac{\eta}{G}}\right]}{\sqrt{\eta}\cosh\left[L(t)\sqrt{\frac{\eta}{G}}\right]} \\
&= \frac{F_L}{G} x \lim_{\eta\to 0} \frac{\sinh\left[x\sqrt{\frac{\eta}{G}}\right]}{x\sqrt{\frac{\eta}{G}}} \lim_{\eta\to 0} \frac{1}{\cosh\left[L(t)\sqrt{\frac{\eta}{G}}\right]} \\
&= \frac{F_L}{G} x
\end{aligned} \tag{1.11}$$

where we have used that $\lim_{y\to 0} \frac{\sinh(y)}{y} = 0$.

In the presence of strong adhesions, forces are dissipated quickly and transport is hindered. Large values of η describe this phenomenon. For a fixed force, if η is too large then the effective tension along the length of the axon is too low to facilitate transport. As the strength of the adhesions increases, $\eta \to \infty$ and $v \to 0$ $\forall x$:

$$\begin{aligned}
\lim_{\eta\to\infty} v\left[x, L(t); \eta\right] &= \frac{F_L}{\sqrt{G}} \lim_{\eta\to\infty} \frac{\sinh\left[x\sqrt{\frac{\eta}{G}}\right]}{\sqrt{\eta}\cosh\left[L(t)\sqrt{\frac{\eta}{G}}\right]} \\
&\leq \frac{F_L}{G} x \lim_{\eta\to\infty} \frac{1}{\sqrt{\eta}} \tanh\left[L(t)\sqrt{\frac{\eta}{G}}\right] \\
&\leq \frac{F_L}{G} x \lim_{\eta\to\infty} \frac{1}{\sqrt{\eta}} \\
&= 0
\end{aligned} \tag{1.12}$$

since v is assumed to be non-negative and $0 < \tanh(y) < 1$ for $y > 0$.

If G is relatively large then the axon will be resistant to stretching at normal forces. This will occur when an axon has a large diameter or if there is a great deal

of microtubule cross-linkage. A direct calculation shows $v \to 0\ \forall x$ as $G \to \infty$.

Lastly we consider the case when $G \to 0$. If G is very small at a point x then either the diameter of the axon is close to zero at that point ($A \approx 0$) or there is little cellular structure at x holding the axon together ($g \approx 0$). In either case, the applied tension causes rapid deformation at x but forces are quickly absorbed into the substrate and are not proximally propagated. The tension gradient causes a sharp jump in the velocity of materials at x making the axon prone to 'rupturing'. Equation 1.10 demonstrates this behavior, as is now shown. First, for $x = L(t)$, we see that

$$\lim_{G\to 0^+} v\left[L(t), L(t); G\right] = \frac{F_L}{\sqrt{\eta}} \lim_{G\to 0^+} \frac{1}{\sqrt{G}} \tanh\left[L(t)\sqrt{\frac{\eta}{G}}\right] = \infty. \tag{1.13}$$

Now, for $x \in [0, L(t))$, we make the substitution $H = \sqrt{\frac{\eta}{G}}$ and take the limit as $H \to \infty$:

$$\begin{aligned}
\lim_{G\to 0^+} v\left[x, L(t)\right] &= \frac{F_L}{\sqrt{\eta}} \lim_{H\to\infty} \frac{H \sinh\left[Hx\right]}{\sqrt{\eta}\cosh\left[HL\left(t\right)\right]} \\
&= \frac{F_L}{\eta} \lim_{H\to\infty} H\frac{e^{Hx} - e^{-Hx}}{e^{HL(t)} + e^{-HL(t)}} \\
&\leq \frac{F_L}{\eta} \lim_{H\to\infty} H\frac{e^{Hx}}{e^{HL(t)}} \qquad (1.14) \\
&= \frac{F_L}{\eta} \lim_{H\to\infty} He^{H(x-L(t))} \\
&= 0
\end{aligned}$$

since $x - L(t) < 0$.

1.3.2 Parameter Values

Average values for G, g, and η were found via methods described in Materials and Methods. The average value of G was found to be $\bar{G} = 3.9 \times 10^7 \pm 3.0 \times 10^7$ g·μm·h^{-1} (mean $\pm$ SD, $n = 31$). The intrinsic value g for each axon at each thirty minute period was found by dividing G by the average cross-sectional area of the axon distal to the initial point of adhesion. We found this value to have an average of $\bar{g} = 1.3 \times 10^7 \pm 8.5 \times 10^6$ g·μm^{-1}·h^{-1} (mean $\pm$ SD, $n = 31$) which is equivalent to $3.6 \times 10^6 \pm 2.4 \times 10^6$ Pa·s (1 Pa·s = 3.6 g·μm^{-1}·h^{-1}). The average η value was $\bar{\eta} = 9.6 \times 10^3 \pm 7.5 \times 10^3$ Pa·s (mean $\pm$ SD, $n = 28$). In three cases there were an insufficient number of mitochondria proximal to the initial point of adhesion to be able to fit a significant value of η.

1.3.3 Model Predictions

As a test of the model, we plotted Eq. (1.10) with the calculated average parameters and a force of 200 μdynes against data from neurons growing naturally on laminin / polyornithine substrates. Using velocity measurements from thirteen arbors of six growing axons ($N = 563$), we observed significant LVT of the distal axon and found a strong correlation between our model and the actual level of stretching (Fig. 1.6 A). An interesting observation in this process was that the majority of docked mitochondria in the proximal regions, where growth cone generated forces have little effect, moved in the retrograde direction.

Figure 1.6: Whether Axonal Stretching Occurs Along the Length or Only at the Tip Depends on the Values of G and η - (A) Comparison of the base model with data from axons growing naturally on laminin / polyornithine substrates. Velocities of docked mitochondria from arbors of six different neurons were recorded ($N = 563$). Average velocities were then calculated at the growth cone and for each 25 μm segment proximal. Comparison of the average velocities with the base model yielded an R^2 value of 0.81. (B) and (C): Model sensitivity to parameters. (B) For large values of η (strong adhesions), forces are dissipated quickly and very little bulk transport is observed. When adhesions are absent ($\eta = 0$) the force is not dissipated and the velocity profile is linear (like a series of dashpots). $L = 200$ μm, $F_L = 200$ μdynes, $G = \bar{G}$. (C) Large G values cause low effective friction (η/G) and result in low velocity at the growth cone with little force dissipation along the length. Small G values lead to high velocities near the source of tension. Because effective friction is high, forces are quickly dissipated and velocity of materials goes to zero a short distance away from the growth cone. This behavior leads to rapid elongation, but possible rupturing of the axon. $L = 200$ μm, $F_L = 200$ μdynes, $\eta = \bar{\eta}$.

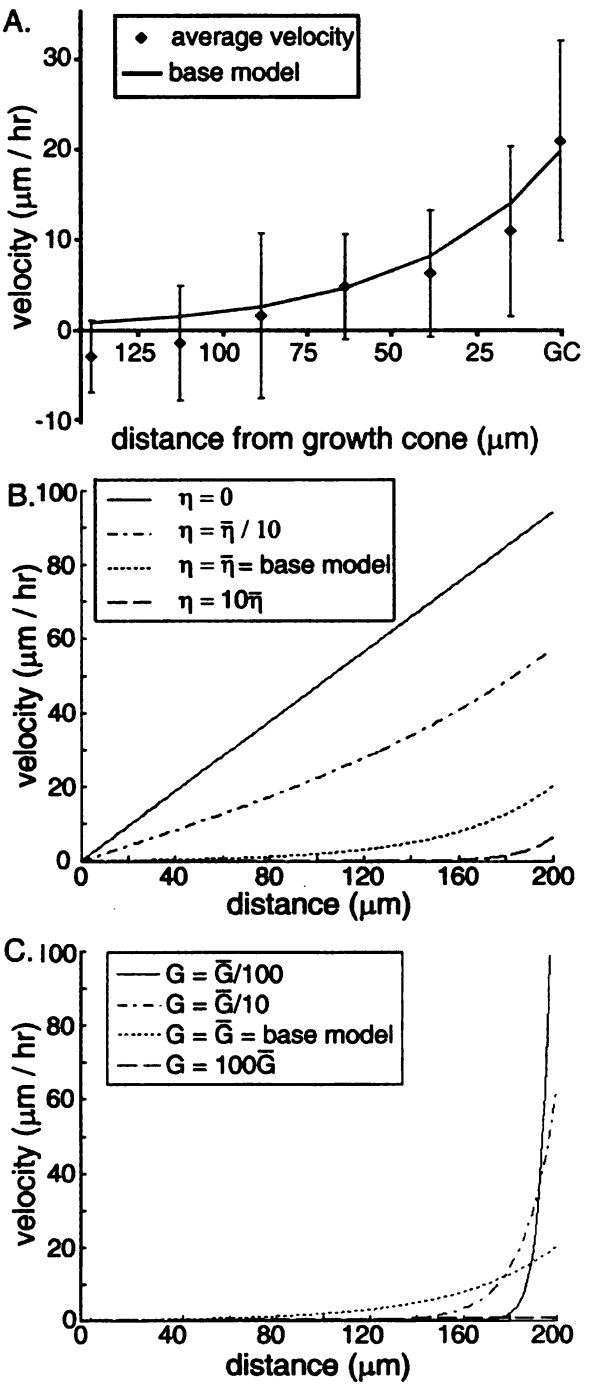
A.
average velocity
base model
velocity (μm / hr)
30
20
10
0
-10
125
100
75
50
25
GC
distance from growth cone (μm)
B.
η = 0
η = η̄ / 10
η = η̄ = base model
η = 10η̄
velocity (μm / hr)
100
80
60
40
20
0
0
40
80
120
160
200
distance (μm)
C.
G = Ḡ/100
G = Ḡ/10
G = Ḡ = base model
G = 100Ḡ
velocity (μm / hr)
100
80
60
40
20
0
0
40
80
120
160
200
distance (μm)

Figure 1.6:

Having analyzed the behavior of the velocity profile for extreme values of G and η, we focus on how the velocity profile changes with the parameters. Plots of Eq. (1.10) for varying magnitudes of η and G are displayed in Fig. 1.6 (B, C). As the effect of the neurite / substrate interactions (η) increases, less of the neurite experiences bulk transport, with the most transport occurring near the growth cone. If adhesive forces are not present, then transport behaves as a system of dashpots, with velocity of docked material increasing linearly. Variations in the growth dashpot parameter, G, cause different types of changes. If G is relatively large, the neurite is too stiff and realistic forces are insufficient to produce significant bulk transport or elongation (Fig. 1.6 C, *dashed line*). As the neurite becomes more fluid (G decreases) both bulk transport and elongation are observed. Notice that, in the presence of adhesions, transport is still minimal in the proximal axon. Decreasing G further, transport occurs only in the distal axon with a steep gradient (Fig. 1.6 C, *solid line*). An extremely small value of G represents an axon that is too fluid to withstand tension. This neurite will see a sharp change from zero velocity of materials in the majority of the axon to extreme stretching near the growth cone. The neurite offers little resistance to tension but the tension dissipates immediately, possibly leading to rupture at the point where the tension is applied. An observed axonal rupture is explained by this model as G being locally too small to handle the forces in that region.

In the towed growth experiments, where the velocity of axonal elongation exceeds the normal rate of elongation, axons thinned. In contrast, in the naturally growing axons dramatic thinning was not observed. This suggests that there is some rate of mass addition that occurs along the length of the axon which normally prevents axonal thinning, but that when the normal growth rate is exceeded there is initially a thinning of the axon. Our simulation of a growing axon without mass addition is consistent with this observation (Fig. 1.7). The force generated at the growth cone (200 μdynes) causes lengthening of the axon and thinning. Force dissipation due to

adhesions restricts thinning to the distal region and, in a short amount of time, the diameter becomes extremely small at the growth cone. Comparison of our simulation and the profiles of naturally growing axons implies that mass addition counteracts stretch-induced thinning.

The model predicts that for a given set of parameters (F_L, G, and $\eta > 0$) a growing axon achieves a maximum velocity of axonal elongation (Fig. 1.8). Further, it shows that there is a characteristic velocity profile that advances with the growth cone and is non-zero for some fixed length $\bar{L}$. For very short axons, forces generated at the growth cone are not fully dispersed along the length and the velocity profile is nearly linear. As the axon elongates, the actual velocity of the materials near the growth cone increases to its maximum value $v_{\max} = F_L/(G\eta)^{1/2}$ and the velocity profile attains its exponential shape. Once the axon is long enough ($L \geq \bar{L}$) so that force dissipation causes the velocity to reach zero prior to the growth cone, the velocity curve behaves, over time, as if it were shifting to the right.

1.4 Discussion

How axons elongate has been a central debate in neurobiology for decades. Tip growth is generally accepted as the method [26, 36], but stretching is observed along the axons of *Xenopus* neurons and in the distal axon of chicken sensory neurons [64, 69, 77]. It is well agreed that growth cones generate tension [50] and cells are viscoelastic materials [38] that adhere to substrates [23], thus it seems reasonable that axons stretch in response to forces. To test this we use direct observation of the movements of docked mitochondria and physical manipulation of the neurons via axonal towing to test whether axons stretch in response to force application at the growth cone and to determine the normal parameters for the viscosity of the axon and the level of adhesion to the substrate. We then mathematically model the axon

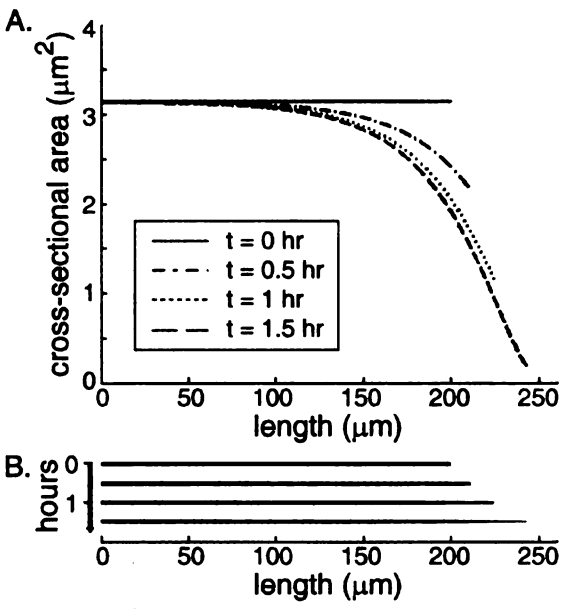

Figure 1.7: Without Mass Addition, Axons Thin when Stretched — To examine the necessity of intercalated mass addition, an Euler's implementation was employed where cross-sectional area was allowed to vary while the axon lengthened. The growth dashpot parameter G and the constant of friction η were initially set at physiological levels ($g = \bar{g}$, $A = \pi\ \mu m^2$, $\eta = \bar{\eta}$). During lengthening, G varied with the cross-sectional area while η was held constant. Here we simulated an axon that was initially 200 μm long, with a uniform axonal diameter of 2 μm, and a constant force of 200 μdynes applied at the growth cone. The simulations ran until the cross-sectional area became smaller than 0.05 μm^2 at any point. (A) The profile of the cross-sectional area over the first 1.5 hours of growth demonstrates that the force gradient due to cell-substrate adhesions leads to non-uniform thinning in the distal region. (B) A scale representation of the axon over the first 1.5 hours of growth strongly suggests that intercalated mass addition occurs to prevent thinning.

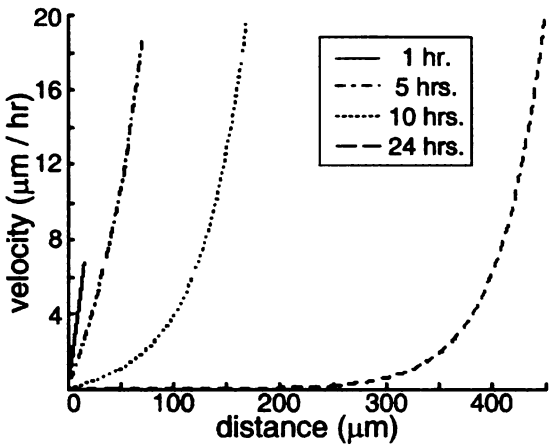

Figure 1.8: Nascent Axons Elongate Slowly — A simulation of an initially short axon ($L_0 = 10$ μm) under tension shows the velocity profile of an elongating axon. Transport is present along the length when the axon is short and the elongation rate is low. As the axon grows, the velocity of elongation increases until the length of the region where transport is observed reaches a maximum (here, roughly 100 μm). The velocity profile then translocates with an increasing lagging zone in the proximal axon where no transport is observed. $F_L = 200$ μdynes, $G = \bar{G}$, $\eta = \bar{\eta}$.

as a viscoelastic fluid, based on the work of Dennerll et al., which suggests that tip growth occurs when the forces generated at the growth cone are weak, the adhesions along the axon are strong, or the viscosity of the axon is high.

While it is well accepted that force application at the growth cone leads to axonal elongation [11, 99], whether it leads to stretching of the axon has not been addressed. Anterograde LVT of the distal cytoskeleton, as previously documented [64, 23, 70, 69, 77], was present in our control experiments (Fig. 1.6 A). To test the effects of external force application, we monitored the movement of docked mitochondria along the axon while towing. We observed that mitochondria along the axon translocated anterogradely (Fig. 1.2 E) and with a velocity profile that was strongly non-linear (Fig. 1.2 F). The velocity of movement of the docked mitochondria was directly linked to the rate of towing. When axons were towed at a rate of 50 μm h^{-1} the velocity of mitochondrial movement next to the growth cone was ≈ 40 μm h^{-1} (Fig. 1.2 F) and

when towing occurred at 100 μm h^{-1} the velocity of movement next to the growth cone was $\approx$ 90 μm h^{-1}. Together these data provide the first direct evidence that the external application of forces to the growth cone leads to stretching of the axon.

The key test for our model was to examine the velocity profile in regions of the axon that were unattached (Fig. 1.4 A) and attached to the substrate (Fig. 1.4 B). If our model is correct then the velocity profile would be linear in the unattached regions and would be non-linear in the attached regions. We found the data support a model where adhesions along the axon dissipate forces exerted at the growth cone. By estimating the cross-sectional area of the axon (Fig. 1.5), we calculated the true viscosity (g) to be $3.6 \times 10^6 \pm 2.4 \times 10^6$ Pa·s on average. This measurement is comparable with observations made in fibroblasts which suggest the cytoplasmic viscosity is between 10^2 and 10^6 Pa·s [94]. The elevated value reported here is not surprising given that axial viscosity of a neurite is a function of deformation-resistant features such as cross-linked cytoskeletal elements within the axon [38, 39, 83]. An important control was to compare the velocity profile of docked mitochondria along the axon during normal axonal elongation with the velocity profile prediction based on our direct estimates of G, η, and the magnitude of force at the growth cone. That our model fits well with the data (Fig. 1.6 A) illustrates its relevance and predictive power.

The strengths of cellular adhesions have previously been measured by means of centrifugation [58] and fluid flow [53] or by the amount of force required to pry a cell from the substrate [98]. While those techniques are useful for determining relative adhesiveness, the results are difficult to apply to other systems because they are in indirect units (e.g. fraction of adherent cells after centrifugation and duration of blasting through a pipette required to detach a cell) or are a complex function of the applied force, viscoelastic properties of the cell, and adhesion. Our description is unique in that it is the first direct estimation of the level of adhesion of an axon to a

substrate. Based on our estimation of the level of cellular adhesion to the substrate $\left(\eta = 9.6 \times 10^3 \pm 7.5 \times 10^3 \text{Pa} \cdot \text{s}\right)$, we can predict the traction force an axon exerts on the substrate vs. distance from the growth cone. For example, given an endogenous force of 2 nN in chicken DRG growth cones and an apparent axonal viscosity of 1.1×10^7 Pa·s, we predict that a 1 micron region of axon 10 microns from the growth will exert 26 pN of traction force. In situations where axons are elongating by tip growth, we predict that traction force due to adhesions will drop off very rapidly away from the growth cone and will be zero along the axon. In contrast, traction forces will decline gradually towards the cell body in cases where axons are elongating by stretching (i.e., in DRG neurons grown on laminin / polyornithine). Further experiments monitoring axonal elongation using plastic pads mounted on cantilevers [34] or micropatterned elastomer substrates [19] will allow our model and predictions to be directly tested.

A key finding of Chang et al. [23] was that the substrate on which a neuron was grown determined if the axons grew by stretching or tip growth. Furthermore, axons that stretched grew more quickly than axons that were attached to the substrate. Our model behaves in a similar fashion (Fig. 1.6 (B, C)). A possible insight to the problem of axonal elongation our model suggests is that axons typically extend by stretching of the distal axon, but when the adhesions along the axon are strong, stretching only occurs at the tip. While tip growth and axonal stretching appear to be qualitatively different, our model suggests tip growth may just be a special case where stretching is restricted to the growth cone.

The tip growth model predicts that axonal elongation occurs by the addition of new mass at the growth cone. Depending on the school of thought, this occurs either through microtubule polymerization at the growth cone [26, 36] or the addition of new microtubules by Stop-and-Go Transport [12]. In both cases, increasing the amount of microtubule polymer has the predicted effect of increasing the rate of axonal

elongation. Our model predicts, for values of G and η which are reasonably greater than zero, that the elongation rate of an axon attached to the substrate is proportional to $F_L\,(G\eta)^{1/2}$. Thus an increase in G due to polymerization leads to a decline in the velocity of elongation. In other words, the rate of axonal elongation is sensitive to the viscosity of the axon: the higher the viscosity, the slower the rate of axonal elongation. This suggests an explanation to the counter-intuitive observation that an increase in microtubule polymerization through the application of the drug taxol slows the rate of axonal elongation [54, 6]. Our model predicts that an increase in microtubule mass along the length will slow the rate of axonal elongation by increasing the viscosity of the axon (Fig. 1.6 C). In the case of taxol application, it suggests the axons elongate more slowly because tubulin is converted to microtubules along the length and the viscosity (G) of the axon increases.

Related is the question of why axons are thin during elongation and then increase in diameter after synapse formation [84]. Our model suggests the apparent viscosity (G) of the axon is a function of axonal diameter, thus thin axons will grow more quickly given a level of tension at the growth cone. The relationship between axonal diameter and rate of growth may also explain why thin neurites of Aplysia neurons ($2-6$ μm in diameter), but not the main axonal trunk ($20-50$ μm) advance in tissue culture [57]. How axonal elongation varies with axonal viscosity and diameter has not been systematically addressed experimentally and will be an interesting avenue for future research.

The observation that rapidly advancing growth cones are small and growth cones that pause enlarge [35] further suggests that mass addition does not control the rate of axonal lengthening. In the context of our model, for a given rate of mass addition there exists a critical level of stretching that would result in no change in diameter. The aforementioned observations could be interpreted such that rapidly advancing growth cones are small because they undergo a super-critical degree of

stretching, and paused and slowly advancing growth cones enlarge because the level of stretching is sub-critical. In this context, our assumption that G is constant during elongation is equivalent to saying that the rate of mass addition increases with the rate of lengthening.

Where mass addition occurs during axonal elongation is a long-standing problem [9]. A simulation of an axon growing by stretching revealed that, without mass addition, thinning of the distal region to a very small diameter (< 250nm) occurs in a matter of hours (Fig. 1.7). Because axons grown naturally on laminin are not observed to significantly thin, this suggests that mass addition is occurring along the distal axon.

Any model of axonal elongation must account for the observation that axons tend to lengthen at some average rate that does not seem to significantly vary with the length of the axon [29]. The inclusion of adhesions along the axon in our model produces this behavior, preventing unbounded elongation rates (Fig. 1.8). Presuming that growth cones generate similar amounts of force in short and long axons, the region of axonal stretching and force dissipation is similar regardless of the length of the axon and advances with the growth cone. This creates a region of axonal stretching in the distal axon, yet a stationary cytoskeletal framework in the proximal axon.

There are several potential shortcomings of our model. The first is that we place mass addition as a dependent variable instead of an independent variable that controls the rate of axonal lengthening. While we based this on our interpretation of the available experimental data as outlined in the introduction, further studies are required to definitively demonstrate the site of mass addition along the axon. The second limitation is that our model is one dimensional and does not address the two or three dimensional problem of axonal guidance. We think this is an exciting question [3], but deeper knowledge with regards to the interactions between the axonal shaft and substrate will be required, in particular to determine whether adhesions are

discrete or continuous. The third potential limitation is we treat the axon as a stiff viscoelastic fluid and ignore elastic behaviors. We agree that an understanding of those processes is important especially in the context of the problem of axonal guidance in short time scales up to several hours. The final limitation is that we do not consider the dynamic aspects of axonal elongation. For example, it is well accepted that sensory neurons do not thin over extended periods of time during elongation on glass coverslips coated with laminin [10], in vivo during lengthening forced by bone elongation [1], or in vitro during towed growth at rates as high as 8 mm/day [74]. Thus in our model we hold axonal diameter, G, and η to be constant for the steady state solution. Yet as is seen in Fig. 1.5 (A, D), which is a representative example, axonal diameter appears to decrease during lengthening caused by towing. We believe this thinning might occur because the rate of mass addition does not rapidly adjust to changes in the rate of axonal lengthening [74]. These results suggest that future models which incorporate dynamic aspects (such as changes in the velocity of elongation) may also need to include changes in axonal diameter, g, and in mass addition as functions of the rate of axonal lengthening.

1.5 Conclusion

As axons are viscoelastic, forces may play a role in elongation and bulk transport of materials. We have proposed a model which suggests that the extent of neuronal lengthening is dictated by tension, the physical viscoelastic properties of the axon, and the axon's surrounding environment. The model suggests that tip growth may be a special case where axonal stretching is restricted to the growth cone because the level of adhesions along the axon are very high, the viscosity or thickness of the axon is large, or force generation in the growth cone is weak.

Chapter 2

Modeling Mitochondrial Dynamics During *In Vivo* Axonal Elongation

2.1 Introduction

Protein synthesis and axonal transport are vital components in the healthy growth of neurons. Newly synthesized cellular materials are necessary for, among other things, elongation and upkeep of the axonal shaft. For a given cell, protein synthesis in this process could either be constant or variable and either predetermined by a genetic developmental program or regulated through external inputs. How neurons control cellular production during the growth of axons shapes the way one approaches current problems such as nerve repair. Other factors which may play a role in the process are microtubule polymerization rates, tension, and axonal transport. The ability to understand the interactions of these qualities (i.e. to develop accurate models) is crucial in the development of techniques for repairing damaged nerves.

In pre-synaptic neurons, axonal elongation is the result of a complex interplay between force generation at growth cone that pulls the axon forward [50, 64, 72], pushing forces due to microtubule and actin polymerization and depolymerization

[8, 15, 55], and the effects of cytoskeletal dynamics and motor protein activity along the axonal shaft [4, 67]. Because inhibiting either protein synthesis or microtubule polymerization blocks axonal elongation [6, 30], while disruption of the contractile actin cytoskeleton can in some cases accelerate axonal elongation [8, 49, 55], most models of axonal elongation have focused on the role of protein production by the cell body, the transport of material to the growth cone, and microtubule addition at the growth cone as the key determinates of the rate of axonal elongation. A popular assumption in elongation models is that the flux of new materials into the axon from the cell body is an independent variable that presumably could vary over time, but is not a direct function of axonal length or rate of elongation [36, 46, 62, 91]. These models assume that the level of production at a given time point is set at some predetermined level and drives axonal lengthening.

In this chapter we focus on post-synaptic neurons where axons lengthen based on the growth of the organism as a whole [11, 93, 78]. Thus, adult neurons have no control over the rate of axonal elongation or the nerve's final length. As neurons constantly generate tension that minimizes axonal length both before and after synapse formation [90], it follows that increases in the length of the axon are the result of forces generated by an increase in body size. Consistent with the view that neurons respond to forced lengthening by increasing the production of new material are studies that have shown that axons are able to maintain viability and increase their caliber when artificially stretched to remarkable lengths [1, 74, 73]. For these reasons it would be useful to have a model where influx is allowed to vary over the course of elongation. Thus in this paper we assign mass production as a variable that is dependent on the length of the nerve and aim to model the manner in which flux of new materials into the axons is modified to accommodate changes in nerve length and density.

While most studies have focused on the production and transport of cytoskeletal

material in the axon, we focus on mitochondria for several reasons. The first is that they play a central role in the progression of Parkinson's disease [59]. Future work on this topic requires a rigorous characterization of normal mitochondrial behavior. The second is that the transport of mitochondria seems to be a function of the mitochondrial life cycle in the cell (Fig. 2.1). Thus further characterization of their transport is of broad interest to the basic cell biology of neurons [22, 32, 63]. Third, the transport and distribution of mitochondria, as compared to microtubules, is far easier to study because it is possible to resolve individual organelles along the nerve. Fourth, as mitochondria are 'housekeeping' organelles required for normal cellular function, and are uniformly distributed along the axon [63], they make an excellent proxy for studying the general production, transport, and distribution of material along the axon.

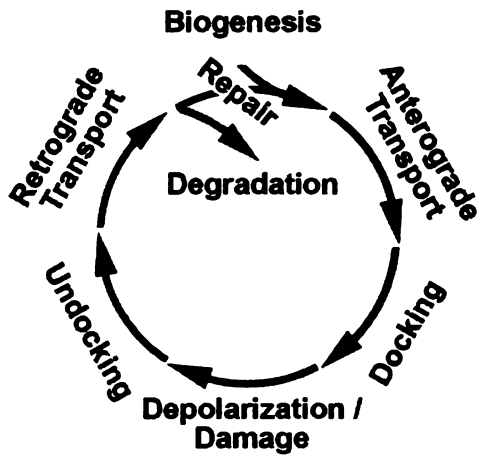

Figure 2.1: Life Cycle of Mitochondria — We hypothesize that new mitochondria are made in the cell body and have a high potential. These mitochondria are transported along the axon and then dock in regions with unmet metabolic demand. Following damage to the mitochondria, they lose potential. This induces signals to undock and return to the cell body, where mitochondrial degradation and repair occurs.

In addition to the production of new material to support structural changes, there

is a constant demand for new materials to replace those lost in the normal functioning of the cell. Many models do not factor in degradation along the length, often because the main focus of those studies is transport [14, 86]. For modeling over long time periods on the scale of the half-life of a material, degradation will affect both demand on the soma and the transport (flux) profile, and must be considered. In regard to the degradation of mitochondria, there has been no recent study of mitochondrial half-life, so we provide our own analysis for this parameter of our model. What mitochondrial half-life in the axon reflects has yet to be clearly defined. Based on our prior work, which demonstrated a correlation between mitochondrial potential and the direction of transport in the axon [63], one possibility is that mitochondrial half-life in the axon reflects the rate of mitochondrial degradation. Nonetheless, mitochondria with a high potential also undergo retrograde transport and it is possible that mitochondria are repaired instead of degraded in the cell body. It is likely that this variable will be a complex function of the rate of mitochondrial depolarization, degradation, repair, or some other function that has yet to be discovered. For the purpose of our discussion, the major point is that mitochondria do not stay in the axon indefinitely, but are removed over time at a rate that has a significant impact on mitochondrial distribution.

Direct measurements of axonal materials will be able to confirm/dispute the assumptions and predictions of previous models and aid in the development of a model of our own. In an effort to accomplish this, we have directly measured mitochondria and their movements during the development of the medial nerve in 1st, 2nd, and 3rd instar Drosophila larvae. Specifically, we have tracked increases in both nerve length and mitochondrial density during the 96 hour developmental period. Using data from this system and a newly developed mathematical model, we answer the following questions about axonal elongation in Drosophila: 1) Does nerve diameter vary spatially, and does it increase during the lengthening of mature neurons? 2) What

is the half-life of a mitochondrion in medial segmental nerves? 3) What profile of protein synthesis is necessary to sustain the observed behavior of these neurons? Our results imply that the neuron responds to lengthening and its absolute length such that uniform density of material is homeostatically maintained by active regulation of the production of cellular materials during maturation.

2.2 Materials and Methods

2.2.1 Drosophila Stocks and Culture

Standard cornmeal fly media was used and all stocks maintained at 25°C. The UAS-mtGFP line was a gift from Dr. William Saxton, University of California, Santa Cruz.

2.2.2 Image Acquisition and Analysis of Axonal Transport

Crawling 1^{st}, 2^{nd}, and 3^{rd} instar *Drosophila* larvae were selected and anaesthetized in halocarbon oil 700 (Sigma) with 10–25% chloroform, titrated to levels just sufficient to inhibit significant muscular contraction. The larvae were then mounted between a slide and coverslip and were imaged for no more than 15 min at $\sim$ 25°C. With the exception of Figure 2.5, all images were acquired on a swept field confocal microscope with NIS software using a Nikon TE2000-E inverted microscope and a PlanApo 60X oil objective, NA 1.4. The aperture and exposure were set at 70-slit and 100 ms, respectively, and images were captured at 2 s intervals for total time of 7 min for a time-lapse series. NIS files were opened in ImageJ, and frames were aligned using StackReg plugin with rigid body settings. The two medial nerves at the base of the ventral nerve cord were selected for each analysis, cropped and rotated, using TJ Rotate with cubic-B-spline interpolation, so that the nerves were always oriented

horizontally with the cell body on one side and the synapse on the other. These images were re-sliced and z-projected using the sum-slices option to generate kymographs. The kymographs were opened in Adobe Photoshop, image color depth was converted from 16 bits / pixel to 8 bits / pixel and color inverted to facilitate better visibility of transport events.

For Figure 2.5 the image was acquired with a spinning-disk confocal fluorescent microscope controlled by MetaMorph software (Universal Imaging) with a 20× air or 60× oil objective (Nikon) and a cooled CCD camera (model ER; Hamamatsu). Confocal stacks were acquired, opened in ImageJ (National Institutes of Health), z-projected, and then assembled into a montage in Photoshop. Timelapse series were acquired at 2 s intervals and processed as described above.

2.2.3 Nerve Length and Mitochondrial Density

The length of each nerve was calculated as the measured distance from the ventral nerve cord to where the nerve bifurcates close to the region of synapse formation. To determine the densities of mitochondria along the length of nerves, 3D reconstructions of nerves where mtGFP was expressed were analyzed and mitochondria were counted (Fig. 2.2). Mitochondria were grouped in 100 μm bins and the densities were plotted for each instar (Fig. 2.3). Average mitochondrial density was calculated for each instar (Fig. 2.4B) to estimate the manner in which density changes during development.

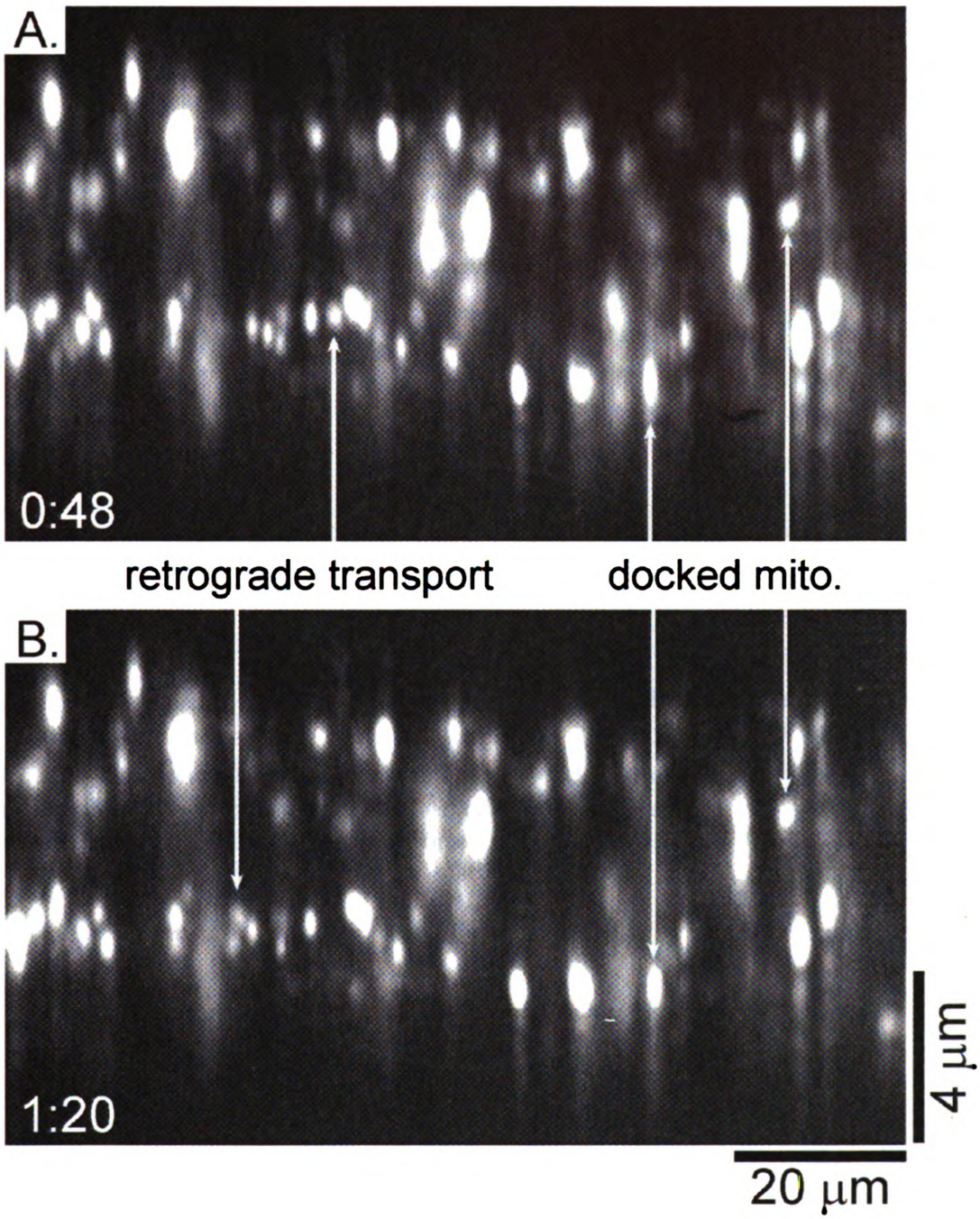

Figure 2.2: Estimation of mitochondrial size using fluorescence levels – To determine the half-life of mitochondria in *Drosophila* larvae, we first estimated the average size of docked and transported mitochondria. Using movies of transport we measured the total intensity of a mitochondrion using an ovular tool and the measure command in ImageJ (background intensities were subtracted from this measurement). Arrows point to the same mitochondria at different times.

Figure 2.3: Mitochondrial Density Profiles for 1^{st}, 2^{nd}, and 3^{rd} Instar Larvae – Density measurements were binned into 100 μm segments for 1^{st} (A), 2^{nd} (B), and 3^{rd} (C) instar *Drosophila* larvae. The averages for each bin are plotted where the error bars represent the standard deviation. Average density is seen to increase during development, with insignificant variation from bin to bin.

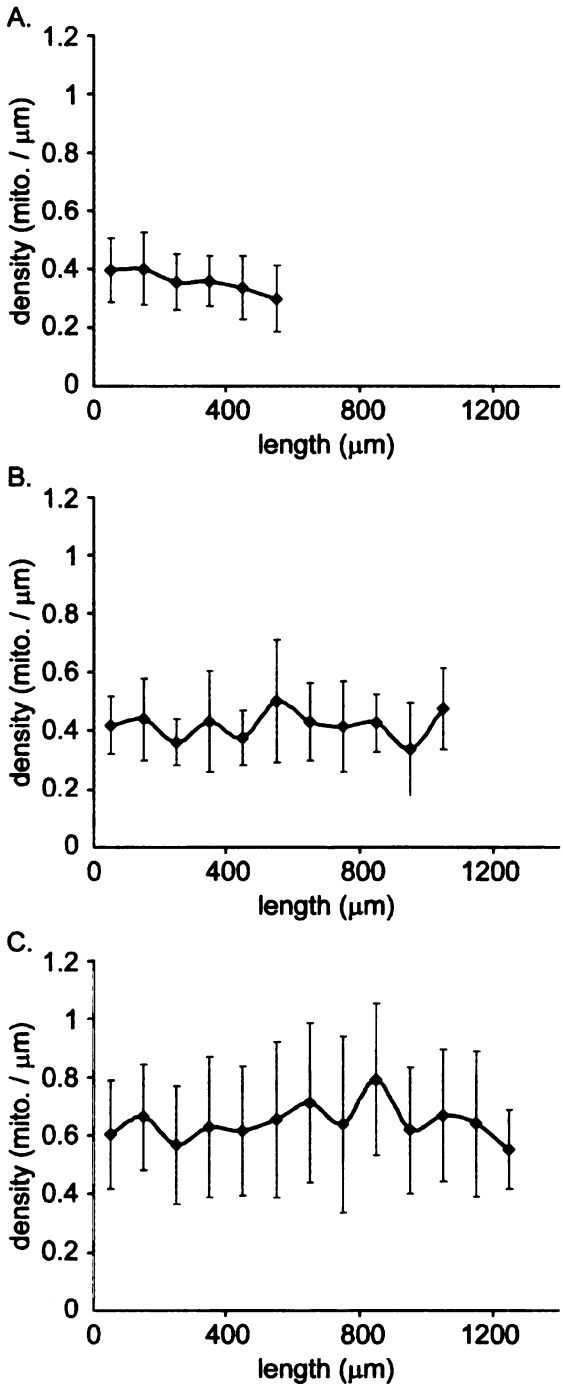
A.
density (mito. / µm)
1.2
1
0.8
0.6
0.4
0.2
0
0
400
800
1200
length (µm)
B.
density (mito. / µm)
1.2
1
0.8
0.6
0.4
0.2
0
0
400
800
1200
length (µm)
C.
density (mito. / µm)
1.2
1
0.8
0.6
0.4
0.2
0
0
400
800
1200
length (µm)

Figure 2.3:

Figure 2.4: Nerve Length and Mitochondrial Density Increase Over Time – Both nerve length and mitochondrial density are observed to increase as *Drosophila* larvae mature. Arrowheads in A, B denote the approximate time, in development, of synapse formation when the mode of growth switches from neurite growth to towed axonal growth. (A) The average lengths of neurons of each instar are plotted at the approximate midpoint time of each instar. Average lengths were found to be 468 ± 124 μm (average $\pm$ s.d., $n = 12$) for the 1^{st} instar, 631 ± 262 μm (average $\pm$ s.d., $n = 11$) for the 2^{nd} instar, and 963 ± 163 μm (average $\pm$ s.d., $n = 11$) for the 3^{rd} instar. The growth rate constant γ is estimated to be 9.24 μm h^{-1}. (B) Mitochondrial density data is similarly plotted and the average values were found to be 0.34 ± 0.06 mitochondria μm^{-1} (average $\pm$ s.d., $n = 12$) for the 1^{st} instar, 0.37 ± 0.05 mitochondria μm^{-1} (average $\pm$ s.d., $n = 11$) for the 2^{nd} instar, and 0.58 ± 0.08 mitochondria μm^{-1} (average $\pm$ s.d., $n = 11$) for the 3^{rd} instar. The constant of density increase α is estimated to be 4.49×10^{-3} mito. μm^{-1} h^{-1}. (C) Mitochondrial density plotted versus nerve length ($n = 34$). A linear trend is clear, though whether these two factors change independently with time is not clear.

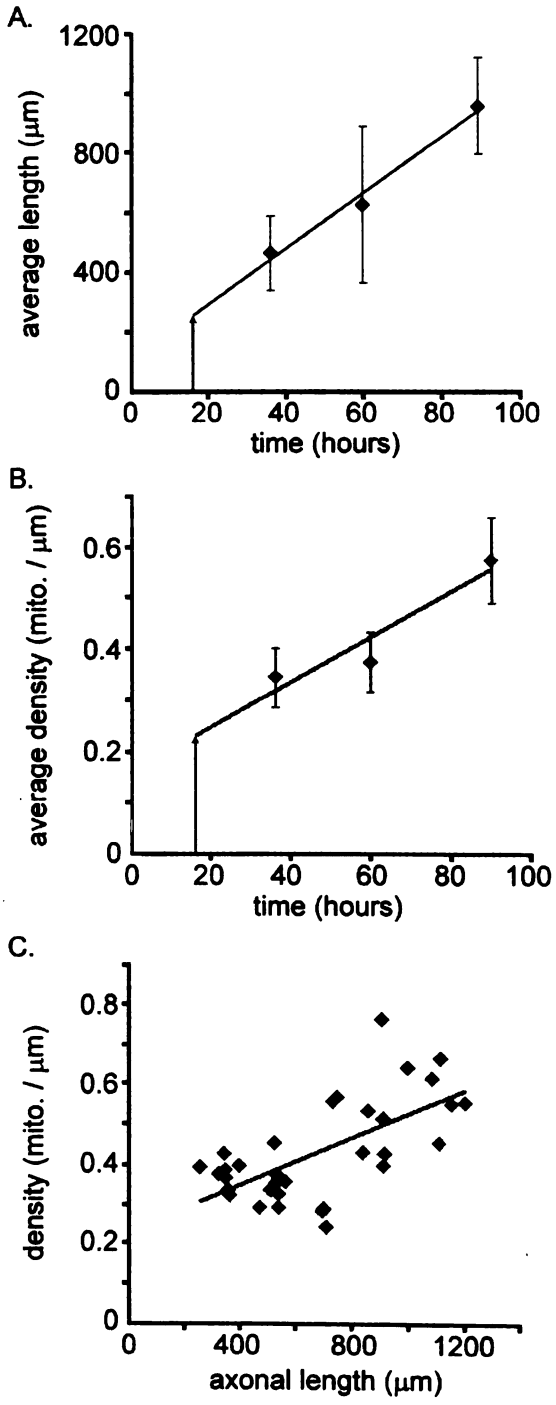
A.
1200
800
400
0
average length (μm)
0
20
40
60
80
100
time (hours)
B.
0.6
0.4
0.2
0
average density (mito. / μm)
0
20
40
60
80
100
time (hours)
C.
0.8
0.6
0.4
0.2
0
density (mito. / μm)
0
400
800
1200
axonal length (μm)

Figure 2.4:

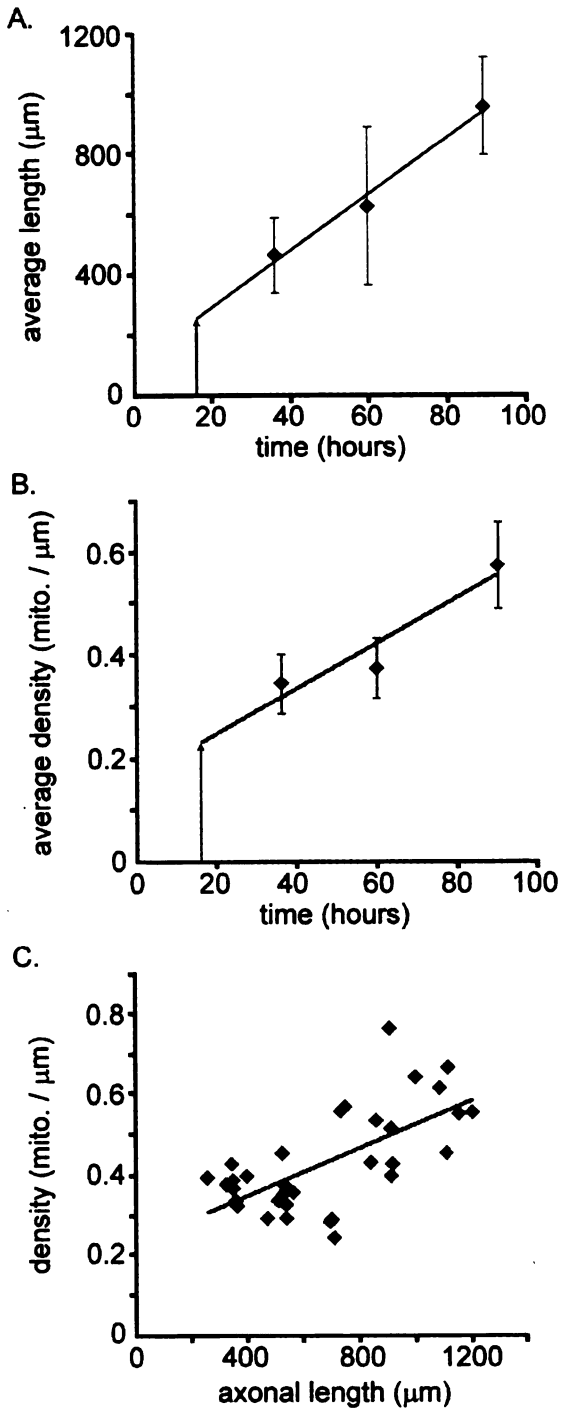
A.
1200
800
400
0
average length (μm)
0
20
40
60
80
100
time (hours)
B.
0.6
0.4
0.2
0
average density (mito. / μm)
0
20
40
60
80
100
time (hours)
C.
0.8
0.6
0.4
0.2
0
density (mito. / μm)
0
400
800
1200
axonal length (μm)

Figure 2.4:

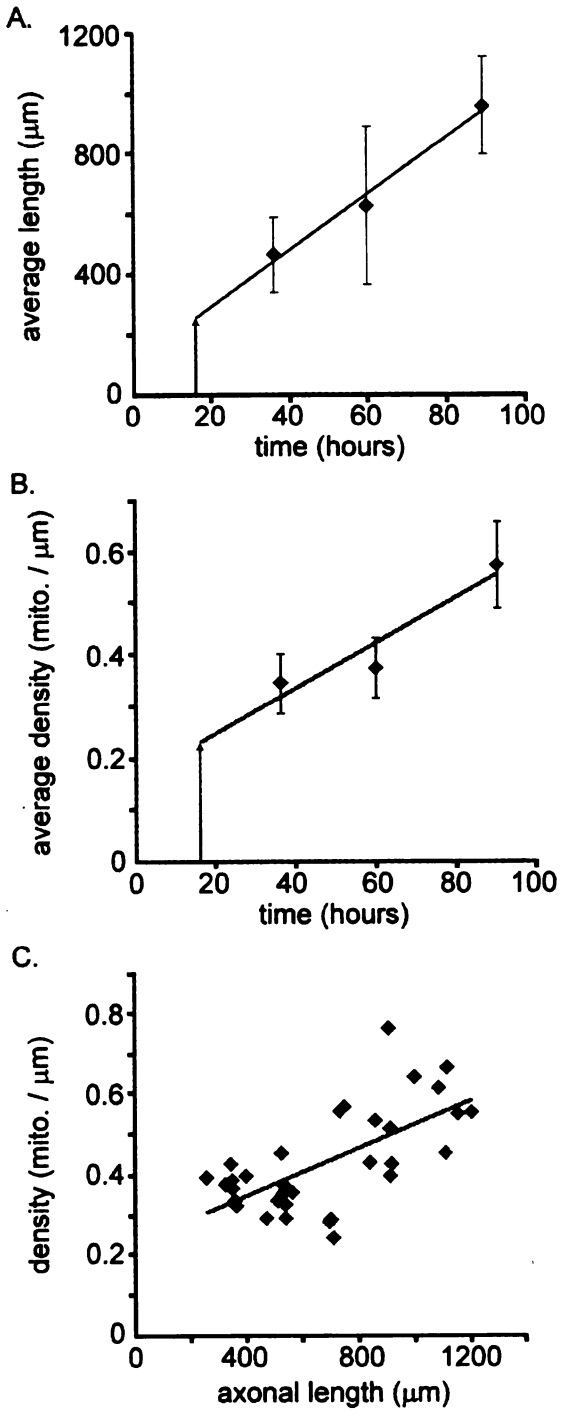
A.
1200
800
400
0
average length (μm)
0
20
40
60
80
100
time (hours)
B.
0.6
0.4
0.2
0
average density (mito. / μm)
0
20
40
60
80
100
time (hours)
C.
0.8
0.6
0.4
0.2
0
density (mito. / μm)
0
400
800
1200
axonal length (μm)

Figure 2.4:

2.2.4 Measurement of Flux and Mitochondrial Half-Life

Multi-kymographs of each trial were generated to analyze retrograde flux of mitochondria in the nerve (Fig. 2.5). Each row of the multi-kymograph represents one z-slice (height level) of the nerve. Arbitrary lines were traced down the multi-kymograph and mitochondria moving right to left that crossed these lines were totaled. This total was divided by the number of horizontal rows used to give the number of retrograde moving mitochondria, and this was divided by the length of the observation to give a value for retrograde flux. Anterograde flux of mitochondria was also measured, but the utility of those measurements are beyond the scope of this thesis and are not reported here.

Figure 2.5: Robust Fast Mitochondrial Transport in *Drosophila* Neurons – mtGFP was expressed in motor neurons and a single optical plane was captured once every two seconds using a spinning disk confocal. (A) A wide view where the neuronal cell bodies in the ventral nerve cord (left side) and the two A8 segmental nerve branches are shown. (B) Examples of the fast transport of individual mitochondria are shown in frames of the movie (times of each frame are zero, 16, and 32 seconds). (C) The multi-kymograph with hand drawn traces over the positions of fast transported mitochondria to illustrate the high level of detail that can be resolved. Retrograde flux was used to quantify degradation while anterograde transported mitochondria represent a combination of slow transport and translation of the nerve due to elongation. Each of the six panels spans a 200 s interval. (D) Summations of the traces of anterograde and retrograde multi-kymographs, excluding slow mitochondrial movements. All scale bars represent a length of 5 μm.

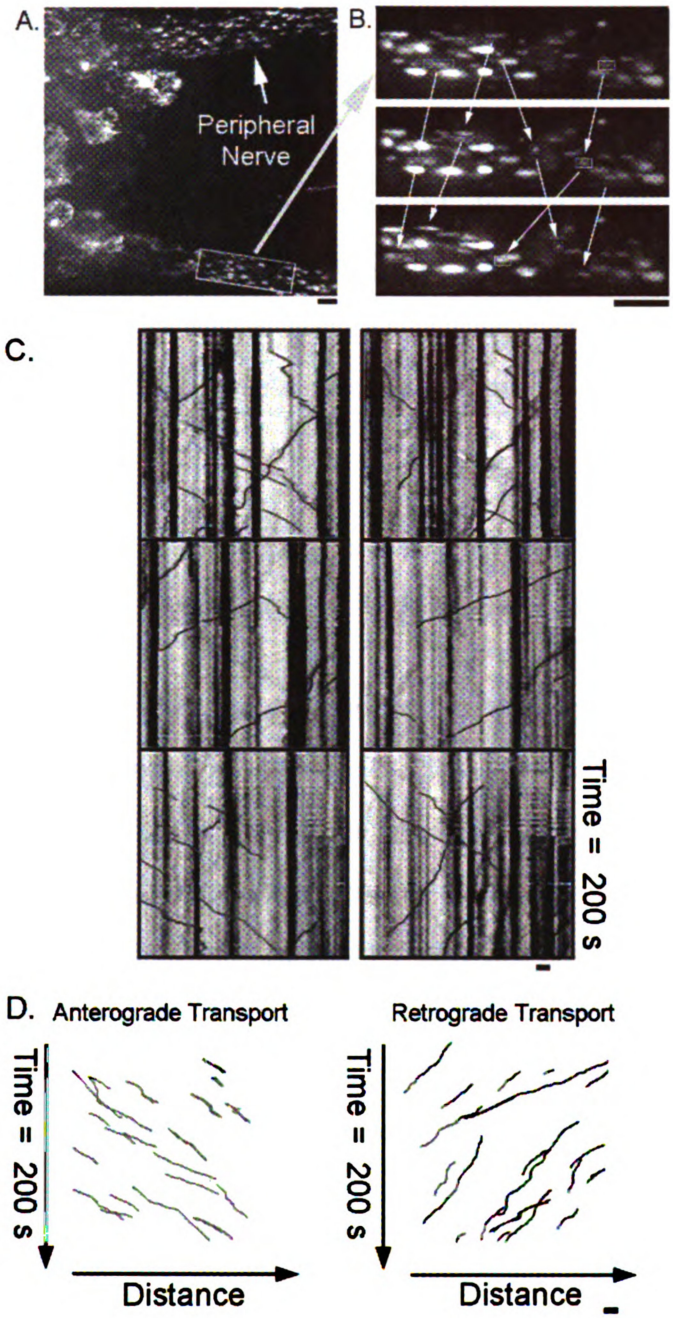
A.
B.
Peripheral
Nerve
C.
Time = 200 s
D.
Anterograde Transport
Retrograde Transport
Time = 200 s
Distance
Time = 200 s
Distance

Figure 2.5:

When measuring half-life we assumed degradation to be proportional to the total amount of mitochondria; $dM_T/dt = \tilde{g} = -M_T/\tau$, where $\tilde{g}$ represents the retrograde flux of mitochondria (treated as negative), M_T represents the total amount of mitochondria, and τ is the characteristic time constant. In vivo movies of mitochondrial transport were analyzed to derive values for $\tilde{g}$ and M_T, from which a value of τ and thus half-life were found. As docked mitochondria were noticeably larger than mitochondria undergoing transport, we used total intensity of all mitochondria as our measure of M_T:

M_T = (number of docked mito.) × (avg. intensity of docked mito.)
+ (number of transported mito.) × (avg. intensity of transported mito.)

The average intensities of docked and transported mitochondria were found by averaging the intensities of a sample of mitochondria from the images. To eliminate bias, the first ten mitochondria to the right of the spatial midpoint of the trial were used. In the case of anterograde and retrograde moving mitochondria, if less than ten were found then all were used. In measuring the intensity, an ovular tool was implemented in ImageJ to surround each mitochondrion. Using the Measure command, the mean intensity of the region was found. A region of equal area, but with no fluorescence, was then measured in a similar way to estimate the average background intensity. Actual intensity of the mitochondrion was calculated by multiplying the area of the region by the difference of these two intensities. The flux term g was also multiplied by the average intensity of retrograde moving mitochondria:

$\tilde{g}$ = −(avg. intensity of retrograde mito.)
× (retrograde flux of mito.)

The units of M_T are intensity, and the units of $\tilde{g}$ are intensity h^{-1}. In this way we were able to estimate the relative amount of mitochondria moving toward the cell body

(i.e. the mitochondria that was degraded). The value of τ was then easily determined and mitochondrial half-life for each trial was calculated as $T_{1/2} = \tau \times \ln(2)$.

2.3 Results

2.3.1 Axonal Length and Mitochondrial Density Increase with Time

Analysis of the medial segmental nerves in 1^{st}, 2^{nd}, and 3^{rd} instar larvae during normal development revealed that axons lengthen in a linear fashion (Fig. 2.4A). Average values for nerve lengths were $468 \pm 124\mu$m (mean $\pm$ SD, $n = 12$) for 1^{st} instar larvae, $631 \pm 262\mu$m (mean $\pm$ SD, $n = 11$) for 2^{nd} instar larvae, and $963 \pm 163\mu$m (mean $\pm$ SD, $n = 11$) for 3^{rd} instar larvae. The associated growth constant was calculated to be $\gamma = 9.24\mu\text{m h}^{-1}$. Average mitochondrial densities were 0.34 ± 0.06 mitochondria μm^{-1} (mean $\pm$ SD, $n = 12$) for the 1^{st} instar, 0.37 ± 0.05 mitochondria μm^{-1} (mean $\pm$ SD, $n = 11$) for the 2^{nd} instar, and 0.58 ± 0.08 mitochondria μm^{-1} (mean $\pm$ SD, $n = 11$) for the 3^{rd} instar. The constant of density increase α was hence found to be 4.49×10^{-3} mitochondria μm^{-1} h^{-1} (Fig. 2.4B). The distribution of mitochondria in each instar was not significantly different from uniform (Fig. 2.3).

2.3.2 Mitochondrial Half-Life in the Nerve

The half-life of mitochondria in 3^{rd} instar larvae nerves was estimated using measurements of total mitochondrial intensity and retrograde flux, the method which is explained in Materials and Methods. Using measurements from six different nerves we found the average half-life to be $T_{1/2} = 35.2 \pm 17.6$ hours (mean $\pm$ SD, $n = 7$). This value was derived from a measured time constant $\tau = 50.8 \pm 25.4$ hours.

2.3.3 Derivation of Model

We use the results obtained by imaging to derive a model for the system which predicts the rate of protein synthesis required to satisfy the needs of an elongating axon. When studying the change in the amount of a substance in a bounded region V, a basic conservation law must be satisfied:

$$\frac{d}{dt}\int_V P(x,t)\,dV = \int_V g(x,t)\,dV - \int_{\partial V} \mathbf{J}\cdot d\mathbf{S} \tag{2.1}$$

where $P(x,t)$ represents the concentration of the substance in V. This equation states that the rate of change of total substance in a region V is equal to the difference of the local synthesis of the substance and the rate of flux of materials out of the region, where g gives the local production / degradation of the substance and $\mathbf{J}$ is the flux of materials. Using the Divergence Theorem,

$$\int_V (\nabla\cdot\mathbf{F})\,dV = \int_{\partial V} \mathbf{F}\cdot d\mathbf{S} \tag{2.2}$$

the relationship can be rewritten as

$$\int_V \left[\frac{\partial P}{\partial t} - g(x,t) + \nabla\cdot\mathbf{J}\right] dV = 0. \tag{2.3}$$

Since the relationship holds on an arbitrary bounded region V, we may simply write

$$\frac{\partial P}{\partial t} = g - \nabla\cdot\mathbf{J}. \tag{2.4}$$

We consider the two factors, g and $\mathbf{J}$ that contribute to changes in the mitochondrial density P. Local synthesis of mitochondria, with regard to the assembly of nuclear encoded proteins, is assumed to be negligible. The function g then solely describes the removal of healthy mitochondria from the axon. Whether this varies over

time is unknown and will be important to investigate more thoroughly in the future, but for this study we assume that mitochondria are cleared at a constant uniform rate, and thus the rate of mitochondrial loss is proportional to the concentration. In the absence of other factors, the differential equation for exponential decay is

$$\frac{dP}{dt} = -kP$$

where $k > 0$. The solution of this equation would be

$$P(t) = P_0 e^{-kt}$$

and the relationship between the half-life of the protein, $T_{1/2}$, and the constant k is $k = \ln 2/T_{1/2}$. Letting $k = \frac{1}{\tau}$ gives the relationship $T_{1/2} = \ln 2 \times \tau$, and we define the degradation function g in terms of τ in this way:

$$g(x,t) = -\frac{P(x,t)}{\tau}. \tag{2.5}$$

Flux of mitochondria due to active transport and low velocity transport (LVT) [64] will also cause changes in the concentration along the length of the axon, but diffusion is omitted since mitochondria are docked tightly to microtubules [44], actin filaments [21], and neurofilaments [92]. Therefore, the term **J** strictly describes the combination of active transport and LVT. Now if we assume that mitochondrial concentration is radially uniform we may write the equation in one dimension:

$$\frac{\partial P}{\partial t} = -\left[\frac{P}{\tau} + \frac{\partial J}{\partial x}\right]. \tag{2.6}$$

We make two assumptions for our model which are based on our experimental observations. The first observation is that nerves tend to lengthen at near constant rates

(Fig. 2.4A), though this rate may vary given the placement of the neuron. The length of the neuron may then be written as a linear equation in t, $L(t) = L_0 + \gamma t$, where γ is the elongation rate. The second observation is that mitochondrial density appears to scale with time since innervations (Fig. 2.4B). There was an observed trend between nerve length and mitochondrial density (Fig. 2.4C), but this relationship does not hold when considering neurons with differing mature lengths (e.g. different segmental nerves). Analysis also revealed that the distribution of mitochondria is effectively uniform $\partial P/\partial x = 0$. We can thus write the mitochondrial density in terms of t by $P(t) = P_0 + \alpha t$. Using this last equation we can substitute $\partial P/\partial t = \alpha$ into our main PDE. Then we may solve Eq. (2.6) for $\partial J/\partial x$ as

$$\frac{\partial J}{\partial x} = -\left[\frac{P_0 + \alpha t}{\tau} + \alpha\right]. \tag{2.7}$$

Since the majority of protein synthesis of nuclear encoded proteins is believed to occur in the cell body [18], in order to maintain a uniformly increasing mitochondrial density, new protein required to support this growth must flow into the axon at $x = 0$. There are three changes in the concentration along the length of the axon that will create a demand for mitochondria. Those needs are (A) replacement of mitochondria that are cleared from the axon, (B) new mitochondria required due to lengthening of the axon, and (C) new mitochondria required to cause an increase in mitochondrial density. Thus new material must enter the axon at $x = 0$ to satisfy these three mitochondrial needs. The latter two changes correspond to changes in cell volume while the former deals with depletion of axonal mitochondrial. The flux requirement, respectively, for each condition is (A) the rate of concentration decrease times length: $P(t)\,L(t)/\tau = (P_0 + \alpha t)(L_0 + \gamma t)/\tau$, (B) the rate of lengthening times the mitochondrial density: $\gamma P(t) = \gamma(P_0 + \alpha t)$, and (C) the rate of increase in density times

length: $\alpha L(t) = \alpha(L_0 + \gamma t)$. Thus we choose our boundary condition to be

$$J(0,t) = \frac{(P_0 + \alpha t)(L_0 + \gamma t)}{\tau} + \gamma(P_0 + \alpha t) + \alpha(L_0 + \gamma t). \tag{2.8}$$

2.3.4 Flux Profile

Solving Eq. (2.7) with the boundary condition (2.8) gives an equation for the flux profile of mitochondria along the length of the axon:

$$J(x,t) = -\left[\frac{P_0 + \alpha t}{\tau} + \alpha\right]x + \frac{(P_0 + \alpha t)(L_0 + \gamma t)}{\tau} + \gamma(P_0 + \alpha t) + \alpha(L_0 + \gamma t). \tag{2.9}$$

The same flux profile can be derived using the less direct boundary condition where only the flux at the growth cone is considered:

$$J(L(t), t) = \gamma(P_0 + \alpha t) \tag{2.10}$$

Equation (2.9) reveals two things; the flux of materials along the axon decreases linearly (Fig. 2.6A), and the rate of influx of materials must increase in a quadratic fashion over time in order to sustain constant increases in axonal length and mitochondrial density (Fig. 2.6B). The flux equation can be written as a quadratic in terms of t as

$$J(x,t) = At^2 + B(x) + C(x), \tag{2.11}$$

where $A = \alpha\gamma/\tau$ and this value, using our estimates, is equal to 8.17×10^{-4}mitochondria h^{-3}.

The model can be applied to axons not only when it is changing in both length and diameter, but also when only one of the two is changing or when neither is changing. Our analysis of length and density in *Drosophila* show that both increase over the three instars. However, as towed growth continues through maturation the diameters

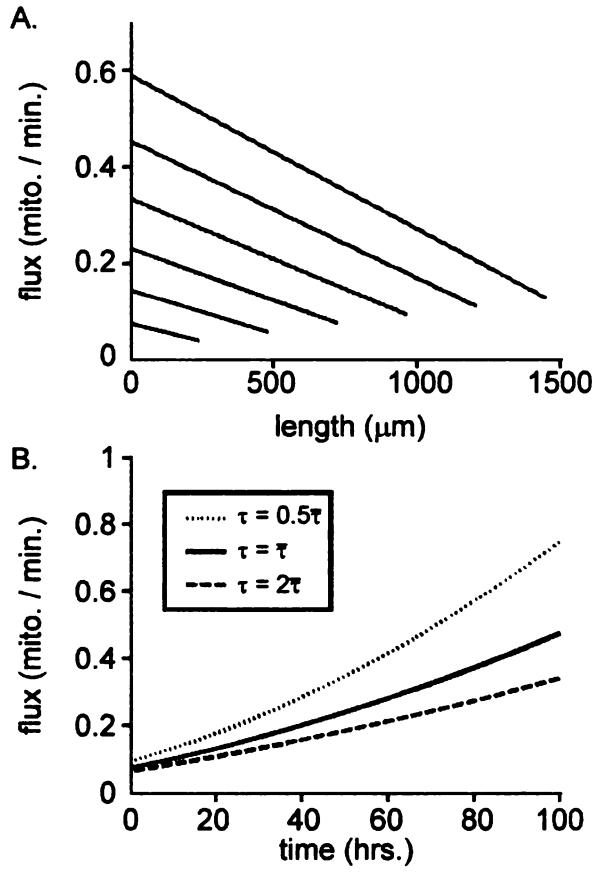

Figure 2.6: Flux Predictions Along the Length and at the Cell Body – (A) Flux of mitochondria is linearly decreasing with distance from the cell body. Shown are the flux profiles at times $t = 0$, 24, 48, 72, 96, and 120 hours. As the nerve elongates and increases its caliber, both production and flux along the length of the axons increase. $L_0 = 237\mu$m, $P_0 = 0.229$ mitochondria μm^{-1}, $\alpha = \bar{\alpha}$, $\gamma = \bar{\gamma}$, $\tau = \bar{\tau}$. (B) The flux of new mitochondria into the axon is plotted as a function of time. Production must increase quadratically in order to support the observed increases in length and density. Values used are the same as in (A) except for τ which is varied. Increasing τ diminishes the quadratic effect on the increase in production.

of these nerves may remain constant. During this phase of growth the parameter α will be zero, reducing the flux equation to being linear in t. Similarly, short neurons will reach their mature length quickly and continue to increase their diameter, also giving a linear influx profile (in t). When the axon has reached its mature length and diameter, then influx must be constant to keep the axon supplied with functioning mitochondria. Between synapse formation and the end of the neuron's life the axon will be in one of these states.

2.4 Discussion

In this study we explore several aspects of axonal elongation in *Drosophila* and derive a mathematical model which predicts the rate of mitochondrial addition to the axon. Length and diameter are shown to increase in a linear fashion in medial segmental *Drosophila* neurons, and a value for mitochondrial half-life is derived. A basis for our model is the mitochondrial life cycle hypothesis (Fig. 2.1). The model incorporates mitochondrial clearance from the axon and active transport, but excludes diffusion since mitochondria are either attached to microtubule motors or stably docked to the cytoskeleton [21, 44, 92]. Flux of mitochondria decreases linearly with distance from the cell body. Based on the constant rate of lengthening and diameter increase, and on mitochondrial degradation, influx of new mitochondria to the axon was found to necessarily increase in a quadratic fashion.

Analysis of mitochondria in 1^{st}, 2^{nd}, and 3^{rd} instar larvae revealed no significant concentration gradient along the nerve (Fig. 2.3). This suggests the neuron has an efficient mechanism for organization of mitochondria. Kymographs have revealed that mitochondria are able to dock in regions of low density [63], and docked mitochondria have been observed to undergo short bouts of transport and then re-dock; a sort of mitochondrial redistribution [13, 21]. The ability of mitochondria to reorganize is

crucial in maintaining a uniform density given the factors that lead to gradients in distribution. Namely, axons are viscoelastic structures which can be deformed either by growth cone induced stretching [50] or towed growth of pre-synaptic [25] or mature neurons [1, 74], and mitochondria eventually become depolarized and are transported back to the cell body [63].

The analysis did reveal, however, that mitochondrial density increases throughout larval development (Fig. 2.4B). When coupled with the lengthening of the nerve, the demand for mitochondria increases in a quadratic fashion (2.11). Using our estimates for α, γ, and τ, and extrapolated values for the initial length and density of the nerve (Fig. 2.4A, B), we found that the quadratic coefficient has a value of 8.17×10^{-4} mitochondria h^{-3} while the linear coefficient is 0.146 mitochondria h^{-2} when $x = 0$. The quadratic effect at the cell body is most noticeable when the flux profile is viewed over the course of days (Fig. 2.6A). Should either rate of increase (α or γ) go to zero, the flux would be increasing in a purely linear fashion. At steady-state length and density ($L = L_\infty$, $P = P_\infty$) the flux profile is constant over time. It is also possible that τ increases during development. This would lower the demand for new mitochondria and thus should be investigated.

While analysis of mitochondrial density revealed a uniform distribution along the length of the nerve (Fig. 2.3), the model suggests that the profile of moving mitochondria is linearly decreasing along the length (2.9). In order for this to be the case, the profile of docked mitochondria must necessarily be linearly increasing along the length. Since healthy mitochondria, either motile or stationary, are capable of producing ATP, this is consistent with a uniform demand for energy along the length of the axonal shaft, (excluding the region directly proximal to the synapse, where mitochondrial concentration has been observed to be higher) [20]. Mitochondria in the cell body may also contribute ATP to the most proximal region of the axon, which would further reduce the need for docking there. However, if the overall ratio

of docked mitochondria to transported mitochondria is high, then a gradient in docked mitochondria would not be observed.

There has been clear evidence that cell bodies are able to respond to changes in length by increasing cellular production. In one such case Pfister et al. showed that extreme towing of mature neurons resulted in longer healthy neurons of increased caliber [74, 73]. Here the change in length was mechanically driven and the cellular density increased as a result. If towing occurred too rapidly, however, the axons ruptured. Hence the cell body's ability to adapt to rapid changes in length is limited. The data in those studies give insight as to how quickly axons may be towed, but to our knowledge no theoretical analysis of the problem yet exists. For the purposes of neuronal repair it would be necessary to understand how an axon is viscoelastically deformed by axial tension (i.e. the increase in protein demand in response to towing) [72] and also to know the production limitations of the cell body.

Our model is broad in the sense that it studies the behavior of the mitochondrial population as a whole. The main idea is that the cell is working to achieve an optimal density which is uniform along the length but increases with time (Figs. 2.3, 2.4B). Tension on the cell from various sources can lead to local differences in density. How a uniform density is re-established is not specifically addressed. One possible explanation is that new mitochondria travel the entire distance from the cell body to sites of need. Another possibility is that, as new mitochondria are being produced, docked mitochondria are redistributed through fast axonal transport [12]. In terms of maintaining uniformity, redistribution through fast axonal transport would be able to achieve this in less time.

An interesting point is that the longer segmental nerves were not observed to be thinner than the shorter ones. This suggests that the level of mitochondrial biogenesis / protein synthesis in the neurons differs, and that two neurons of the same age are able to regulate protein synthesis based on their lengths. If protein synthesis were

independent of nerve length, then one would expect shorter nerves to have larger caliber. Little is known about whether neurons can sense how long they are, but this piece of evidence makes a strong case for some sort of signaling pathway for length recognition. While the length of the nerve is determined by the size of the animal, the caliber is controlled by the production of material, making this a vital regulatory process. Another example of selective diameter regulation is seen in the variance of cat retinal axons. Here, a correlation was found between the eccentricity of intraretinal X-cells and their axonal diameters, and also between soma size and axonal diameter [89]. The entire system, which has the difficult task of processing visual cues, was found to be highly complex, with intraretinal and extraretinal axon sizes varying to produce uniform mean total conduction times [88]. The regulation of action potentials is known to be dependent on axonal and dendritic diameters [42, 76], thus this may be the motivation for a carefully managed axonal diameter. Given these examples we propose that the neuron is able to detect its own length and mitochondrial density and, in turn, modulate production and reorganize cellular materials to achieve and maintain a preferred caliber.

Current therapies for treating nerve damage typically involve the application of drugs or growth factors, the splicing of severed nerve endings together such that the distal degenerating nerve provides a track for the regeneration of axons coming from the proximal stump, and / or the insertion of conduits to provide tracks [75]. Our model raises questions pertinent to the treatment of peripheral nerve injury. It suggests that the production of materials is a response to increased axonal length. Traditionally, reconnection of served nerves is performed without tension at the site of repair. However, studies in primates have shown that direct repair under modest tension yields better results relative to a tension-free repair, but this remains controversial [79]. Could force application at the stump of a severed nerve, that causes axonal lengthening, be used in combination with current therapies to facilitate regen-

eration?

Developing rational treatments for chronic neurodegenerative disorders, such as Alzheimer's and Parkinson's diseases, is hindered by the weak understanding of the chain of events linking the primary insult and the ultimate manifestation of the disease. A deeper knowledge of the mitochondrial life cycle (Fig. 2.1) will provide a foundation for the study of these maladies, not unlike the way Harvey's discovery of blood circulation [96] laid the groundwork for the treatment of heart disease. The predictions made by our model add to the overall understanding of mitochondrial dynamics, and further studies of mitochondria in the axon will be essential to the goal of curing neurodegenerative diseases.

While lengthening in post-synaptic neurons is governed by the rate of bodily growth, it is yet unclear how tension changes during this process. On the surface, stretching of the axons would seemingly increase tension. However, the addition of new material to the axons will counteract the stress that is caused by stretching. Further, it is unclear whether mass addition occurs in preparation for or in response to lengthening-induced tension. How these two processes interact, which we cannot elucidate from this study, is highly significant in understanding mitochondrial biogenesis and transport and demands further examination.

2.4.1 Model Comparisons

While production of cellular materials is shown to necessarily increase with time, the profile of flux at any fixed time is decreasing with distance from the cell body (Fig 2.6). The result is in qualitative agreement with studies that observed a decline in transported mitochondria in growing axons [62, 66]. This flux gradient is present in models of transport which consider protein degradation [60] and is absent in models which do not [33]. Smith and Simmons reported a steady flux in their unidirectional transport model and a linearly declining flux in their bidirectional transport model

[86]. Our flux results are in agreement with their bidirectional model when a maximal efficiency of cargo loading onto microtubules is assumed. The declining profile can be explained in that any new mitochondrion, regardless of destination, must be transported through the most proximal region of the axon but fewer and fewer are transported to increasingly distal regions. Mitochondria are believed to dock in regions where ATP levels are low [44, 63], which means that transported materials can leave the transported phase at any point along the axon. This differs from other models, where all transported materials must be delivered to the growth cone (a one sink model versus a multi-sink model). Hence different models should be used for transport of different intracellular cargos (e.g. mitochondria vs. synaptic vesicles).

A significant difference between our model and previous models [60, 62, 91] is that we consider axonal length to be independent and treat protein synthesis as a dependent variable. At the foundation of this choice is the debate over what drives axonal elongation. While some have presented arguments for production-driven elongation, it may be the other way around where production responds to changes in axonal length. We have concentrated here on mature neurons, yet the idea applies to presynaptic axons as well. Tension has been shown to cause lengthening in both types of neuron, and in those cases the cell bodies have responded by increasing production to restore the axon or nerve to a viable diameter [1, 25, 50, 74]. For these reasons we hold changes in length as independent and study how production must change to sustain the axon and avoid rupture. Put another way, production does not increase to cause changes in length, but to support them. It is likely that there is an upper bound on material production by the cell body, but such a bound is yet unknown.

Redistribution of cellular materials likely plays a large role in maintaining the observed uniform cellular density. Brown et al. derived a stochastic model to address stop-and-go transport of neurofilaments [14]. In this study, transition probabilities of neurofilaments changing between the various states of transport (paused or moving

at various velocities) were experimentally determined. To maintain a uniform concentration of cellular materials, stop-and-go transport would need to preferentially occur in regions with a local concentration gradient. A possible way to apply this stochastic model to one that favors a uniform mitochondrial distribution would be to use transition probabilities which are functions of $\partial P/\partial x$.

2.5 Conclusion

In this section we have developed a model for elongation that suggests that the flux of mitochondria in the axon decreases linearly along the length of the axon and increases quadratically with time. The model is based on the observations that axonal length and mitochondrial density tend to increase at a linear rate during development. Using an analysis of retrograde flux of mitochondria we derived an updated estimate for mitochondrial half-life in *Drosophila*. Our model suggests that mitochondrial production is modulated by the cell body based on axonal length, axonal diameter, and mitochondrial half-life. If neurons are able to detect their lengths, as we suggest, then uncovering the means by which they do this opens many exciting avenues for future work. To test these predictions we plan to measure anterograde and retrograde mitochondrial flux during each of the three instars of development. In this process we may also assess whether mitochondrial half-life is constant through development or whether it varies, and also test the expected linear decrease in flux along the length of the nerve.

Chapter 3

The Role of Stretching in Slow Axonal Transport

3.1 Introduction

Slow axonal transport and axonal elongation occur at approximately the same velocity and many have suspected that these two processes are closely related. Intuitively, axonal elongation cannot occur at a rate that exceeds the transport of the materials that make up the axon. While some axonal proteins are moved by fast transport at average velocities of up to 400 mm day^{-1}, many cytoskeletal proteins are transported in slow components a and b at velocities in a range of 0.1 to 10 mm day^{-1} [5, 61, 80, 95, 13, 40]. A series of recent papers have demonstrated that axonal stretching is linked to axonal elongation [74, 1, 87, 52, 82]. A particularly exciting result is that when forces are applied to axons they can elongate at a rate of 8 mm day^{-1} for sustained periods of time without thinning [74, 73]. Together these results would imply that slow axonal transport is increased during rapid stretch-induced growth.

The demand for slow axonal transport and the location of mass addition to the axon depend on the mode of elongation (Fig. 3.1) which, in turn, depends on the

physical properties of the system. In this paper we analyze the role of stretching in the slow transport of intracellular materials. We do this in the contexts of growth cone mediated axonal elongation, towed growth after synapse formation, and conditions of extreme stretch growth. Building upon our previous work, we develop a model that determines how much of the necessary flux of materials can be accounted for by stretching. Finally we suggest how stretching may be incorporated into models of slow axonal transport.

3.2 Results

3.2.1 Flux Equations

The flux profile $J(x,t)$ that is necessary to support a constant velocity of axonal elongation was determined in the previous chapter as Eq. 2.9:

$$J(x,t) = -\left[\frac{P(t)}{\tau} + \alpha\right] x + \frac{P(t)\,L(t)}{\tau} + \gamma P(t) + \alpha L(t)\,. \tag{3.1}$$

where P is the density of materials in the axon, L is the length of the axon, α is the rate of change of the density of materials, γ is the rate of lengthening, and τ is the characteristic time constant of decay (defined by *half-life* $= \tau \times \ln 2$) [71]. Based on work in the preceding chapter, we assume that the density is uniform with respect to distance along the axon. Length and density increases in elongating axons have also shown a linear trend, which give equations $L(t) = L_0 + \gamma t$ and $P(t) = P_0 + \alpha t$.

The viscoelastic response of an axon to pulling forces is dependent on the axon's axial viscosity and the level of adhesions that exist between the axon and a possible substrate [72]. We consider two cases: one where there are no adhesions and one where there are adhesions uniformly distributed along the length of the axon. In the case where the axon is unattached, the velocity of materials will decrease linearly

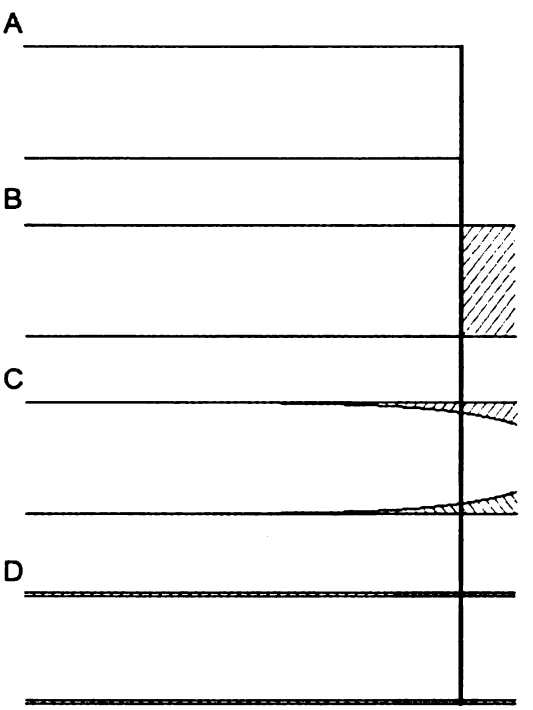

Figure 3.1: Opposing Models of Mass Addition – As an axon elongates, new mass is added to the existing framework. (A) Diagram of an axon before a bout of elongation. Vertical line across all panels denotes the position of the distal tip before the bout. (B) Diagram of an axon after elongation by the tip-growth model. The shaded area denotes the location of the addition of new mass. (C) Diagram of an axon after elongation by stretch-and-intercalation in the presence of adhesions. Unshaded area distal to the vertical line exhibits the portion of the existing framework which has been pulled into the "new" segment of the axon by stretching. (D) Diagram of an axon after stretching in the absence of adhesions. New mass is added uniformly along the axon.

from the source of tension (Fig. 3.2) so that the flux $J_{\mathrm{U}}(x,t)$ in this regime may be approximated by

$$J_{\mathrm{U}}(x,t) = \gamma \frac{x}{L(t)} P(t). \tag{3.2}$$

If adhesions are present, then the decrease in velocity of materials is non-linear in x and is dependent on the viscosity of the axon G and the strength of the adhesions η. In this case the flux of materials can be approximated by

$$J_{\mathrm{Ad}}(x,t) = \frac{F_0}{\sqrt{\eta G}} \frac{\sinh\left(x\sqrt{\eta G}\right)}{\cosh\left(L(t)\sqrt{\eta/G}\right)} P(t) \tag{3.3}$$

where F_0 is the magnitude of the generated axial force (Fig. 3.3). Here we will assume that the axon is long enough so that the flux at the growth cone $J_{\mathrm{Ad}}(x,t) \approx \left[F_0/\sqrt{\eta G}\right] P(t)$ where the velocity of elongation $F_0/\sqrt{\eta G}$ is constant. We thus equate this value to γ. Specifics of this assumption will be handled below.

Figure 3.2: Flux Profiles in the Absence of Adhesions – Transport profiles are shown at three different time points during elongation. Dimensionless values characterizing axonal elongation $A = 1.98$ and change in protein density $C = 1.00$ were calculated from parameters given in Table 3.1. With an initial length of $L_0 = 237\mu$m and an elongation rate of $\gamma = 9.24\ \mu\text{m h}^{-1}$, profiles are shown (A) after zero days, (B) after one day, and (C) after five days. The solid lines denote the total necessary flux profile (Eq. 2.9) as determined in [71]. The point where the Stretch Transport (Eq. 3.2) and Other Transport lines intersect is $x_{1/2}/L$. Because proteins are degraded along the length and protein density simultaneously increases, the requirement of other modes of transport increases over time. Thus, the fraction of transport due to stretching decreases, as seen by the rightward shift in the point where the modes of transport intersect $x_{1/2}/L$.

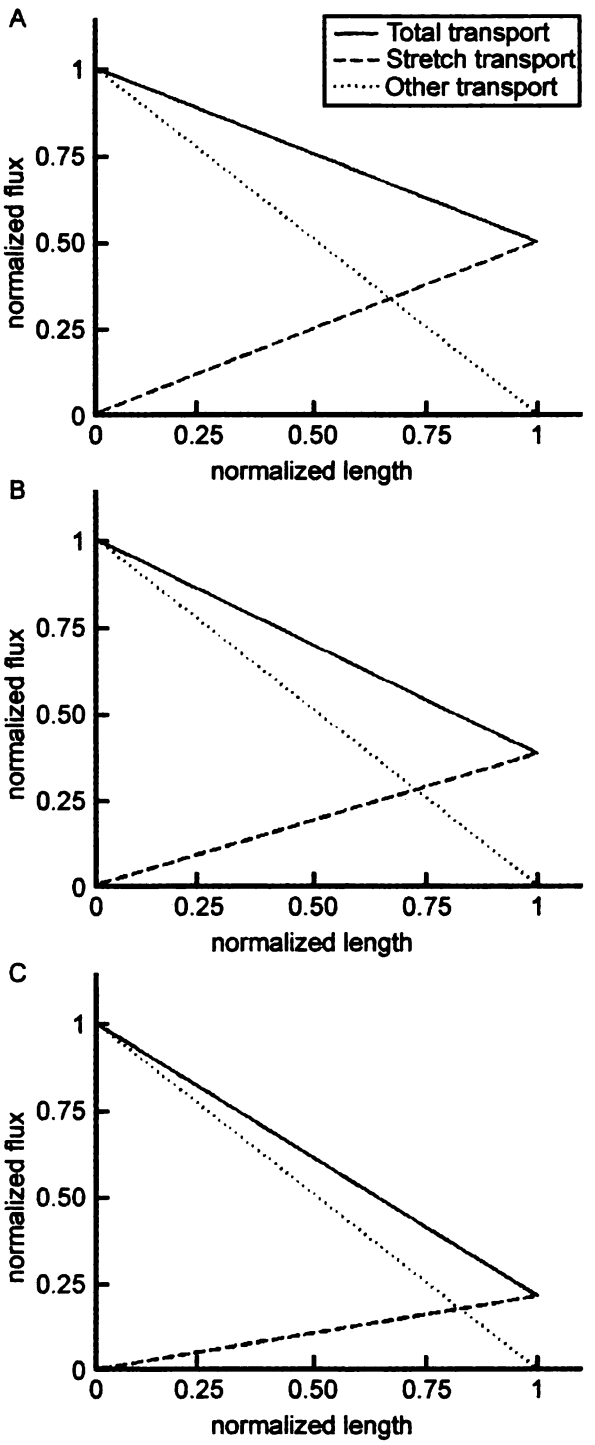
A
Total transport
Stretch transport
Other transport
normalized flux
normalized length
B
normalized flux
normalized length
C
normalized flux
normalized length
0
0.25
0.50
0.75
1

Figure 3.2:

Figure 3.3: Flux Profiles in the Presence of Adhesions – Transport profiles are shown at three different time points in an elongation process. Dimensionless values characterizing elongation $A = 1.98$, axonal viscoelastic properties $B = 7.06$, and changes in protein density $C = 1.00$ were calculated from parameters given in Table 3.1. With an initial length of $L_0 = 237\mu$m and an elongation rate of $\gamma = 9.24\mu$m h^{-1}, profiles are shown (A) after zero days, (B) after one day, and (C) after five days. The solid lines denote the total necessary flux profile (Eq. 5) as determined in [71]. The point where the Stretch Transport (Eq. 7) and Other Transport lines intersect is $x_{1/2}/L$. The presence of adhesions along the length decreases the effect of stretching. Thus the position where the modes of transport intersect $x_{1/2}/L$ is close to the normalized length of 1.

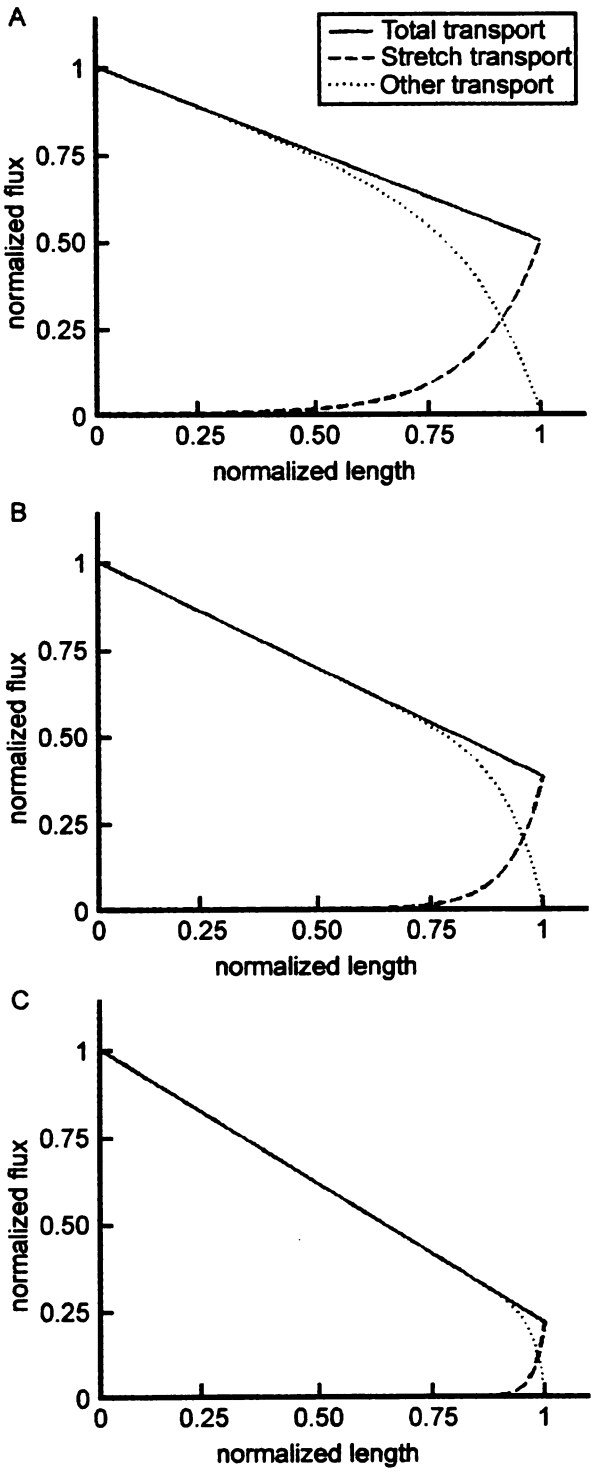
A
Total transport
Stretch transport
Other transport
normalized flux
normalized length
B
normalized flux
normalized length
C
normalized flux
normalized length
0
0.25
0.50
0.75
1

Figure 3.3:

3.2.2 Non-Dimensionalization

As the magnitudes of variables and parameters will vary based on the system to be studied, it is necessary to redefine them in dimensionless form. We start with the following choices for the variables:

$$\begin{aligned} \tilde{x} &= \frac{x}{L_0} & \tilde{t} &= \frac{\gamma}{L_0} t & \tilde{P} &= \frac{P}{P_0} \\ \tilde{L} &= \frac{L}{L_0} & \tilde{J} &= \frac{\tau}{P_0 L_0} J \end{aligned} \tag{3.4}$$

L_0 and P_0 represent the initial values of the axon length and protein density, respectively. As we will study the case of minimal protein decay (τ large) we avoid using $\tilde{t} = t/\tau$. The non-dimensional flux equations may then be written as

$$\tilde{J}\left(\tilde{x}, \tilde{t}\right) = -\left[\tilde{P} + C\right] \tilde{x} + \tilde{P}\tilde{L} + A\tilde{P} + C\tilde{L}, \tag{3.5}$$

$$\tilde{J}_{\mathrm{U}}\left(\tilde{x}, \tilde{t}\right) = A\frac{\tilde{x}}{\tilde{L}}\tilde{P}, \tag{3.6}$$

and

$$\tilde{J}_{\mathrm{Ad}}\left(\tilde{x}, \tilde{t}\right) = AD\frac{\sinh\left(B\tilde{x}\right)}{\cosh\left(B\tilde{L}\right)}\tilde{P}, \tag{3.7}$$

where the four dimensionless parameters A, B, C and D are defined as

$$\begin{aligned} A &= \frac{\gamma t}{L_0} & B &= L_0\sqrt{\eta/G} \\ C &= \frac{\alpha\tau}{P_0} & D &= \frac{F_0}{\gamma\sqrt{\eta G}}. \end{aligned} \tag{3.8}$$

Expressions for the scaled length and density are $\tilde{L}\left(\tilde{t}\right) = 1+\tilde{t}$ and $\tilde{P}\left(\tilde{t}\right) = 1+(C/A)\,\tilde{t}$, respectively. Our assumption that the velocity of stretch elongation is constant will be safe if $\tanh\left(B\tilde{L}\right)$ which requires that $B\tilde{L} > 2.7$. If this is the case then γ can be equated with the velocity of stretch-elongation and we may set $D = 1$. At this point

we drop the tildes while keeping in mind that we are dealing with the dimensionless variables.

3.2.2.1 Alternate Scaling Choices

Our choice of scaling above leaves something to be desired if one wishes to study the effect the time-constant τ has on the system. This is because both parameters A and C contain τ. The parameters α and γ, however, are present in only one of those two parameters. If we are interested in studying the effects of τ we can change the scaling factor on the flux variable:

$$\tilde{x} = \frac{x}{L_0} \qquad \tilde{t} = \frac{\gamma}{L_0} t \qquad \tilde{P} = \frac{P}{P_0}$$
$$\tilde{L} = \frac{L}{L_0} \qquad \tilde{J} = \frac{1}{\alpha L_0} J \tag{3.9}$$

This gives scaled flux equations (dropping the tildes)

$$J(x,t) = -[HP+1]x + HPL + EP + L \tag{3.10}$$

$$J_{\mathrm{U}}(x,t) = E\frac{x}{L}P \tag{3.11}$$

$$J_{\mathrm{Ad}}(x,t) = DE\frac{\sinh(Bx)}{\cosh(BL)}P \tag{3.12}$$

where the new dimensionless parameters are defined by

$$E = \frac{\gamma P_0}{\alpha L_0} \qquad H = \frac{P_0}{\alpha \tau}. \tag{3.13}$$

The advantage of this choice is that the variables τ and γ are isolated in separate parameters. The downside is that the rate of protein increase α is present in both parameters (regardless of our choice of scaling, we cannot avoid one of α, γ, or τ

existing in both dimensionless parameters). Further, E and H vary inversely with α and τ, which could cause some problems if either of these are small. While the case of τ very small (very short protein half-life) is not generally relevant, a value of α equal to zero represents a constant protein density, which is a fairly common situation.

Another choice is to let $\tilde{J} = J/(\gamma P_0)$. This lead to a set of flux equations

$$J(x,t) = -[UP + V]x + UPL + P + VL \tag{3.14}$$

$$J_{\mathrm{U}}(x,t) = \frac{x}{L}P \tag{3.15}$$

$$J_{\mathrm{Ad}}(x,t) = D\frac{\sinh(Bx)}{\cosh(BL)}P \tag{3.16}$$

where

$$U = \frac{L_0}{\gamma\tau} \qquad V = \frac{\alpha L_0}{\gamma P_0}. \tag{3.17}$$

This choice of scaling parameters isolates α and τ. It also simplifies the stretch-flux equations by eliminating a parameter from each (at the expense of the total flux equation being slightly more complex). Again, however, the parameters are inversely proportional to γ and τ, which may be undesirable. Depending on the situation, one of these alternate scaling choices may be preferable. Because of the inverse relationships that exist in the alternate scaling choices, our original choice for scaling seems to be the least difficult to interpret.

3.2.3 Region of Stretch-Dominance and Anterograde Momentum

The total flux profile is decreasing and the stretch-flux profiles are increasing so that for each value of t there will be a unique point $x_{1/2}(t)$ where the stretch-induced flux will equal half of the total flux. Between that point and the terminal end of the

axon, stretching will account for more than half of anterograde flux of material (Figs. 3.2, 3.3).

In the case of no adhesions, we solve the equation $J_U(x,t) = J(x,t)/2$ for x and divide by L to obtain

$$\frac{x_{1/2}}{L} = \frac{PL + AP + CL}{PL + 2AP + CL}, \tag{3.18}$$

which is easily seen to be between zero and one. The evolution of this point of equality is shown in Fig. 3.4A for the cases of measured axonal conditions ($A, C = O(1)$), the case of constant protein density ($C = 0$), the case of undetectable protein degradation ($A, C >> 1$), and the case of both constant protein density and undetectable protein degradation ($C = 0$ and $A >> 1$). In general, increasing C pushes $x_{1/2}/L$ toward 1 whereas increasing A pushes $x_{1/2}/L$ toward 1/2.

Another measure of the effect of stretching is how much it contributes to the total anterograde momentum of the system. Momentum, $p(t)$, is calculated as the integral of flux over the length of the axon and is a measure of total transport in the axon.

$$p(t) = \int_0^{L(t)} J(x,t)\, dx = \frac{L}{2}(PL + 2AP + CL). \tag{3.19}$$

Figure 3.4: The Contribution of Stretching Changes During Elongation – As an axon elongates, the fraction of the axon where stretching is the dominant form of transport decreases. (A) The lines show $x_{1/2}/L$ as a function of increasing axonal length. In the absence of adhesions, a constant axonal diameter, and extremely high protein half-life ($A >> 1$, $C = 0$), the only source of protein demand is axonal elongation. Thus $x_{1/2}/L$ remains fixed at 0.5. When the effect of increasing protein density ($A, C >> 1$) is added, $x_{1/2}/L$ increases slowly to a limiting value of 2/3. Under conditions of constant axonal diameter and a physiological protein half-life ($C = 0$) the contribution due to stretching decreases as the axon elongates. When caliber increases and proteins degrade ($A = 1.98$ and $C = 1.00$) this effect is elevated. (B) Comparison of the evolution of $x_{1/2}/L$ in the presence of (solid line) and absence of (dotted-dashed line) adhesions. $A = 1.98$, $C = 1.00$ in both cases and $B = 7.06$ when adhesions are present. (C) In the presence of adhesions ($B = 7.06$), $x_{1/2}/L$ is lowered only slightly for extreme values of A, C.

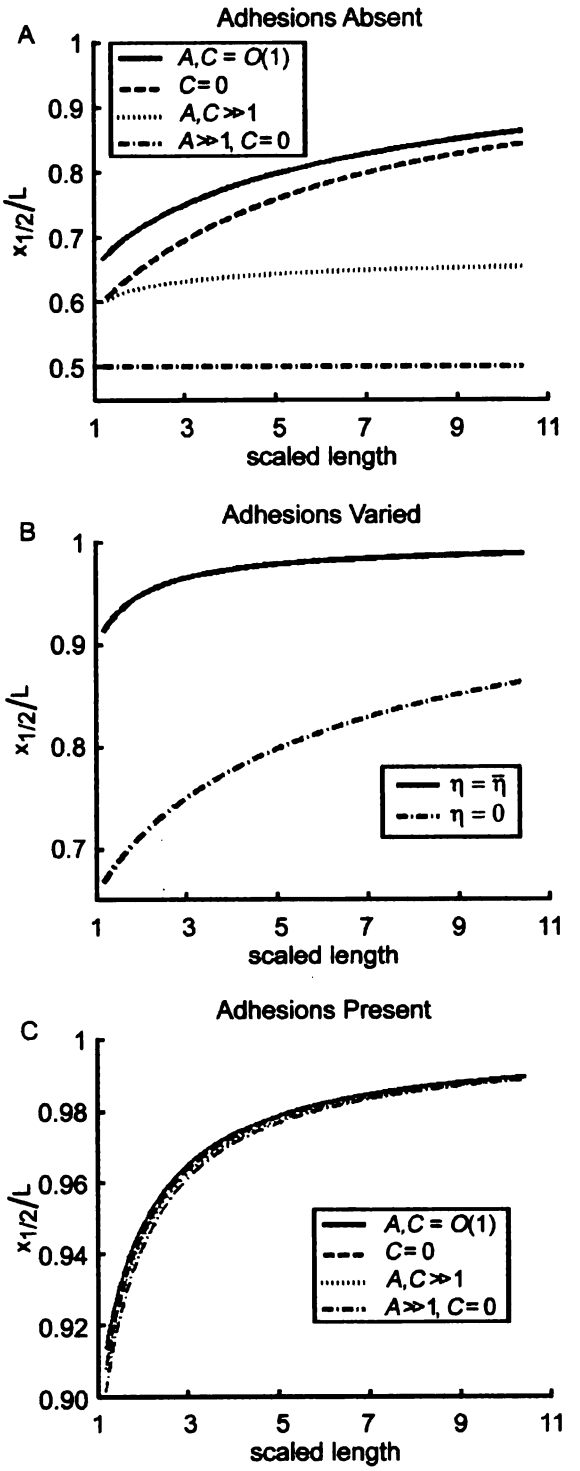
A
Adhesions Absent
A,C = O(1)
C = 0
A,C ≫ 1
A ≫ 1, C = 0
x1/2/L
scaled length
B
Adhesions Varied
η = η̄
η = 0
x1/2/L
scaled length
C
Adhesions Present
A,C = O(1)
C = 0
A,C ≫ 1
A ≫ 1, C = 0
x1/2/L
scaled length

Figure 3.4:

The momentum due to stretching is calculated similarly (here in the absence of adhesions):

$$p_{\mathrm{U}}(t) = \int_0^{L(t)} J_{\mathrm{U}}(x,t)\, dx = \frac{1}{2}APL. \tag{3.20}$$

The fraction of anterograde momentum that is accounted for by stretching is $p_{\mathrm{U}}(t)/p(t)$. Note that both of these may be calculated using simple geometric formulae. In the case of no adhesions, the contribution of stretching to total anterograde momentum and the point where stretching accounts for half of total flux are related by

$$\frac{p_{\mathrm{U}}(t)}{p(t)} = \frac{AP}{PL + 2AP + CL} = 1 - \frac{x_{1/2}}{L}. \tag{3.21}$$

When adhesions are present along the length of the axon, we find $x_{1/2}/L$ by solving the equation $J_{\mathrm{Ad}}(x,t) = J(x,t)/2$, which is transcendental. Multiplying this equation by two and setting $D = 1$ gives

$$2A\frac{\sinh(Bx)}{\cosh(BL)}P = -[P + C]x + PL + AP + CL. \tag{3.22}$$

For the case of constant protein density and undetectable protein degradation ($C = 0$ and $A >> 1$) the asymptotic solution is

$$\frac{x_{1/2}}{L} = \frac{\operatorname{asinh}\left[\frac{\cosh(BL)}{2}\right]}{BL} + O\left(A^{-1}\right) \tag{3.23}$$

and the first term is a good approximation.

An asymptotic solution up to $O\left(\epsilon^2\right)$ can be found in a straight-forward manner. Let $C = 0$ and $\epsilon = \frac{1}{A}$. Then Equation 3.22 becomes

$$2\frac{\sinh(Bx)}{\cosh(BL)} = -\epsilon x + \epsilon L + 1 \tag{3.24}$$

If we let $x = x_0 + \epsilon x_1 + \epsilon^2 x_2 + \ldots$ then

$$\frac{2}{\cosh(BL)} \sinh\left(Bx_0 + \epsilon B x_1 + O\left(\epsilon^2\right)\right) = \\ -\epsilon\left(x_0 + \epsilon x_1 + \epsilon^2 x_2 + O\left(\epsilon^3\right)\right) + \epsilon L + 1 \quad (3.25)$$

Separating this equation into its ϵ^0, ϵ^1, ϵ^2,... components depends on accurately expanding the sinh term. We apply the Taylor expansion:

$$f(x+\epsilon) = f(x) + \epsilon f'(x) + \frac{\epsilon^2}{2} f''(x) + O\left(\epsilon^3\right)$$

to get

$$\sinh\left(Bx_0 + \epsilon\left(Bx_1 + \epsilon B x_2 + O\left(\epsilon^2\right)\right)\right) = \\ \sinh(Bx_0) + \epsilon\left(Bx_1 + \epsilon B x_2 + O\left(\epsilon^2\right)\right)\cosh(Bx_0) \\ + \frac{\epsilon^2\left(Bx_1 + \epsilon B x_2 + O\left(\epsilon^2\right)\right)^2}{2}\sinh(Bx_0) + O\left(\epsilon^3\right) \quad (3.26)$$

Now that we have the expansion (3.26) we solve Eq. (3.25) for the first three orders.

The $O(1)$ terms give the equation $\sinh(Bx_0) = \frac{\cosh(BL)}{2}$ so that

$$x_0 = \frac{1}{B}\operatorname{asinh}\left(\frac{\cosh(BL)}{2}\right) \quad (3.27)$$

The ϵ^1 terms yield the equation $\frac{2}{\cosh(BL)} B\cosh(Bx_0)\, x_1 = -x_0 + L$ which easily solves for x_1:

$$x_1 = \frac{\cosh(BL)}{2B\cosh(Bx_0)}(-x_0 + L) \quad (3.28)$$

Using the relationship $\cosh(\operatorname{asinh} x) = \sqrt{x^2+1}$ we can write the solution for x_1 as

$$\begin{aligned} x_1 &= \frac{\cosh(BL)\left(L - \frac{1}{B}\operatorname{asinh}\left(\frac{\cosh(BL)}{2}\right)\right)}{2B\sqrt{\left(\frac{\cosh(BL)}{2}\right)^2 + 1}} \\ &= \frac{\cosh(BL)\left(BL - \operatorname{asinh}\left(\frac{\cosh(BL)}{2}\right)\right)}{B^2\sqrt{\cosh^2(BL) + 4}} \end{aligned} \tag{3.29}$$

Equating ϵ^2 terms on each side of Eq. (3.25) gives

$$Bx_2\cosh(Bx_0) + \frac{(Bx_1)^2}{2}\sinh(Bx_0) = -x_1 \tag{3.30}$$

which can be solved:

$$x_2 = \frac{-2x_1 - (Bx_1)^2\sinh(Bx_0)}{2B\cosh(Bx_0)}. \tag{3.31}$$

A reasonably clean expression for x_2 can be written without x_0 (but still containing x_1) by making the proper substitution:

$$x_2 = \frac{-4x_1 - (Bx_1)^2\cosh(BL)}{2B\sqrt{\cosh^2(BL) + 4}} \tag{3.32}$$

We thus have the asymptotic solution to Eq. (3.24) up to order ϵ^2.

$$\begin{aligned} x = & \frac{1}{B}\operatorname{asinh}\left(\frac{\cosh(BL)}{2}\right) \\ & + \epsilon \frac{\cosh(BL)\left(BL - \operatorname{asinh}\left(\frac{\cosh(BL)}{2}\right)\right)}{B^2\sqrt{\cosh^2(BL)+4}} \\ & + \epsilon^2 \frac{-4x_1 - (Bx_1)^2\cosh(BL)}{2B\sqrt{\cosh^2(BL)+4}} \\ & + O\left(\epsilon^3\right) \end{aligned} \tag{3.33}$$

In the general case the solution may be well-approximated using Newton's Method. Fig. 3.4B compares the evolution of $x_{1/2}/L$ in the presence (solid line) and absence (dotted-dashed line) of adhesions. Figure 3.4C shows that, in the presence of adhesions, the region of stretch-dominance is much less sensitive to the parameters A and C.

Figure 3.5 shows the dependence of $x_{1/2}/L$ on the parameters and $A, B,$ and $, C$ when $t = 0$. The dotted line in each panel represents the value of $x_{1/2}/L$ for $A = 1.98, B = 7.06,$ and $C = 1.00$, which are derived using data from previous experiments (see Table 3.1). In each panel, one parameter is allowed to vary while the other two are held fixed at the values listed above. Values for B are restricted to those greater than 2.7, as is required for the use of this model. The sensitivity of $x_{1/2}/L$ with respect to each parameter is estimated as the derivative of each of these

curves at $(\bar{A}, \bar{B}, \bar{C}) = (1.98, 7.06, 1.00)$. Those estimates are

$$\left.\frac{\partial}{\partial A}\left(\frac{x_{1/2}}{L}\right)\right|_{(\bar{A},\bar{B},\bar{C})} = -5.01 \times 10^{-3} \tag{3.34a}$$

$$\left.\frac{\partial}{\partial B}\left(\frac{x_{1/2}}{L}\right)\right|_{(\bar{A},\bar{B},\bar{C})} = 1.12 \times 10^{-2} \tag{3.34b}$$

$$\left.\frac{\partial}{\partial C}\left(\frac{x_{1/2}}{L}\right)\right|_{(\bar{A},\bar{B},\bar{C})} = 4.97 \times 10^{-3} \tag{3.34c}$$

which shows that $x_{1/2}/L$ is about twice as sensitive to B than to the other two parameters at this set of parameter values. Observing Figure 3.5 we see that the greatest reduction in $x_{1/2}/L$ can be achieved by decreasing B.

Figure 3.5: Sensitivity of the Stretch-Dominated Region in the Presence of Adhesions – The location of $x_{1/2}/L$ is plotted for varying values of the dimensionless parameters when $t = 0$. Dotted line in each panel represents the value of $x_{1/2}/L = 0.913$ for parameter values $A = 1.98$, $B = 7.06$, and $C = 1.00$. In the presence of adhesions, varying A or C does little to decrease $x_{1/2}/L$ (panels A and C). Smaller values of B, however, significantly decrease $x_{1/2}/L$ (panel B).

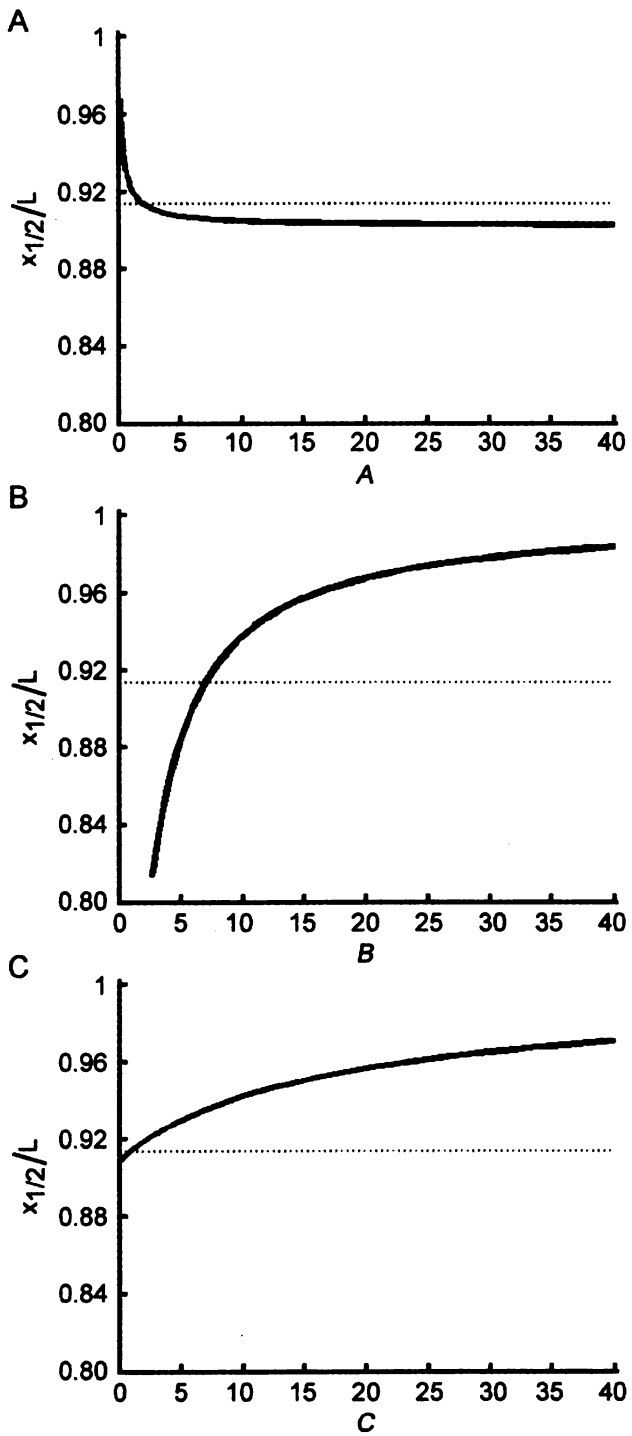
A
1
0.96
0.92
0.88
0.84
0.80
x1/2/L
0 5 10 15 20 25 30 35 40
A
B
1
0.96
0.92
0.88
0.84
0.80
x1/2/L
0 5 10 15 20 25 30 35 40
B
C
1
0.96
0.92
0.88
0.84
0.80
x1/2/L
0 5 10 15 20 25 30 35 40
C

Figure 3.5:

Parameter	Value	System
α	4.49×10^{-3} mito μm^{-1} h^{-1}	*Drosophila* Larvae
γ	9.24 μm h^{-1}	*Drosophila* Larvae
τ	50.8 h	*Drosophila* Larvae
L_0	237 μm	*Drosophila* Larvae
P_0	.229 mito μm^{-1}	*Drosophila* Larvae
G	3.9×10^7 g μm h^{-1}	Embryonic Chick
η	3.5×10^4 g μm^{-1} h^{-1}	Embryonic Chick

Table 3.1: Parameters used to calculate our baseline values of the non-dimensional parameters $A = 1.98$, $B = 7.06$, and $C = 1.00$.

Anterograde momentum is calculated in the same way as above:

$$p_{\mathrm{Ad}}(t) = \int_0^{L(t)} J_{\mathrm{Ad}}(x,t)\, dx = AP\frac{1-\operatorname{sech}(BL)}{B}. \tag{3.35}$$

The fraction of anterograde momentum that is accounted for by stretching in the presence of adhesions is $p_{\mathrm{Ad}}(t)/p(t)$ and can be expressed as

$$\frac{p_{\mathrm{Ad}}(t)}{p(t)} = \frac{2AP}{PL+2AP+CL}\frac{1-\operatorname{sech}(BL)}{BL}. \tag{3.36}$$

Figure 3.7 shows the sensitivity of this ratio to the parameters A, B, and C when $t = 0$. As with the region of stretch dominance, the greatest increase in stretching's contribution to anterograde momentum can be achieved by decreasing B. Unlike $x_{1/2}/L$, however, the contribution of stretching to anterograde momentum is about

equally sensitive to each parameter at $(\bar{A}, \bar{B}, \bar{C}) = (1.98, 7.06, 1.00)$:

$$\frac{\partial}{\partial A}\left(\frac{p_{\mathrm{Ad}}}{p}\right)\Big|_{(\bar{A},\bar{B},\bar{C})} = 1.59 \times 10^{-2} \tag{3.37a}$$

$$\frac{\partial}{\partial B}\left(\frac{p_{\mathrm{Ad}}}{p}\right)\Big|_{(\bar{A},\bar{B},\bar{C})} = -1.31 \times 10^{-2} \tag{3.37b}$$

$$\frac{\partial}{\partial C}\left(\frac{p_{\mathrm{Ad}}}{p}\right)\Big|_{(\bar{A},\bar{B},\bar{C})} = -1.58 \times 10^{-2} \tag{3.37c}$$

These partial derivatives may be found directly from Eq. 3.36. Note that this equation has a local maximum with respect to B, but this is an artifact since it occurs in the region $0 < B < 2.7$ for all $t \geq 0$.

Claim 1. *With respect to the parameter B, Eq. 3.36 possesses a unique local maximum on the interval $0 < B < 2.7$.*

Proof. We begin by rewriting Eq. 3.36:

$$\frac{p_{\mathrm{Ad}}(t)}{p(t)} = \psi(A, C)\,\frac{1 - \operatorname{sech}(BL)}{BL} \tag{3.38}$$

where

$$\psi(A, C) = \frac{2AP}{PL + 2AP + CL} \tag{3.39}$$

so that

$$\frac{\partial}{\partial B}\left(\frac{p_{\mathrm{Ad}}(t)}{p(t)}\right) = \psi(A, C)\,\frac{(BL)\operatorname{sech}(BL)\tanh(BL) - [1 - \operatorname{sech}(BL)]}{B^2 L}. \tag{3.40}$$

Now, since ψ is defined and non-zero for all $t \geq 0$, we have that this partial derivative is zero if and only if

$$BL\sinh(BL) - \cosh^2(BL) + \cosh(BL) = 0. \tag{3.41}$$

The plot of the LHS of Eq. 3.41 (Figure 3.6) shows that there is one positive zero (which we call z) and that this will be a relative maximum of Eq. 3.36 with respect to B. A numerical estimate for this zero is $z \approx 1.506$. When $t = 0$ we have that $L = 1$

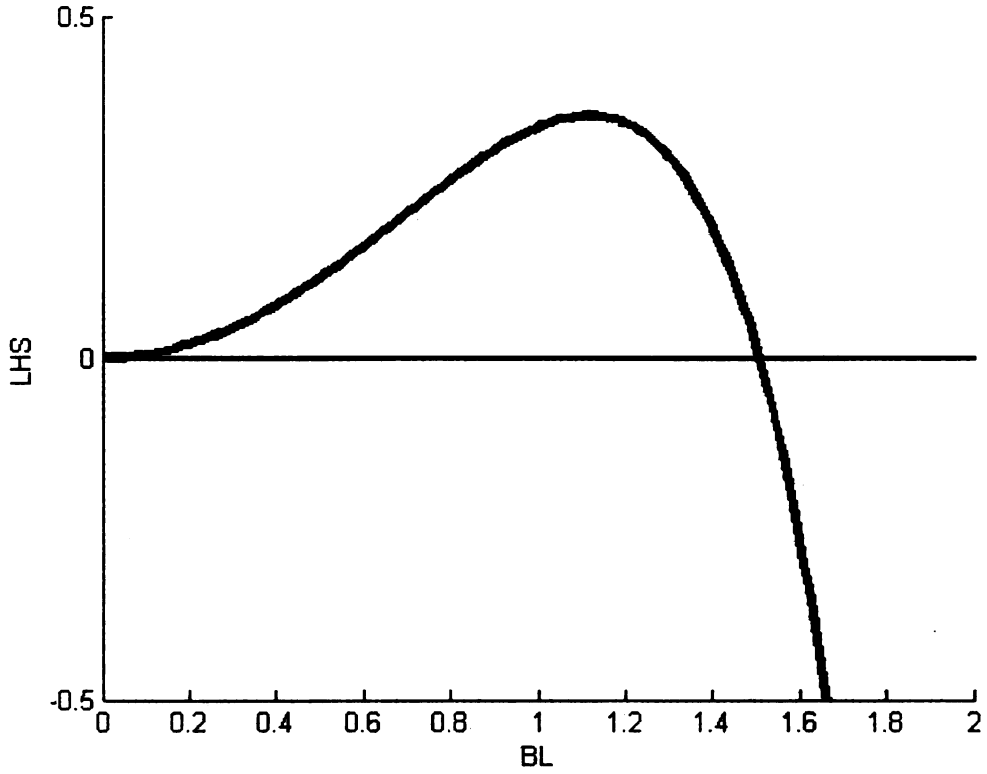

Figure 3.6: Graph of the left-hand side of Equation 3.41.

so that the solution of Eq. 3.41 (i.e. the maximum of Eq. 3.36) occurs at $B = z$. Since L increases with t, it follows that the value of B which maximizes $p_{\mathrm{Ad}}(t)/p(t)$ decreases. That is,

$$B_{max}(t) = \frac{z}{L} = \frac{z}{1+t} < z < 2.7. \tag{3.42}$$

□

Figure 3.7: Sensitivity of the Relative Contribution of Stretching to Momentum in the Presence of Adhesions – The value of the contribution of transport due to stretching, $p_{\mathrm{Ad}}(t)/p(t)$, is plotted for varying values of the dimensionless parameters when $t = 0$. Dotted line in each panel represents the value $p_{\mathrm{Ad}}(t)/p(t) = .094$ for parameter values $A = 1.98$, $B = 7.06$, and $C = 1.00$. In the presence of adhesions, increasing A can cause a moderate increase in $p_{\mathrm{Ad}}(t)/p(t)$, but decreasing C does little (panels A and C). As is the case with $x_{1/2}/L$, decreasing B leads to the greatest increase in $p_{\mathrm{Ad}}(t)/p(t)$ (panel B).

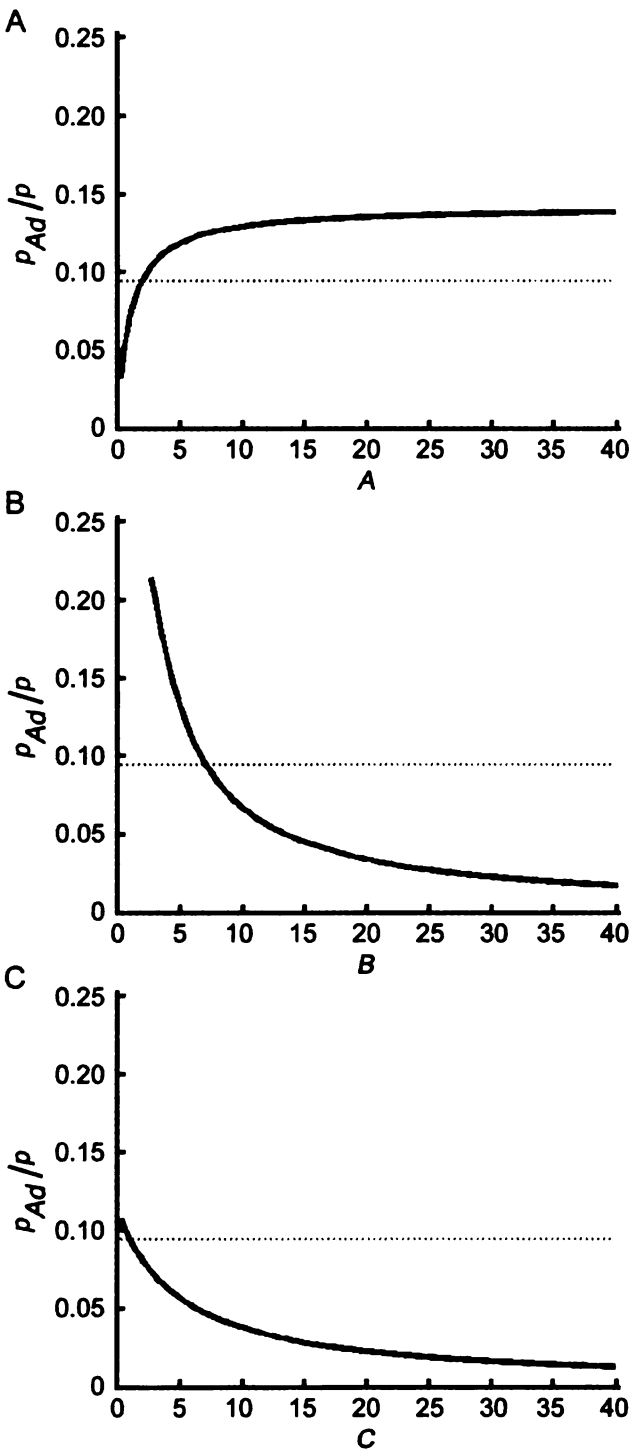
A
0.25
0.20
0.15
0.10
0.05
0
p_{Ad}/p
0 5 10 15 20 25 30 35 40
A
B
0.25
0.20
0.15
0.10
0.05
0
p_{Ad}/p
0 5 10 15 20 25 30 35 40
B
C
0.25
0.20
0.15
0.10
0.05
0
p_{Ad}/p
0 5 10 15 20 25 30 35 40
C

Figure 3.7:

3.3 Discussion

This work is the first to incorporate the effects of axonal stretching in a model of slow axonal transport. Here we consider both the case where stretching is caused by forces generated at the distal end of the axon [74, 72, 25], and by bodily growth. A fundamental issue that we address is under what conditions stretching makes a significant contribution to slow axonal transport. When studying the growth cone / synaptic region, shorter neurons, or when considering towed growth with limited adhesions, stretching makes a significant contribution to the transport process and lessens the demand for carrier-mediated transport to supply the distal axon with materials.

We have chosen two means by which to consider the effects of stretching. The first is to compare stretching's contribution to the flux of materials at different points along the axon. When this contribution is greater than half of total flux, we say that stretching is the dominant form of transport at that point. As the total flux profile is decreasing and the stretch-flux profile is increasing, there will be a unique point along the axon, $x_{1/2}(t)$, where stretching will account for half of anterograde flux. Between this point and the distal end, stretching is the dominant form of transport. The fraction of the axon where stretching is the dominant form of transport, then, is $1 - x_{1/2}/L$. The second way in which we view stretching's contribution to transport is anterograde momentum, which is the integral of anterograde flux over the length of the axon. Whereas flux is a measure of transport at a single point, anterograde momentum is a measure of total anterograde transport in the axon. The fraction of total anterograde transport that occurs by stretching is given by the ratio $p_{\mathrm{U}}(t)$ when adhesions are absent and $p_{\mathrm{Ad}}(t)$ when adhesions are present.

This model introduces three main parameters which play a role in the contribution of axonal stretching. These are the elongation parameter $A = \gamma\tau/L_0$, the density

parameter $C = \alpha\tau/P_0$, and the viscosity-adhesion parameter $B = L_0\sqrt{\eta/G}$. In the case of no adhesions, only the parameters A and C are present in Eq. 3.5 and 3.6 and their values dictate both the size of the stretch-dominated region and the fraction of anterograde momentum due to stretching. Contributing to each of these dimensionless quantities is the degradation time-constant τ, so that a change in the half-life of the protein would change both A and C. A change in A or C alone would be interpreted as a change in γ or α, respectively. Figure 3.4A shows that a slower rate of protein density increase α (decreased C) and/or an increase in protein half-life τ (increased A and C) elevate the relative contribution of stretch-induced transport. Both of these changes result in a decrease in the overall demand for new protein while leaving the demand at the distal tip and the actual flux contribution of stretching unchanged (see Eq. 2.9 and 3.2). This part of the model best describes the cases of nerve elongation due to bodily growth and instances where axons are towed while unattached to a substrate.

One such example of this type of elongation is the extreme stretch-grown axons engineered by Pfister, et al. In these experiments, innervated rat axons were elongated to a length of 5 cm over the course of 14 days. During the first two days the rate of elongation was increased from 1 to 4 mm day^{-1}, and for the final twelve days the rate of elongation was held at 4 mm day^{-1} [74]. Using their data for microtubule density and axonal caliber before and after the elongation process, and the estimation that about 30% of tubulin in axons exists in soluble form [65], we can estimate the contribution that stretching makes to slow transport in these experiments. The values used to determine the parameters A and C are given in Table 3.2.

Figure 3.8 shows the contribution of stretching to overall transport in extreme stretch-grown axons. Under conditions of extreme stretch-growth, we observe that stretching accounts for 49.1% of anterograde momentum at the beginning of the third day of stretch-growth ($t = 0$, the beginning of the 4 mm day^{-1} elongation rate). At

Data for Pfister et al. Comparison		
Parameter	Value	Source
Length of Tubulin Dimer	.008 μm	[27]
Dimers / μm of microtubule	13/.008 = 1625	derived
Tubulin in Soluble Form	$\approx$ 30%	[65]
MT Density (0 days)	153 MT μm^{-2}	[74]
Axonal Caliber (0 days)	.43 μm^2	[74]
Approximate MT Density (0 days)	66 MT μm^{-1}	derived
Approximate Linear Tubulin Density (0 days)	153214 dimers μm^{-1}	derived
γ	4 mm day^{-1}	[74]
τ	73.6 days	[62]
Microtubule Density (14 days)	158 MT μm^{-2}	[74]
Axonal Caliber (14 days)	.58 μm^2	[74]
Approximate Microtubule Density (14 days)	92 MT μm^{-1}	derived
Approximate Linear Tubulin Density (14 days)	213571 dimers μm^{-1}	derived
α	4311 dimers μm^{-1} day^{-1}	derived
P_0 (2 days)	161836 dimers μm^{-1}	derived
L_0 (2 days)	3.5 mm	[74]
A	84.1	derived
C	1.96	derived

Table 3.2: Parameters Used for Applying this Model to the Data of Pfister, et al.

the end of the twelve-day span ($t = 13.7$) at this elongation rate, the percentage of anterograde momentum which is accounted for by stretching has only dropped to 41.1%. This is due to the fact that the elongation parameter is much greater than the density parameter ($A = 84.1, C = 1.96$). The studies of Pfister et al. showed that axons are able to grow at remarkable rates. Our model suggests that, when axons elongate at high rates in this manner, stretching makes a significant contribution to the transport of axonal materials.

Figure 3.8: The Contribution of Stretching to Slow Axonal Transport in Rapid Stretch-Grown Axons – We applied our model to the study of Pfister et al. [74] to see how much stretching contributed to anterograde transport in cases of extreme stretch-growth. In the study, axons were elongated at a rate of 4 mm day^{-1} for twelve days. These axons were free of adhesions along the length, so Eq. 5 and 6 were applied. Parameter values $A = 84.1$ and$C = 1.96$ were derived using values found in Table 3.2. (A) Flux profiles of anterograde transport at the beginning of the 12-day elongation period. Since A is much greater than C, the slope of the total flux profile is shallow and stretching is the dominant form of transport in most of the distal axon $\left(x_{1/2}/L = .509\right)$. (B) After twelve days, stretching is still the dominant form of transport in the distal 41% of the axon $\left(x_{1/2}/L = .589\right)$. (C) The relative contribution of stretching to anterograde momentum is given by the ratio $p_U(t)/p(t)$. Over the course of 12 days of elongation at 4 mm day^{-1} this ratio declines from .491 to .411, showing that stretching accounts for a significant amount of anterograde transport ($> 40\%$) when axons are elongated by extreme stretch-growth.

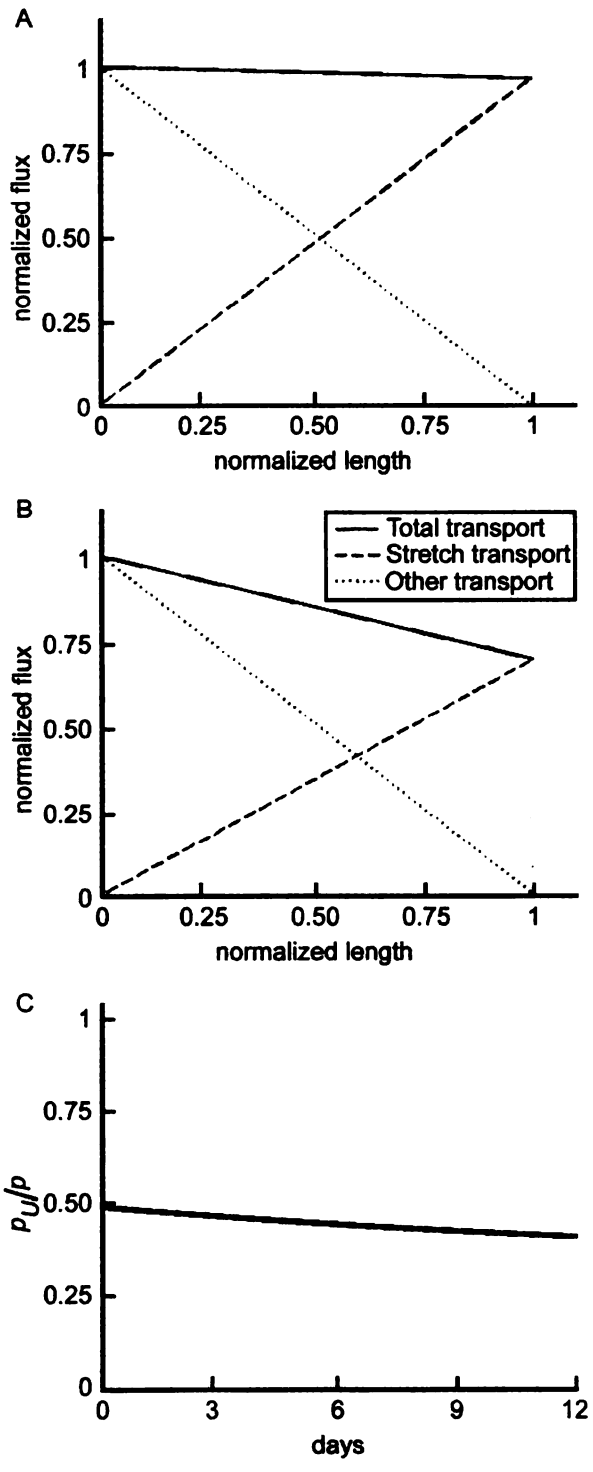
A
normalized flux
1
0.75
0.50
0.25
0
0
0.25
0.50
0.75
1
normalized length
B
Total transport
Stretch transport
Other transport
normalized flux
1
0.75
0.50
0.25
0
0
0.25
0.50
0.75
1
normalized length
C
p_U/p
1
0.75
0.50
0.25
0
0
3
6
9
12
days

Figure 3.8:

The parameter B enters in Eq. 3.3 when adhesions are present, and its effect on the point $x_{1/2}/L$ is much more pronounced than that of A or C. When $B = 7.06$, stretching is dominant in the distal 10% of the axon (Figs. 3.3, 3.4B) and there is almost no effect on the time evolution of $x_{1/2}/L$ when A and/or C take extreme values (Fig. 3.4C). Altering the value of B while keeping the other parameters constant amounts to modifying the ratio η/G, where η describes the strength of focal adhesions and G describes the viscosity of the axon. Axial forces are quickly dissipated by strong focal adhesions, so when this ratio is large there will be limited stretching of the axon. High axonal viscosity will lower force dissipation and a larger portion of the distal axon will experience stretching (assuming the same velocity of elongation). This part of the model best describes when axons are engaged in growth-cone mediated elongation along sticky substrates.

Figure 3.5 shows the system's sensitivity to the three parameters when adhesions are present and $P = L = 1$ (i.e. when $t = 0$). From previous work, we use baseline dimensionless parameter values $A = 1.98$, $B = 7.06$, and $C = 1.00$ (Table 3.1). Then, keeping two of these values fixed, we allow the third parameter to vary to study its effect on $x_{1/2}/L$. This value decreases with A and increases with B and C. To increase the size of the region where flux is dominated by stretching, $x_{1/2}/L$ must be lowered. Figure 3.5 shows that, in the presence of adhesions, increasing A or decreasing C only produce mild reductions in $x_{1/2}/L$. In contrast, reducing B can lead to as much as a doubling of the size of the stretch-dominated region. Anterograde momentum due to flux exhibits a similar dependence on A, B, and C, with a decrease in B effecting the largest possible increase in $p_{\mathrm{Ad}}(t) / (t)$ (Fig. 3.7). In general, decreasing adhesions along the length of the axon is the most effective method of increasing the contribution of stretching during elongation.

The location of addition of new material to an elongating axon and the need for active transport depend primarily on the mode by which the axon elongates. If

the framework of the existing axon is stationary, then all new material is added at the distal end (Fig. 3.1B). If axial tension is deforming the axon, then much of the material in the "new" segment of the axon has been transported there through stretching. Further, the existing length of the axon thins as a part of the stretching process and new material must be deposited there to reestablish a uniform diameter (Fig 3.1, C and D). Intercalated mass addition has been shown to occur in several systems, including rats [17], chicks [64], and *Drosophila* larvae [71]. With stretch-and-intercalation, the need for long bouts of active transport flux decreases, as much of the new material from the cell body is deposited along the length of the axon prior to the distal tip.

In terms of the PDEs that govern the motion of particles, stretching would add a spatially-dependent advection component to the equations of motion. For instance, if $c(x,t)$ represents the concentration of a protein in an axon, then the PDE which governs the concentration could be expressed as

$$\frac{\partial c}{\partial t} = D\frac{\partial^2 c}{\partial x^2} - \left(a + \gamma\frac{x}{L(t)}\right)\frac{\partial c}{\partial x} + g(x,t) \tag{3.43}$$

if there are no adhesions, or

$$\frac{\partial c}{\partial t} = D\frac{\partial^2 c}{\partial x^2} - \left(a + \frac{F_0 \sinh\left(x\sqrt{\eta/G}\right)}{\sqrt{\eta G}\cosh\left(L(t)\sqrt{\eta/G}\right)}\right)\frac{\partial c}{\partial x} + g(x,t) \tag{3.44}$$

when adhesions are present. When modeling the motion of intracellular particles, the populations are often divided between those that are free to diffuse in the cytoplasm and those that are bound by motors to microtubules [86, 33, 48]. It is unknown how axonal stretching affects different parts of the axon (such as the outer membrane, the cytoplasm, and the cytoskeleton). A question of interest that may need to be answered is whether different populations of particles (e.g. on- and off-track particles)

are equally affected by stretching.

One important aspect of stretch-induced elongation that we have not addressed here is short-term axonal thinning. In their extreme stretch-growth experiments, Pfister et al. demonstrated that stretching axons at too high a strain rate leads to rupture. However, when these tracts were properly conditioned, they were able to sustain elongation rates of up to 8 mm day^{-1} [74]. Although our current model would suggest that, in the absence of adhesions, increasing the elongation parameter A as much as possible would increase both the rate of elongation and the contribution of stretching to anterograde transport, there is certainly a limit as to how much stretching an axon or a nerve can support. A theoretical analysis of this limitation is required for optimal rates of axon / nerve regeneration to be determined.

It has long been thought that the rate of axonal regeneration is linked to the speed of slow axonal transport. When an axon elongates by axially oriented forces, much of the necessary transport in the axon occurs by stretching, reducing the demand for microtubule motor mediated transport. A way to increase regeneration rates in the presence of adhesions may be to condition the nerves to be more susceptible to stretching [43, 45]. In this way, transport due to stretching would increase slow axonal transport and allow faster rates of regeneration. We have shown that the stretch-dominated region and anterograde momentum of an axon/nerve are sensitive to the ratio of adhesions to axonal viscosity, and that stretching's influence can be increased by controlling this ratio. It may be possible to achieve this increase by modulating the expressions of cell-adhesion molecules (to decrease η) and/or cytoskeletal components (to increase G).

If one were to discover a drug that drastically increased both the rates of axonal elongation and slow axonal transport, it would be a major advance in the field of nerve regeneration. Stretching, a purely physical mechanism, possesses the ability to simultaneously accomplish both tasks. With advances in technology, axonal winches

(cables embedded in the body to stretch damaged nerves) and miniature robots that tow nerves will be possible. A combination of physical and cellular approaches (e.g. growth factors, gene therapy, neuronal stem cells) has the promise to yield phenomenal rates of exquisitely controlled nerve regeneration.

Chapter 4

Some Results on the Profile of Transported Material in Axons

4.1 Introduction

Of the mathematical models that have been done on the transport of materials in elongating axons [60, 86, 91, 62, 48], none have considered axonal stretching to play a significant role in slow axonal transport. Given that we have shown that stretching can account for up to 49% of slow axonal transport in certain situations, a future aim is to incorporate stretching into a slow axonal transport model. Some other goals of this study would be to determine the most relevant modes of transport and to extract the profile of active transport given what we know about the diffusion constant of the material and the transport due to low velocity transport (LVT). For instance, answers to questions such as the following could be pursued: Under what conditions do stretching and / or diffusion play a significant role in slow axonal transport? How does stretching reduce the need for carrier-mediated transport? How quickly can an axon restore itself after a sudden deformation? How is this ability altered when certain transport mechanisms are disabled or enhanced?

As a beginning to finding and answer to these questions, the case of transport by diffusion in a slowly elongating axon is explored. The role of diffusion is highest when there are concentration gradients along the length of the axon, and the biggest contribution to the maintenance of the axon is likely to be the reestablishment of a uniform concentration along the length.

We begin with the general advection-diffusion equation. Let $\phi(x,t)$ be the concentration profile of a material within the axon. The material is transported at an average velocity given by a and a stretch-induced mechanism given by $v(x,t)$, has diffusion constant D, and decays with characteristic time constant τ satisfying $\ln(2)\tau = t_{1/2}$. If the initial concentration in the axon is constant, there is an influx $J(t)$ of material at the cell body, and material does not flow out at the growth cone, then the system may be modeled as follows:

$$\begin{aligned} &\phi_t(x,t) + (a + v(x,t))\phi_x(x,t) = D\phi_{xx}(x,t) - \tfrac{1}{\tau}\phi \\ &\phi(x,0) = \phi_0 \\ &\phi_x(0,t) = -\frac{J(t)}{d} \qquad\qquad \phi_x(L(t),t) = 0 \end{aligned} \tag{4.1}$$

4.2 Fixing the Boundary

We see that this PDE is of the moving boundary type. Namely, the right endpoint of the system, $L(t)$, increases with t during outgrowth. To fix the boundary, we make the following substitutions. First we add tildes to denote the original variable.

$$\begin{aligned} &\tilde{\phi}_{\tilde{t}}(\tilde{x},\tilde{t}) + (a + \tilde{v})\,\phi_{\tilde{x}}(\tilde{x},\tilde{t}) = D\tilde{\phi}_{\tilde{x}\tilde{x}}(\tilde{x},\tilde{t}) - \tfrac{1}{\tau}\tilde{\phi} \\ &\tilde{\phi}(\tilde{x},0) = \phi_0 \\ &\tilde{\phi}_{\tilde{x}}(0,\tilde{t}) = -\frac{J(\tilde{t})}{d} \qquad\qquad \tilde{\phi}_{\tilde{x}}(\tilde{L}(\tilde{t}),\tilde{t}) = 0 \end{aligned} \tag{4.2}$$

Now we introduce the non-dimensional variable x, which will fix the right boundary at 1. We also introduce scaling factors t, ϕ, and L:

$$x = \frac{\tilde{x}}{L(t)} \qquad t = \frac{\tilde{t}}{t_0} \qquad \phi = \frac{\tilde{\phi}}{\phi_0} \qquad L = \frac{\tilde{L}}{L_0} \qquad v = \frac{t_0}{L_0}\tilde{v} \tag{4.3}$$

where t_0 is a time scale that will be determined later. In order to transform the equations we need to apply the chain rule to the derivatives.

$$\frac{\partial\tilde{\phi}}{\partial\tilde{t}} = \frac{\partial\tilde{\phi}}{\partial t}\frac{dt}{d\tilde{t}} + \frac{\partial\tilde{\phi}}{\partial x}\frac{\partial x}{\partial t}\frac{dt}{d\tilde{t}} = \frac{\phi_0}{t_0}\left[\phi_t - \frac{x}{L}\frac{\gamma t_0}{L_0}\phi_x\right] \tag{4.4}$$

$$\frac{\partial\tilde{\phi}}{\partial\tilde{x}} = \frac{\partial\tilde{\phi}}{\partial x}\frac{\partial x}{\partial\tilde{x}} + \frac{\partial\tilde{\phi}}{\partial t}\frac{\partial t}{\partial\tilde{x}} = \phi_0\frac{\partial\phi}{\partial x}\frac{1}{L_0 L(t)} + 0 = \frac{\phi_0}{L_0}\frac{\phi_x}{L(t)} \tag{4.5}$$

$$\frac{\partial^2\phi}{\partial\tilde{x}^2} = \frac{\partial}{\partial\tilde{x}}\left(\frac{\partial\phi}{\partial\tilde{x}}\right) = \frac{\partial}{\partial\tilde{x}}\left(\frac{\phi_0}{L_0}\frac{\phi_x}{L(t)}\right) = \frac{\phi_0}{L_0^2}\frac{\phi_{xx}}{(L(t))^2} \tag{4.6}$$

From previous work, we have the following definitions of $L(t)$ and $J(t)$:

$$L(t) = \frac{\tilde{L}(t)}{L_0} = \frac{L_0 + \gamma t_0 t}{L_0} = 1 + \frac{\gamma t_0}{L_0}t \tag{4.7}$$

$$J(t) = \phi_0\left[\frac{L_0 + \gamma t_0 t}{\tau} + \gamma\right] \tag{4.8}$$

These equations allow us to write the PDE in terms of non-dimensional variables:

$$\begin{aligned} &\phi_t = \frac{1}{Q^2}\frac{1}{L^2}\phi_{xx} + \left[A\frac{x}{L} - (\zeta + v)\right]\phi_x - \phi \\ &\phi(x,0) = 1 \\ &\phi_x(0,t) = \Gamma\left[L + A\right]L \qquad\qquad \phi_x(1,t) = 0 \end{aligned} \tag{4.9}$$

where $t_0 = \tau$ and the non-dimensional parameters are given as

$$\Gamma = \frac{L_0^2}{\tau d} \qquad \frac{1}{Q^2} = \frac{\tau D}{L_0^2} \qquad A = \frac{\gamma\tau}{L_0} \qquad \zeta = \frac{a\tau}{L_0}. \tag{4.10}$$

The parameters may be interpreted as follows: A is the elongation rate parameter, ζ is the velocity of active transport parameter, and $\Gamma/Q^2 = D/d = \delta$ is the diffusion parameter.

4.3 Transport By Diffusion Only

We consider a simplified form of the system where the stretching and active transport components of transport are comparatively small. That is, $\max\{a, \tilde{v}\}\frac{\tau}{L_0} << 1$. This corresponds to cases where carrier-mediated transport has been crippled, either by addition of a drug or because of a neurological disorder, and where stretching terms can be neglected (zero-to-minimal elongation or elongation in a highly adhesive environment). Omitting these terms, the system reduces to

$$\begin{aligned} &\phi_t = \frac{1}{Q^2}\frac{1}{L^2}\phi_{xx} + A\frac{x}{L}\phi_x - \phi \\ &\phi(x,0) = 1 \\ &\phi_x(0,t) = \Gamma\left[L + A\right]L \qquad \phi_x(1,t) = 0 \end{aligned} \tag{4.11}$$

4.3.1 $A = 0$

The case when $A = 0$ has special significance in that it represents the case when elongation has stopped (i.e. the adult phase after towed growth). The removal of this term significantly simplifies equation (4.11), giving

$$\begin{aligned} &\phi_t = \frac{1}{Q^2}\phi_{xx} - \phi \\ &\phi(x,0) = 1 \\ &\phi_x(0,t) = -\Gamma \qquad \phi_x(1,t) = 0 \end{aligned} \tag{4.12}$$

where $A = 0$, $L = 1$.

The transformed system has a constant influx at the cell body which, when coupled

with the constant decay along the length, will give a steady-state solution. We will then find the transient part of the solution by subtracting the steady-state from the PDE; i.e.

$$\phi(x,t) = \phi^{\infty}(x) + \phi^{T}(x.t).$$

Letting $t \to \infty$ we set $\phi_t = 0$ and get the ODE

$$\begin{aligned} &\phi^{\infty}_{xx} - Q^2\phi^{\infty} = 0 \\ &\phi^{\infty}_{x}(0) = -\Gamma \qquad\qquad \phi^{\infty}_{x}(1) = 0 \end{aligned} \tag{4.13}$$

The solution of this system is

$$\phi^{\infty}(x) = \frac{\Gamma}{Q}\left[\coth Q \cosh\left(Qx\right) - \sinh\left(Qx\right)\right]. \tag{4.14}$$

We find the transient solution $\phi^{T}(x,t)$ by substituting $\phi(x,t) = \phi^{T}(x,t) + \phi^{\infty}(x)$ into (4.12), which gives the transformed system:

$$\begin{aligned} &\phi^{T}_{t}(x,t) = \frac{1}{Q^2}\phi^{T}_{xx} - \phi^{T} \\ &\phi^{T}(x,0) = 1 - \phi^{\infty}(x) \\ &\phi^{T}_{x}(0,t) = -\Gamma - \phi^{\infty}_{x}(0) = 0 \qquad \phi^{T}_{x}(1,t) = 0 - \phi^{\infty}_{x}(1) = 0 \end{aligned} \tag{4.15}$$

where we have used that $\phi^{\infty}(x)$ solves (4.13). We find a solution to this homogeneous equation using separation of variables. Let

$$\phi^{T}(x,t) = X(x)T(t). \tag{4.16}$$

Inserting this into (4.15) gives the relationship

$$\frac{T'(t)}{T(t)} = \frac{Q^{-2}X''(x) - X(x)}{X(x)} = -\lambda \tag{4.17}$$

where λ is positive so that the solution decays as $t \to \infty$. Further, we must have that $\lambda \geq 1$ so that $X(x)$ will be constant (if $\lambda = 1$) or in terms of sine and cosine (as opposed to sinh and cosh) and will thus able to satisfy the no-flux boundary conditions. Solving each of these ODEs gives

$$T(t) = Ae^{-\lambda t} \tag{4.18}$$

$$X(x) = c_1 \sin\left(Q\sqrt{\lambda - 1}x\right) + c_2 \cos\left(Q\sqrt{\lambda - 1}x\right) \tag{4.19}$$

Applying the boundary condition at $x = 0$ on (4.19) gives that $c_1 = 0$. Thus, for our solution to exist, we must have that

$$\lambda_n = \left(\frac{n\pi}{Q}\right)^2 + 1 \tag{4.20}$$

where $n \in \mathbb{Z}$. Given that these eigenvalues are the same for $\pm n$, we only need to consider values of n greater than or equal to zero. Inserting this expression for λ_n gives an infinite number of eigenfunctions of the form

$$X_n(x) = c_n \cos(n\pi x). \tag{4.21}$$

Thus the solution of (4.15) is a linear combination of the form

$$\phi^T(x,t) = \sum_{n=0}^{\infty} A_n e^{-\lambda_n t} \cos(n\pi x). \tag{4.22}$$

We use the initial condition to solve for the constants A_n. Letting $t = 0$ we have

$$1 - \phi^{\infty}(x) = \sum_{n=0}^{\infty} A_n \cos(n\pi x). \tag{4.23}$$

We take advantage of the fact that, for $m, n \in \mathbb{Z}$,

$$\int_0^1 \cos(m\pi x)\cos(n\pi x)dx = \begin{cases} 0 & (m \neq n) \\ \frac{1}{2} & (m = n) \end{cases} \tag{4.24}$$

to solve for each constant. Integrating (4.23) with respect to the weight function $\cos(m\pi x)$ gives

$$A_m = \begin{cases} \int_0^1 1 - \phi^\infty(x)\,dx = 1 - \Gamma/Q^2 & m = 0 \\ 2\int_0^1 \cos(m\pi x) - \phi^\infty(x)\cos(m\pi x)dx = \frac{-2\Gamma}{(m\pi)^2+Q^2} & m = 1, 2, \ldots \end{cases} \tag{4.25}$$

Thus we have the complete solution to the $\gamma = 0$ system:

$$\phi(x,t) = \phi^T(x,t) + \phi^\infty(x). \tag{4.26}$$

4.3.2 $A = \epsilon$

We next turn to the case where growth rates are of order $\epsilon << 1$. The perturbed system is of the form

$$\begin{aligned} &\phi_t = \left(\tfrac{\epsilon x}{1+\epsilon t}\right)\phi_x + \frac{1}{Q^2}\frac{1}{(1+\epsilon t)^2}\phi_{xx} - \phi \\ &\phi(x,0) = 1 \\ &\phi_x(0,t) = -\Gamma\left[1 + \epsilon\,(2t+1) + \epsilon^2\left(t^2+t\right)\right] \qquad \phi_x(1,t) = 0 \end{aligned} \tag{4.27}$$

We write the solution to the perturbed system as

$$\phi(x,t) = \phi^0(x,t) + \epsilon\phi^1(x,t) + \epsilon^2\phi^2(x,t) + \ldots \tag{4.28}$$

Rewriting the PDE in (4.27) gives the following:

$$\begin{aligned}\left(1+2\epsilon t+\epsilon^2 t^2\right)\left(\phi_t^0+\epsilon\phi_t^1+\ldots\right) &= \left(\epsilon x+\epsilon^2 xt\right)\left(\phi_x^0+\epsilon\phi_x^1+\ldots\right)\\ &+\frac{1}{Q^2}\left(\phi_{xx}^0+\epsilon\phi_{xx}^1+\ldots\right)\\ &-\left(1+2\epsilon t+\epsilon^2 t^2\right)\left(\phi^0+\epsilon\phi^1+\ldots\right)\end{aligned} \tag{4.29}$$

Breaking this down into equations of common powers of ϵ gives

$$\begin{aligned}&\phi_t^0=\tfrac{1}{Q^2}\phi_{xx}^0-\phi^0\\ \epsilon^0:\ &\phi^0(x,0)=1\\ &\phi_x^0(0,t)=-\Gamma \qquad \phi_x^0(1,t)=0\end{aligned} \tag{4.30}$$

$$\begin{aligned}&\phi_t^1-\tfrac{1}{Q^2}\phi_{xx}^1+\phi^1=x\phi_x^0-2t\left(\phi^0+\phi_t^0\right)\\ \epsilon^1:\ &\phi^1(x,0)=0\\ &\phi_x^1(0,t)=-\Gamma\left(2t+1\right) \qquad \phi_x^1(1,t)=0\end{aligned} \tag{4.31}$$

The ϵ^0 system (4.30) is identical to the $A=0$ system (4.12). Therefore, the solution of the ϵ^0 case is the same as before:

$$\phi^0(x,t)=\frac{\Gamma}{Q}\left[\coth\left(Q\right)\cosh\left(Qx\right)-\sinh\left(Qx\right)\right]+\sum_{n=0}^{\infty}A_n e^{-\lambda_n t}\cos\left(n\pi x\right). \tag{4.32}$$

Finding a solution to the PDE (4.31) requires that we transform the system before we attempt to solve. The semi-infinite time domain and zero initial condition make this system a candidate for solving via the Laplace Transform. Define the transform of $\phi^1(x,t)$ as

$$\mathcal{L}\left\{\phi^1(x,t)\right\}=\int_0^{\infty}e^{-st}\phi^1\left(x,t\right)\,dt=\psi\left(x,s\right).$$

Then, applying the derivative rule for Laplace Transforms we have

$$\mathcal{L}\left\{\phi_t^1\right\} = s\psi(x,s) - \phi^1(x,0) = s\psi(x,s).$$

The left hand side of the PDE in (4.31) becomes

$$\mathcal{L}\{\text{LHS}\}: \quad s\psi - \frac{1}{Q^2}\psi_{xx} + \psi = (1+s)\psi - \frac{1}{Q^2}\psi_{xx}. \tag{4.33}$$

We expand the right-hand side of the PDE by substituting in the ϵ^0 solution:

$$\begin{aligned} &\cosh(Qx)\left[-2t\coth(Q)\frac{\Gamma}{Q}\right] - \Gamma x\cosh(Qx) \\ \text{RHS:} \quad &+ 2t\frac{\Gamma}{Q}\sinh(Qx) + \Gamma\coth(Q)x\sinh(Qx) \\ &+ \sum_{n=0}^{\infty} A_n 2t\left(\lambda_n - 1\right)e^{-\lambda_n t}\cos(n\pi x) - A_n(n\pi)e^{-\lambda_n t}x\sin(n\pi x) \end{aligned} \tag{4.34}$$

Each of these terms has a straight-forward Laplace Transform, with a shift theorem applied to the terms in the series:

$$\text{Shift:} \quad \text{If } \mathcal{L}\{f(t)\} = F(s), \text{ then } \mathcal{L}\left\{e^{-at}f(t)\right\} = F(s+a).$$

The Laplace Transform of the right-hand side, then, is

$$\begin{aligned} &\cosh(Qx)\left[\frac{-2\Gamma\coth(Q)}{Qs^2}\right] - x\cosh(Qx)\frac{\Gamma}{s} \\ \mathcal{L}\{\text{RHS}\}: \quad &+ \sinh(Qx)\frac{2\Gamma}{Qs^2} + x\sinh(Qx)\frac{\Gamma\coth(Q)}{s} \\ &+ \sum_{n=0}^{\infty}\frac{2A_n\left(\lambda_n - 1\right)}{\left(s+\lambda_n\right)^2}\cos(n\pi x) - \frac{A_n(n\pi)}{s+\lambda_n}x\sin(n\pi x) \end{aligned} \tag{4.35}$$

Particular Solution

The solution of this equation in the Laplace domain requires a homogeneous and

a particular solution. As the particular solution will have an effect on the boundary conditions, we find this first and then solve the homogeneous equation with the modified boundary conditions.

Given the form of (4.35), we guess that the particular solution $\psi_p(x,s)$ will have the form

$$\begin{aligned}\psi_p(x,s) = &(\varphi_1(s) + x\varphi_2(s))\cosh(Qx) + (\varphi_3(s) + x\varphi_4(s))\sinh(Qx) \\ &+ \sum_{n=0}^{\infty} (V_n(s) + xW_n(s))\cos(n\pi x) + (Y_n(s) + xZ_n(s))\sin(n\pi x)\end{aligned} \tag{4.36}$$

Substituting this equation into (4.33), $(1+s)\psi - \frac{1}{Q^2}\psi_{xx}$, and equating with (4.35) gives a system of eight equations:

$$\frac{2}{Q}\varphi_4(s) - s\varphi_1(s) = \frac{-2\Gamma}{Qs^2}\coth(Q) \tag{4.37a}$$

$$-s\varphi_2(s) = \frac{-\Gamma}{s} \tag{4.37b}$$

$$\frac{2}{Q}\varphi_2(s) - s\varphi_3(s) = \frac{2\Gamma}{Qs^2} \tag{4.37c}$$

$$-s\varphi_4(s) = \frac{\Gamma\coth(Q)}{s} \tag{4.37d}$$

$$-(s+\lambda_n)W_n(s) = 0 \tag{4.37e}$$

$$-W_n(s)\frac{2\pi n}{Q^2} - (s+\lambda_n)Y_n(s) = 0 \tag{4.37f}$$

$$-(s+\lambda_n)Z_n(s) = \frac{-A_n(n\pi)}{s+\lambda_n} \tag{4.37g}$$

$$\frac{2\pi n}{Q^2}Z_n(s) - (s+\lambda_n)V_n(s) = \frac{2A_n(\lambda_n - 1)}{(s+\lambda_n)^2} \tag{4.37h}$$

which, since we have $s, \lambda_n > 0$ and $\lambda_n - 1 = (n\pi)^2/Q^2$, yields only three non-zero

functions: $\varphi_2(s)$, $\varphi_4(s)$, and $Z_n(s)$. The particular solution, then, is given as

$$\psi_p(x,s) = \frac{-\Gamma}{s^2} x\cosh(Qx) + \frac{\Gamma}{s^2}\coth(Q)x\sinh(Qx) - \sum_{n=0}^{\infty}\frac{A_n(n\pi)}{(s+\lambda_n)^2}x\sin(n\pi x). \tag{4.38}$$

Homogeneous Solution

With the particular solution in hand, we determine the homogeneous problem to be solved by adding the particular solution's contribution to the boundary conditions. Since

$$\psi_{p_x}(0,s) = \frac{-\Gamma}{s^2} \qquad \psi_{p_x}(1,s) = \frac{\Gamma Q}{s^2\sinh(Q)} - \sum_{n=0}^{\infty}\frac{(-1)^n A_n(n\pi)^2}{(s+\lambda_n)^2} \tag{4.39}$$

the homogeneous problem to be solved is as follows:

$$\begin{aligned}
&(1+s)\psi_h - \frac{1}{Q^2}\psi_{hxx} = 0 \\
&\psi^1_{h_x}(0,s) = \psi_x(0,s) - \psi_{p_x}(0,s) = \frac{-2\Gamma}{s^2} - \frac{\Gamma}{s} - \left(-\frac{\Gamma}{s^2}\right) = \frac{-\Gamma}{s^2} - \frac{\Gamma}{s} \\
&\psi^1_{h_x}(1,s) = \psi_x(1,s) - \psi_{p_x}(1,s) = \frac{-\Gamma Q}{s^2\sinh(Q)} + \Sigma_{n=0}^{\infty}\frac{(-1)^n A_n(n\pi)^2}{(s+\lambda_n)^2}
\end{aligned} \tag{4.40}$$

The equation is solved as

$$\psi_h(x,s) = c_1(s)e^{Q\sqrt{1+s}x} + c_2(s)e^{-Q\sqrt{1+s}x} \tag{4.41}$$

where the functions of s are

$$c_1(s) = c_2(s) - \frac{\Gamma}{Q\sqrt{1+s}}\left(\frac{1}{s^2} + \frac{1}{s}\right) \tag{4.42}$$

$$c_2(s) = \frac{1}{1-e^{-2Q\sqrt{1+s}}}\left[\frac{\Gamma}{Q\sqrt{1+s}}\left(\frac{1}{s^2}+\frac{1}{s}\right) - \frac{\Gamma e^{-Q\sqrt{1+s}}}{s^2\sqrt{1+s}\sinh(Q)} + \frac{e^{-Q\sqrt{1+s}}}{Q\sqrt{1+s}}\sum_{n=0}^{\infty}\frac{(-1)^n A_n (n\pi)^2}{(s+\lambda_n)^2}\right] \tag{4.43}$$

Note that the term factored out of equation (4.43) can be expressed as an infinite series:

$$\frac{1}{1-e^{-2Q\sqrt{1+s}}} = \sum_{k=0}^{\infty} e^{-2Qk\sqrt{1+s}}.$$

Further, the problem that we may end up with an non-invertible function of s is avoided since the term that is subtracted in (4.42) is exactly what is needed to cancel the order 1 term in $c_2(s)$. Thus, every exponent will be negative and all terms in the homogeneous solution will be invertible. The homogeneous solution is thus composed

of eight parts which can each be inverted:

$$\begin{aligned}
\psi_h(x,s) = & \frac{-\Gamma}{\sinh(Q)s^2}\sum_{k=0}^{\infty}\frac{e^{-Q\sqrt{1+s}(-x+1+2k)}}{\sqrt{1+s}} \\
& + \frac{1}{Q}\sum_{n=0}^{\infty}\frac{(-1)^n(n\pi)^2 A_n}{(s+\lambda_n)^2}\sum_{k=0}^{\infty}\frac{e^{-Q\sqrt{1+s}(-x+1+2k)}}{\sqrt{1+s}} \\
& + \frac{\Gamma}{Qs^2}\sum_{k=0}^{\infty}\frac{e^{-Q\sqrt{1+s}(-x+2+2k)}}{\sqrt{1+s}} \\
& + \frac{\Gamma}{Qs}\sum_{k=0}^{\infty}\frac{e^{-Q\sqrt{1+s}(-x+2+2k)}}{\sqrt{1+s}} \\
& + \frac{\Gamma}{Qs^2}\sum_{k=0}^{\infty}\frac{e^{-Q\sqrt{1+s}(x+2k)}}{\sqrt{1+s}} \\
& + \frac{\Gamma}{Qs}\sum_{k=0}^{\infty}\frac{e^{-Q\sqrt{1+s}(x+2k)}}{\sqrt{1+s}} \\
& - \frac{\Gamma}{\sinh(Q)s^2}\sum_{k=0}^{\infty}\frac{e^{-Q\sqrt{1+s}(x+1+2k)}}{\sqrt{1+s}} \\
& + \frac{1}{Q}\sum_{n=0}^{\infty}\frac{(-1)^n(n\pi)^2 A_n}{(s+\lambda_n)^2}\sum_{k=0}^{\infty}\frac{e^{-Q\sqrt{1+s}(x+1+2k)}}{\sqrt{1+s}}
\end{aligned} \tag{4.44}$$

We label the eight parts of this equation $\beta_i(x,s)$, $i = 1,2,..,8$. Due to the quickly decaying nature of the series in (4.44) the inversions can be computed term-by-term. Each inversion is similar; the only differences being the constants (with respect to s) in the exponents and the factor of $1/s$, $1/s^2$, or $1/(s+\lambda_n)^2$ in front of the infinite sum. The inversions, then, may be found using the following formulae [28, 16]:

$$\mathcal{L}^{-1}\left\{\frac{e^{-a\sqrt{s}}}{\sqrt{s}}\right\} = \frac{1}{\sqrt{\pi t}}e^{-a^2/(4t)}$$

$$\mathcal{L}^{-1}\left\{\frac{1}{s}\right\} = 1$$

$$\mathcal{L}^{-1}\left\{\frac{1}{s^2}\right\} = t$$

$$\mathcal{L}^{-1}\{F(s+c)\} = e^{-ct}f(t)$$

$$\mathcal{L}^{-1}\{F(s)G(s)\} = f(t) * g(t) = \int_0^t f(t-v)g(v)\,dv$$

In short, we use the first inversion formula with the shift theorem ($c = 1$), and then apply convolution to complete the inversion process. The full process is shown for $\beta_1(x,s)$ (the other seven inversions are similar).

$$\begin{aligned}
b_1(x,t) &= \mathcal{L}^{-1}\{\beta_1(x,s)\} \\
&= \mathcal{L}^{-1}\left\{\frac{-\Gamma}{\sinh(Q)}\sum_{k=0}^{\infty}\frac{1}{s^2}\cdot\frac{e^{-Q\sqrt{1+s}(-x+1+2k)}}{\sqrt{1+s}}\right\} \\
&= \frac{-\Gamma}{\sinh(Q)}\sum_{k=0}^{\infty} t * \left(\frac{e^{-t}}{\sqrt{\pi t}}e^{\frac{-[Q(-x+1+2k)]^2}{4t}}\right) \\
&= \frac{-\Gamma}{\sinh(Q)}\sum_{k=0}^{\infty}\int_0^t (t-v)\frac{e^{-v}}{\sqrt{\pi v}}e^{\frac{-[Q(-x+1+2k)]^2}{4v}}\,dv \\
&= \frac{-2\Gamma}{\sqrt{\pi}\sinh(Q)}\sum_{k=0}^{\infty}\int_0^{\sqrt{t}} (t-u^2)e^{\frac{-[Q(-x+1+2k)]^2}{4u^2}-u^2}\,du
\end{aligned} \tag{4.45}$$

The substitution $u = \sqrt{v}$ was made in the integral to eliminate the singularity $1/\sqrt{v}$ when $v = 0$. A singularity still remains in the exponent when $u = 0$, but the integrand converges to zero as $u \to 0$, guaranteeing the convergence of each integral. Further, the series in k will converge $\forall t > 0$ since each integral is bounded by $t^{3/2}e^{\frac{-(Qk)^2}{t}}$.

The other seven inversions are:

$$b_2(x,t) = \frac{2}{Q\sqrt{\pi}} \sum_{n=0}^{\infty} (-1)^n A_n (n\pi)^2 \sum_{k=0}^{\infty} \int_0^{\sqrt{t}} (t-u^2) e^{\frac{-[Q(-x+1+2k)]^2}{4u^2} - \lambda_n \left(t-u^2\right) - u^2} du \tag{4.46}$$

$$b_3(x,t) = \frac{2\Gamma}{Q\sqrt{\pi}} \sum_{k=0}^{\infty} \int_0^{\sqrt{t}} \left(t-u^2\right) e^{\frac{-[Q(-x+2+2k)]^2}{4u^2} - u^2} du \tag{4.47}$$

$$b_4(x,t) = \frac{2\Gamma}{Q\sqrt{\pi}} \sum_{k=0}^{\infty} \int_0^{\sqrt{t}} e^{\frac{-[Q(-x+2+2k)]^2}{4u^2} - u^2} du \tag{4.48}$$

$$b_5(x,t) = \frac{2\Gamma}{Q\sqrt{\pi}} \sum_{k=0}^{\infty} \int_0^{\sqrt{t}} \left(t-u^2\right) e^{\frac{-[Q(x+2k)]^2}{4u^2} - u^2} du \tag{4.49}$$

$$b_6(x,t) = \frac{2\Gamma}{Q\sqrt{\pi}} \sum_{k=0}^{\infty} \int_0^{\sqrt{t}} e^{\frac{-[Q(x+2k)]^2}{4u^2} - u^2} du \tag{4.50}$$

$$b_7(x,t) = \frac{-2\Gamma}{\sqrt{\pi}\sinh(Q)} \sum_{k=0}^{\infty} \int_0^{\sqrt{t}} \left(t-u^2\right) e^{\frac{-[Q(x+1+2k)]^2}{4u^2} - u^2} du \tag{4.51}$$

$$b_8(x,t) = \frac{2}{Q\sqrt{\pi}} \sum_{n=0}^{\infty} (-1)^n A_n (n\pi)^2 \sum_{k=0}^{\infty} \int_0^{\sqrt{t}} \left(t-u^2\right) e^{\frac{-[Q(x+1+2k)]^2}{4u^2} - \lambda_n \left(t-u^2\right) - u^2} du \tag{4.52}$$

The sum of these eight functions gives the inversion of the homogeneous solution. If

we let $p(x,t) = \mathcal{L}^{-1}\left\{\psi p(x,s)\right\}$, then we get

$$p(x,t) = -\Gamma t x\left(\cosh(Qx) - \coth(Q)\sinh(Qx)\right) - \sum_{k=0}^{\infty} A_n(n\pi)te^{-\lambda_n t}x\sin(n\pi x) \tag{4.53}$$

The solution of the system (4.31), then, is

$$\phi^1(x,t) = \sum_{i=1}^{8} b_i(x,t) + p(x,t). \tag{4.54}$$

Future work will include the inclusion of other processes (active transport, stretching). Given the complexity of the equations, numerical schemes will need to be employed to study the system.

Chapter 5

Conclusions

While there have been tremendous advances in the field of nerve repair, many challenges to efficient regeneration remain. A fundamental matter to this aim is a thorough understanding of the way in which axons elongate: whether that elongation happens naturally or is artificially induced. The current model of how this occurs, the tip-growth model, posits that the existing axon is stationary during elongation, with all new mass addition occurring at the distal end of the axon [26]. If this is indeed the case, then the goal for therapies should be to increase both the production of cytoskeletal materials and the transport of those materials to the growth cone. A major pillar of the tip-growth model is that axonal lengthening happens as a result of the activities of the production and transport mechanisms. If lengthening occurs, however, through a combination of axially oriented forces and deformation (stretching) of the axonal framework, very different strategies for accelerating elongation should be pursued.

The problem of axonal elongation is approached from a purely physical standpoint; while the molecular foundations of the physical processes are understood and appreciated, they are not directly modeled in this work. The goal of this work is to join others [74, 1, 7, 50] in moving the trend away from tip-growth-based methods

and toward physical approaches based on forces and stretching. The point to be made then, is that tip-growth has inadequacies and that axonal stretching can explain phenomena on top of what the tip-growth model can account for. The problems of how forces are generated and how they may be increased, the ways in which the composition of the cytoskeleton and axoplasm affect axonal viscosity, and the modulation of cell adhesiveness (just to name a few) are each, in themselves, expansive enough to fill an entire dissertation. As the ideas of force and stretching being major players in elongation continues to gain traction, molecular-based approaches to these topics are sure to receive more attention.

In Chapter 1, a biophysical model of axonal elongation is introduced and developed. Rather than focusing solely on the rate of elongation, the profile of deformation along entire axons was studied to determine the axon's viscoelastic response to tension. In the presence of adhesions, the maximum velocity was shown to be a function of the axial force, the viscosity of the axon, and the strength of the adhesions. The model predicts a constant rate of elongation given a constant force and predicts that deformation of the framework will occur in the distal regions of the axon. Further, this deformation is dependent on the ratio of axonal viscosity to substrate adhesions. The results of this work have been recognized as a part of the renaissance of the role of physical forces in the problem of elongation and regeneration [31].

Chapter 2 deals primarily with the demands on neuronal cell bodies to supply their axons with enough protein for healthy elongation and upkeep. Instead of protein production and transport being the driving forces of elongation, these factors are assumed to be dependent on the rate of axonal lengthening and radial growth. Experiments done on *Drosophila* larvae revealed that mitochondrial density was uniform and both mitochondrial density and axonal length increased linearly during instar development. Flux measurements led to an estimate that the half-life of mitochondria in *Drosophila* nerves is approximately 35 days.

The third chapter builds upon the work of the first two chapters. It combines the theories of how stretching transports the existing axonal framework and the demands that growth places on neuronal cell bodies. Since stretching has not yet been considered to contribute to the process, two new measurements were conceived which are meant to weigh stretching's contribution to slow axonal transport. The first determines the portion of the axon where stretching accounts for greater than half of necessary anterograde flux (this necessary flux was modeled in Chapter 2). The second measures the contribution that stretching makes to total anterograde transport in the axon (referred to as anterograde momentum). Whereas the first measure refers to a relative position along the axon, the value of the second measure gives information about stretching's total contribution in the axon. It was shown, for both of these measures, that stretching can be dominant as a form of anterograde flux in the distal half of the axon (in the case of the first measure) and can contribute to nearly half of all necessary anterograde flux (in the case of the second measure). The main hindrance to stretching's effects was shown to be substrate adhesions. It was concluded that stretching axons may be an effective way of accelerating regeneration, specifically because it simultaneously increases elongation and slow transport.

If stretching of the axonal framework is significant, then PDE models of slow axonal transport must account for these effects. Chapter 4 contains some of my preliminary attempts at analyzing PDE models of slow axonal transport. Here, a model where diffusion is the only mode of transport is solved analytically for the case of no growth (steady-state length) and is solved asymptotically for the case of small growth. Given the analysis of PDE models that did not consider stretching [86, 60, 33], there would seem to be many future projects involving the analysis (analytical and numerical) of elongation and transport with the effects of axonal stretching included.

This thesis challenges the tip-growth model and introduces a model where axial forces, along with intrinsic and extrinsic factors (viscoelasticity and friction, respec-

tively), determine the rate of elongation and the magnitude of deformation of the axon. It (1) demonstrates that axons grown on substrates respond to forces and undergo non-uniform deformation, and this deformation is greatest near the distal end, (2) predicts the flux that must occur in response to axonal growth and protein degradation in order to sustain healthy elongation, (3) shows that stretching not only can increase the rate of elongation, but can play a major role in the slow transport of axonal proteins, and (4) lays the foundation for the incorporation of axonal stretching into PDE models of elongation and transport. Neurites, in their quest to become innervated axons, undergo bouts of elongation, retraction, turning, and branching. The search for therapies that produce rapid rates of regeneration is much like the quest of the neurite. As the evidence continues to mount, researchers should turn away from pursuing therapies that assume the tip-growth model and follow the guidance cues provided by studies that have revealed the importance of forces and axonal stretching. With this thesis, I hope that the neuroscience community is one step closer to moving in that direction and achieving a breakthrough in the treatment of damaged nerves.

BIBLIOGRAPHY

[1] I. Abe, N. Ochiai, N. Ichimura, A. Tsujino, J. Sun, and Y. Hara. Internodes can nearly double in length with gradual elongation of the adult rat axon. *J. Orthop. Res.*, 22:571–577, 2004.

[2] M. Aeschlimann. *Biophysical models of axonal pathfinding.* PhD thesis, University of Lausanne, 2000.

[3] M. Aeschlimann and L. Tettoni. Biophysical model of axonal pathfinding. *Neurocomputing*, 38:87–92, 2001.

[4] P.W. Baas and F.J. Ahmad. Force generation by cytoskeletal motor proteins as a regulator of axonal elongation and retraction. *Trends Cell Biol.*, 11:244–249, 2001.

[5] P.W. Baas, C. Vidya Nadar, and K.A. Myers. Axonal transport of microtubules: the long and short of it. *Traffic*, 7:490–498, 2006.

[6] J.R. Bamburg, D. Bray, and K. Chapman. Assembly of microtubules at the tip of growing axons. *Nature*, 321:788–790, 1986.

[7] R. Bernal, P. A. Pullarkat, and F. Melo. Mechanical properties of axons. *Phys. Rev. Lett.*, 99(1):018301, 2007.

[8] F. Bradke and C.G. Dotti. The role of local actin instability in axon formation. *Science*, 283:1931–1934, 1999.

[9] D. Bray. Surface movements during the growth of single explanted neurons. *Proc. Natl. Acad. Sci. USA*, 65:905–910, 1970.

[10] D. Bray. Branching patterns of individual sympathetic neurons in culture. *J. Cell Biol.*, 56:702–712, 1973.

[11] D. Bray. Axonal growth in response to experimentally applied mechanical tension. *Dev. Biol.*, 102:379–389, 1984.

[12] A. Brown. Slow axonal transport: stop and go traffic in the axon. *Nat. Rev. Mol. Cell Biol.*, 1:153–156, 2000.

[13] A. Brown. Axonal transport of membranous and nonmembranous cargoes: a unified perspective. *J. Cell Biol.*, 160:817–821, 2003.

[14] A. Brown, L. Wang, and P. Jung. Stochastic simulation of neurofilament transport in axons: the.

[15] K.B. Buck and J.Q. Zheng. Growth cone turning induced by direct local modification of microtubule dynamics. *J. Neurosci.*, 22:9358–9367, 2002.

[16] R.G. Buschman. *Integral Transformations, Operational Calculus, and Generalized Functions.* Kluwer Academic Publishers, 1996.

[17] R.B. Campenot. The regulation of nerve fiber length by intercalated elongation and retraction. *Brain Res.*, 352:149–154, 1985.

[18] R.B. Campenot and H. Eng. Protein synthesis in axons and its possible functions. *J. Neurocytol.*, 29:793–398, 2000.

[19] C.M. Cesa, N. Kirchgessner, D. Mayer, U.S. Schwarz, B. Hoffman, and R. Merkel. Micropatterned silicone elastomer substrates for high resolution analysis of cellular force patterns. *Rev. Sci. Instrum.*, 78:034301, 2007.

[20] S.R. Chada and P.J. Hollenbeck. Mitochondrial movement and positioning in axons: the role of growth factor signaling. *J. Exp. Biol.*, 206:1985–1992.

[21] S.R. Chada and P.J. Hollenbeck. Nerve growth factor signaling regulates motility and docking of axonal mitochondria. *Curr. Biol.*, 14:1272–1276, 2004.

[22] D.T. Chang and I.J. Reynolds. Mitochondrial trafficking and morphology in healthy and injured neurons. *Prog. Neurobiol.*, 80:241–268, 2006.

[23] S. Chang, V.I. Rodionov, G.G. Borisy, and S.V. Popov. Transport and turnover of microtubules in frog neurons depend on the pattern of axonal growth. *J. Neurosci.*

[24] S. Chang, T.M. Svitkina, G.G. Borisy, and S.V. Popov. Speckle microscopic evaluation of microtubule transport in growing nerve processes. *Nat. Cell Biol.*, 1:399–403, 1999.

[25] T.J. Dennerll, P. Lamoureux, R.E. Buxbaum, and S.R. Heidemann. The cytomechanics of axonal elongation and retraction. *J. Cell Biol.*, 109:3073–3083, 1989.

[26] E. W. Dent and F. B. Gertler. Cytoskeletal dynamics and transport in growth cone motility and axon guidance. *Neuron*, 40:209–227, 2003.

[27] A. Desai and T.J. Mitchison. Microtubule polymerization dynamics. *Annu. Rev. Cell Dev. Biol.*, 13:83–117, 1997.

[28] G. Doetsch. *Guide to the Applications of the Laplace and Z-Transforms.* Van Norstrand Reinhold, London, 1971.

[29] C.G. Dotti, C.A. Sullivan, and G.A. Banker. The establishment of polarity by hippocampal neurons in culture. *J. Neurosci.*, 8:1454–1468, 1988.

[30] H. Eng, K. Lund, and R.B. Campenot. Synthesis of beta-tubulin, actin, and other proteins in axons of sympathetic neurons in compartmented cultures. *J. Neurosci.*, 19:1–9, 1999.

[31] K. Franze and J. Guck. The biophysics of neuronal growth. *Rep. Prog. Phys.*, 73:094601, 2010.

[32] R.L. Frederick and J.M. Shaw. Moving mitochondria: establishing distribution of an essential organelle. *Traffic*, 8:1668–1675, 2007.

[33] A. Friedman and G. Craciun. A model of intracellular transport of particles in an axon. *J. Math. Biol.*, 51:217–246, 2005.

[34] C.G. Galbraith and M.P. Sheetz. A micromachined device provides a new bend on fibroblast traction forces. *Proc. Natl. Acad. Sci. USA.*, 94:9114–9118, 1997.

[35] P. Godement, C.L. Wang, and C.A. Mason. Retinal axon divergence in the optic chiasm: dynamics of growth cone behavior at the midline. *J. Neurosci.*, 14:7024–7039, 1994.

[36] B.P. Graham and A. van Ooyen. Mathematical modelling and numerical simulation of the morphological development of neurons. *BMC Neurosci.*, 7(Suppl 1: S9):1–12, 2006.

[37] S.R. Heidemann, P. Lamoureux, K. Ngo, M. Reynolds, and R.E. Buxbaum. Open-dish incubator for live cell imagin with an inverted microscope. *Biotechniques*, 35:708–714,716, 2003.

[38] S.R. Heidemann and D. Wirtz. Towards a regional approach to cell mechanics. *Trends Cell Biol.*, 14:160–166, 2004.

[39] N. Hirokawa. Cross-linker system between neurofilaments, microtubules, and membranous organelles in frog axons revealed by the quick-freeze, deep-etching method. *J. Cell Biol.*, 94:129–142, 1982.

[40] N. Hirokawa, Y. Noda, Y. Tanaka, and S. Niwa. Kinesin superfamily proteins and intracellular transport. *Nat. Rev. Mol. Cell Biol.*, 10:682–696, 2009.

[41] N. Hirokawa, S. Terada, T. Funakoshi, and S. Takeda. Slow axonal transport: the subunit transport model. *Trends Cell Biol.*, 7:384–388, 1997.

[42] A.L. Hodgkin and A.F. Huxley. A quantitative description of membrane current and its application to conduction and excitation in nerve. *J. Physiol.*, 117:500–544, 1952.

[43] P.N. Hoffman. A conditioning lesion induces changes in gene expression and axonal transport that enhance regeneration by increasing the intrinsic growth state of axons. *Exp. Neurol.*, 223:11–18.

[44] P.J. Hollenbeck. The pattern and mechanism of mitochondrial transport in axons. *Front Biosci.*, 1:d91–d102, 1996.

[45] K. Kadoya, S. Tsukada, P. Lu, G. Coppola, D. Geschwind, M.T. Filbin, A. Blesch, and M.S. Tuszynski. Combined intrinsic and extrinsic neuronal mechanisms facilitate bridging axonal regeneration one year after spinal cord injury. *Neuron*, 64:165–172.

[46] G. Kiddie, D. McLean, A. Van Ooyen, and B. Graham. Biologically plausible models of neurite outgrowth. *Prog. Brain Res.*, 147:67–80, 2005.

[47] A. Kis, S. Kasas, B. Babic, A.J. Kulik, W. Benoit, G.A. Briggs, C. Schonenberger, S. Catsicas, and L. Forro. Nanomechanics of microtubules. *Phys. Rev. Lett.*, 89:248101, 2002.

[48] A.V. Kuznetsov and A.A. Avramenko. A macroscopic model of traffic jams in axons. *Math. Biosci.*, 218:142–152, 2009.

[49] F. Lafont, M. Rouget, A. Rousselet, C. Valenza, and A. Prochiantz. Specific responses of axons and dendrites to cytoskeleton perturbations: an in vitro study. *J. Cell Sci.*, 104 (Pt. 2):433–443, 1993.

[50] P. Lamoureux, R.E. Buxbaum, and S.R. Heidemann. Direct evidence that growth cones pull. *Nature*, 340:159–162, 1989.

[51] P. Lamoureux, G. Ruthel, R.E. Buxbaum, and S.R. Heidemann. Mechanical tension can specify axonal fate in hippocampal neurons.

[52] A.C. Lee and D.M. Suter. Quantitative analysis of microtubule dynamics during adhesion-mediated growth cone guidance. *Dev. Neurobiol.*, 68:1363–1377, 2008.

[53] V. Lemmon, S.M. Burden, H.R. Payne, G.J. Elmslie, and M.L. Hlavin. Neurite growth on different substrates: permissive versus instructive influences and the role of adhesive strength. *J. Neurosci.*, 12:818–826, 1992.

[54] P.C. Letourneau and A.H. Ressler. Inibition of neurite initiation and growth by taxol. *J. Cell Biol.*, 98:1355–1362, 1984.

[55] P.C. Letourneau, T.A. Shattuck, and A.H. Ressler. Pull and push in neurite elongation: observations on the effects of different concentrations of cytochalasin b and taxol. *Cell Motil. Cytoskeleton*, 8:193–209, 1987.

[56] S.S. Lim, K.J. Edson, P.C. Letrourneau, and G.G. Borisy. A test of microtubule translocation during neurite elongation. *J. Cell Biol.*, 111:123–130, 1990.

[57] P. Lovell and L.L. Moroz. The largest growth cones in the animal kingdom: an illustrated guide to the dynamics of Aplysia neuronal growth in cell culture. *Integr. Comp. Biol.*, 46:847–870, 2006.

[58] G. Maheshwari, G. Brown, D.A. Lauffenburger, A. Wells, and L.G. Griffith. Cell adhesion and motility depend on nanoscale rgd clustering. *J. Cell Sci.*, 113:1677–1686, 2000.

[59] W. Mandemakers, V.A. Morais, and B. De Strooper. A cell biological perspective on mitochondrial dysfunction in parkinson disease and other neurodegenerative diseases. *J. Cell Sci.*, 120:1707–1716, 2007.

[60] D.R. McLean and B.P. Graham. Mathematical formulation and analysis of a continuum model for tubulin-driven neurite elongation. *Proc. R. Soc. Lond. A*, 460:2437–2456, 2004.

[61] K.E. Miller and S.R. Heidemann. What is slow axonal transport? *Exp. Cell Res.*, 314:1981–1990, 2008.

[62] K.E. Miller and D.C. Samuels. The axon as a metabolic compartment: protein degradation, transport, and maximum length of an axon. *J. Theor. Biol.*, 186:373–379, 1997.

[63] K.E. Miller and M.P. Sheetz. Axonal mitochondrial transport and potential are correlated. *J. Cell Sci.*, 117:2791–2804, 2004.

[64] K.E. Miller and M.P. Sheetz. Direct evidence for coherent low velocity axonal transport of mitochondria. *J. Cell Biol.*, 173:373–381, 2006.

[65] J.R. Morris and R.J. Lasek. Monomer-ploymer equilibria in the axon: direct measurement of tubulin and actin as polymer and monomer in axoplasm. *J. Cell Biol.*, 98:2064–2076, 1984.

[66] R.L. Morris and P.J. Hollenbeck. The regulation of bidirectional mitochondrial transport is coordinated with axonal outgrowth. *J. Cell Sci.*, 104 (Pt. 3):917–927, 1993.

[67] K.A. Myers and P.W. Baas. Kinesin-5 regulates the growth of the axon by acting as a brake on its microtubule array. *J. Cell Biol.*, 178:1081–1091, 2007.

[68] S. Okabe and N. Hirokawa. Turnover of fluorescently labelled tubulin and actin in the axon. *Nature*, 343:479–482, 1990.

[69] S. Okabe and N. Hirokawa. Differential behavior of photoactivated microtubules in growing axons of mouse and frog neurons. *J. Cell Biol.*, 117:105–120, 1992.

[70] S. Okabe and N. Hirokawa. Do photobleached microtubules move? re-evaluation of fluorescence laser photobleaching both in vitro and in growing *Xenopus* axon. *J. Cell Biol.*, 120:1177–1186, 1993.

[71] M. O'Toole, R. Baqri, R. Latham, and K.E. Miller. Modeling mitochondrial dynamics during in vivo axonal elongation. *J. Theor. Biol.*, 255:369–377, 2008.

[72] M. O'Toole, P. Lamoureux, and K.E. Miller. A physical model of axonal elongation: force, viscosity, and adhesions govern the mode of outgrowth. *Biophys. J.*, 94:2610–2620, 2008.

[73] B.J. Pfister, D.P. Bonislawski, D.H. Smith, and A.S. Cohen. Stretch-grown axons retain the ability to transmit active electrical signals.

[74] B.J. Pfister, A. Iwata, D.F. Meaney, and D.H. Smith. Extreme stretch growth of integrated axons. *J. Neurosci.*, 24:7978–7983, 2004.

[75] L.A. Pfister, M. Papaloizos, H.P. Merkle, and B. Gander. Nerve conduits and growth factor delivery in preipheral nerve repair. *J. Peripher. Nerv. Syst.*, 12:65–82, 2007.

[76] W. Rall. Branching dendritic trees and motoneuron membrane sensitivity. *Erp. Neurol.*, 1:491–527, 1959.

[77] S.S. Reinsch, T.J. Mitchison, and M. Kirschner. Microtubule polymer assembly and transport during axonal elongation. *J. Cell Biol.*, 115:365–379, 1991.

[78] F. Rossi, S. Gianola, and L. Corvetti. Regulation of intrinsic neuronal properties for axon growth and regeneration. *Prog. Neurobiol.*, 81:1–28, 2007.

[79] K. Rowshan, N.F. Jones, and R. Gupta. Current surgical techniques of peripheral nerve repair. *Oper. Tech. Othop.*, 14:163–170, 2004.

[80] S. Roy, M.J. Winton, M.M. Black, J.Q. Trojanowski, and V.M. Lee. Rapid and itermittent cotransport of slow component-b proteins. *J. Neurosci.*, 27:3131–3138, 2007.

[81] M. Sato, T.Z. Wong, D.T. Brown, and R.D. Allen. Rheological properties of living cytoplasm: a preliminary investigation of squid axoplasm (*Loligo pealei*). *Cell Motil.*, 4:7–23, 1984.

[82] A.W. Schaefer, V.T. Schoonderwoert, L. Ji, N. Mederios, G. Danuser, and P. Forscher. Coordination of actin filament and microtubule dynamics during neurite outgrowth. *Dev. Cell*, 15:146–162, 2008.

[83] B.J. Schnapp and T.S. Reese. Cytoplasmic structure in rapid-frozen axons. *J. Cell Biol.*, 94:667–669, 1982.

[84] A.K. Sharma, S. Bajada, and P.K. Thomas. Age changes in the tibial and plantar nerves of the rat. *J. Anat.*, 130:417–428, 1980.

[85] G.I. Sinclair, P.W. Baas, and S.R. Heidemann. Role of microtubules in the cytoplasmic compartmentation of neurons. ii. endocytosis in the growth cone and neurite shaft. *Brain Res.*, 450:60–68, 1988.

[86] D.A. Smith and R.M. Simmons. Models of motor-assisted transport of intracellular particles. *Biophys. J.*, 80:45–68, 2001.

[87] D.H. Smith. Stretch growth of integrated axon tracts. *Prog. Neurobiol.*, 89:231–239, 2009.

[88] L.R. Stanford. Conduction velocity variations minimize conduction time differences among retinal ganglion cell axons. *Science*, 238:358–360, 1987.

[89] L.R. Stanford. X-cells in the cat retina: relationships between the morphology and physiology of a class of cat retinal gnaglion cells. *J. Neurophysiol.*, 58:940–964, 1987.

[90] D.C. Van Essen. A tension-based theory of morphogenesis and compact wiring in the central nervous system. *Nature*, 385:313–318, 1997.

[91] M.P. Van Veen and J. Van Pelt. Neuritic growth rate described by modeling microtubule dynamics. *Bull. Math. Biol.*, 56:249–273, 1994.

[92] O.I. Wagner, J. Lifshitz, P.A. Janmey, M. Linden, T.K. McIntosh, and J.F. Leterrier. Mechanisms of mitochondria-neurofilament interactions. *J. Neurosci.*, 23:9046–9058, 2003.

[93] P. Weiss. Nerve pattern: the mechanics of nerve growth. *Growth (Suppl. Third Growth Symp.)*, 5:163–203, 1941.

[94] S. Yamada, D. Wirtz, and S.C. Kuo. Mechanics of living cells measured by laser tracking microrheology. *Biophys. J.*, 78:1736–1747, 2000.

[95] A. Yuan, T. Sasaki, M.V. Rao, A. Kumar, V. Kanumuri, D.S. Dunlop, R.K. Liem, and R.A. Nixon. Neurofilaments form a highly stable stationary cytoskelton after reaching a critical level in axons. *J. Neurosci.*, 29:11316–11329, 2009.

[96] K.M. Zareba. Circulation over the centuries: William harvey (1578–1657). *Cardiol. J.*, 14:214–215, 2007.

[97] J. Zheng, R.E. Buxbaum, and S.R. Heidemann. Investigation of microtubule assembly and organization accompanying tension-induced neurite initiation. *J. Cell Sci.*, 104:1239–1250, 1993.

[98] J. Zheng, R.E. Buxbaum, and S.R. Heidemann. Measurements of growth cone adhesion to culture surfaces by micromanipulation. *J. Cell Biol.*, 127:2049–2060, 1994.

[99] J. Zheng, P. Lamoureux, V. Santiago, T. Dennerll, R.E. Buxbaum, and S.R. Heidemann. Tensile regulation of axonal elongation and initiation. *J. Neurosci.*, 11:1117–1125, 1991.